PHD

Evaluation of a technique for the remote measurement of surface temperature distributions in laser heated samples

Ayling, Joanna R.

Award date:
1996

Awarding institution:
University of Bath

EVALUATION OF A TECHNIQUE FOR THE REMOTE MEASUREMENT OF SURFACE TEMPERATURE DISTRIBUTIONS IN LASER HEATED SAMPLES

Submitted by Joanna R Ayling
for the degree of
Doctor of Philosophy
of the University of Bath
1996

COPYRIGHT

J. Ayling

ProQuest LLC
789 East Eisenhower Parkway
P.O. Box 1346
Ann Arbor, MI 48106-1346

ABSTRACT

The nuclear power industry has a great interest in the thermal behaviour of nuclear fuels under the extreme environmental conditions encountered within a reactor core. A technique designed to calculate the thermal properties of such materials from a remote measurement of the temperature distribution created on their surface by an infra-red laser has been evaluated.

The experimental and analytical procedures have been tested, and the optimum system parameters determined. It has been shown that positioning of the test sample is crucial, and that damage to the target surface governs the overall validity of experimental results.

An investigation has been made into the physical responses of various materials to laser heating in order that the suitability of these materials to the temperature measurement system described may be determined. A low thermal conductivity, high emissivity, high melting point ceramic, such as uranium dioxide, is well suited to a thermodynamic study employing this method. Other materials, and in particular metals, have been found to be less appropriate.

CONTENTS

FIGURE LIST

TABLE LIST

ACKNOWLEDGEMENTS

Firstly, I would like to thank David Ladds for his assistance with this work, and my project supervisor George Saunders for allowing me the freedom to follow my own interests. Thanks are also due to Wendy Lambson for her practical help and preparation of all but the UO_2 samples, Barry Chapman for his assistance with the SEM work, Bill Clark for discussion of the optical techniques, Robert Draper for his photographic skills and general practical help, Owen Holbrook and John Trail for their practical suggestions, and all other members of the School of Physics.

I also wish to thank AEA Technology, Harwell, for their supply of UO_2 samples and partial financial assistance, in particular Robert Williamson (Reactor Services Division) and Antony Harker (Theoretical Physics Division).

Special thanks go to Peter Taylor and Mark Deven of the School of Materials Science for the supply and preparation of samples, for allowing access to their optical microscope, and general consultation and advice. Thanks also go to Les Steele, Jeff Venn, and all other members of the Science Workshop.

Finally I would like to thank David Ladds for many hours of proof reading and constructive criticism, and for his continuing support and encouragement.

CHAPTER 1

1. INTRODUCTION

1.1. BACKGROUND

The safety of nuclear reactors is of primary importance to the nuclear power industry. The safe operation of such systems requires a complete understanding of the thermodynamic behaviour of the fuel, both under normal and unusually severe conditions. The radioactive and toxic nature of these materials makes a study of their performance within the core itself very hazardous. The use of a theoretical model overcomes these risks, and also allows the mathematical simulation of abnormal operating conditions which may occur in the event of an accident.

Several models of this type have been constructed. However, these techniques require accurate experimental data on the thermal properties of the test material (nominally UO_2). Despite the huge growth in interest in the use of metal oxides as nuclear fuels in the 1950's, the extent of knowledge about their thermal properties at very high temperatures and pressures remains extremely limited due to the experimental difficulties involved in measuring them.

The central aim of a contract between AEA Technology Harwell and the School of Physics at the University of Bath was to measure these properties using small samples in a controlled laboratory environment, thus minimising the risks associated with the use of toxic and radioactive materials.

1.2. EXPERIMENTAL OBJECTIVES

The main objective of the project was to develop a system for the measurement of the thermal conductivity of uranium dioxide at simultaneous extremes of temperature and pressure. Experimental temperatures exceeding the melting point of the test material[1], and simultaneous pressures of up to 100kbar were requested. It was also recognised that the calculation of thermal diffusivity and the determination of a phase diagram would be beneficial.

AEA Technology expressly requested that any calculations of thermal conductivity be made directly from experimental data and not inferred from measured thermal diffusivity. A number of methods already exist for the determination of thermal diffusivity (many are described by Parrot and Stuckes, 1975) but the subsequent calculation of thermal conductivity requires a knowledge of density and specific

---

[1] Typically 3100K. A comprehensive list of measured melting points is given in section 7.1.4.

heat as a function of temperature. The conversion of thermal diffusivity to thermal conductivity is not a trivial task and is susceptible to the large inaccuracies described by Hutchings (1987).

It is possible to determine thermal conductivity directly from an experimental measurement of temperature provided that a temperature gradient or distribution exists. The solution of this problem has been discussed in detail by Tytler (1995) and is not considered further in this text.

1.3. PRINCIPLES OF EXPERIMENTAL DESIGN

The required experimental system may be divided into three parts: the creation of extreme pressures, a sample heating method, a temperature measurement technique.

1.3.1. THE CREATION OF EXTREME PRESSURES

Diamond anvil cells (DACs) have, in recent years, become standard instruments for the production of pressures in the megabar region. High pressures are achieved by placing the test sample between the flat parallel faces of two opposed diamond anvils, which are then forced together using a leverage mechanism. This technique creates a highly localised force on the sample and subsequently, a high pressure.

However, the use of a diamond cell imposes several experimental restrictions, the greatest being the allowable sample size. The maximum workable dimension of an anvil cell sample is approximately 300μm which limits the choice of heating mechanism. Also, the sample within the cell becomes physically inaccessible, although the diamonds' high transparency to both visible and infra-red radiation does allow optical access.

1.3.2. SAMPLE HEATING METHOD

The sample heating method had to meet quite specific criteria, namely the ability to produce highly localised temperature distributions with a peak in excess of 3200K.

Although temperatures of 3700K can be achieved in evacuated graphite element vacuum furnaces (Draper, private communication), they are not suitable for establishing the required sample temperature distribution. A platinum heating wire could be used to create a temperature distribution within the sample, but if used in air would begin to evaporate above 1700°C. Neither method is appropriate.

Laser heating is able to satisfy both of the necessary criteria. An infra-red laser can provide sufficient power to cause melting and is capable of establishing a radially symmetric temperature distribution with radial heat flow out from the centre (the hottest point). By operating such a laser in the TEM_{00} monomode, the resultant temperature distribution should be symmetrical and have a single peak.

Such a temperature distribution is appropriate for the method of thermal conductivity calculation adopted by Tytler (1995).

1.3.3. TEMPERATURE MEASUREMENT

The development of a system for temperature measurement provides the greatest experimental challenge because the extremely high experimental temperatures prevent the use of a standard apparatus such as thermocouples. The solution arrived at overcomes the problems posed by the diamond cell by exploring its optical properties, and by the extension of an original proposal made by Heinz and Jeanloz (1987).

Of the standard thermocouples available, the Platinum-13%Rhodium/Platinum type will operate at the highest temperature, 1700°C (TC Ltd, 1995). Tungsten-Tungsten/Rhenium thermocouples can operate successfully to higher temperatures, but the sheathing around the thermocouple will then introduce restrictions of its own. (Alumina sheaths are effective up to 2000°C (Draper, private communication)). Even supposing thermocouples were capable of operating at these temperatures, they would be too cumbersome to use effectively within a DAC.

Remote temperature measurement techniques are ideally suited to use with a diamond cell, and are particularly useful when high experimental temperatures render contact methods unworkable. Such methods of temperature measurement work upon the principle that when a hot body glows, the wavelength distribution of light intensity it emits may be used to find its temperature. This is called the Planck law of thermal radiation and its application to temperature measurement is described further in section 2.3.1.

Optical pyrometry and spectroradiometry are two temperature measurement techniques which make use of this relationship.

OPTICAL PYROMETRY

The optical system in a pyrometer, which includes a microscope, a calibrated light source and a narrow-band wave filter, is arranged so that a test body and the light source can be viewed simultaneously. A power supply is used to adjust the current through the calibrated light source and thus its temperature, see figure 1.1. When the test sample and light source filament appear indistinguishable as viewed through the filter, the intensity of light they are emitting at the wavelength selected by the narrow band filter, is matched. If the two bodies then have identical emissivities, they will be at the same temperature. In reality the emissivities are rarely the same and have to be taken into account (via the principle of brightness temperature) when calculating temperature.

Brightness temperature is defined as the temperature at which a blackbody would emit the same radiant flux as the test body, and is the temperature always measured by an optical pyrometer. For non-black bodies, the actual temperature of the test body is always more than the brightness temperature. The filament current is converted to brightness temperature by means of a predetermined calibration relationship. However, a detailed knowledge of the emissivity of the sample as a function of temperature and wavelength is required to make this conversion.

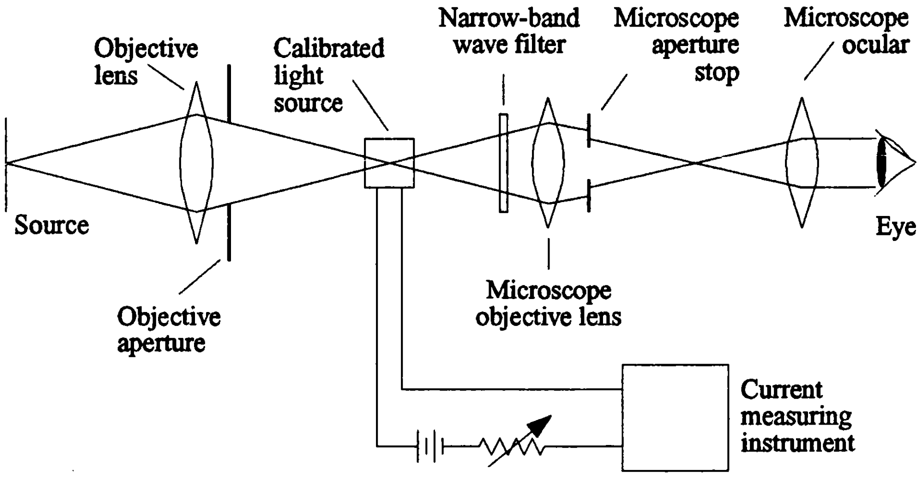

Figure 1.1. Schematic diagram of a single wavelength optical pyrometer.

Although optical pyrometry is a well established technique, it is only able to measure average temperatures. In addition, the emissivity of a material as a function of temperature is not always known. There are many texts on temperature measurement which include pyrometric techniques, for example Benedict (1984), Coxon (1960), and Herzfield (1962).

SPECTRORADIOMETRY

Spectroradiometry is a method based upon the principle that the emissivities of a material at two similar wavelengths will be approximately equal. Thus, over a short wavelength range the emissivity can be assumed to remain constant. By taking the ratio of the intensities of light emitted by a hot body at two similar wavelengths, the emissivity can be disregarded. However, if the two chosen wavelengths are not sufficiently far apart, the difference in measured intensities may be so small that a temperature difference cannot be resolved. Thus, the choice of measured wavelengths must be a compromise between these two conflicting demands.

Two sets of apparatus which use this principle are a scanning slit and monochromator, and a spectrograph and solid state detector.

Scanning Slit and Monochromator

A scanning slit and monochromator apparatus has been used by Heinz and Jeanloz (1987) to measure the temperature distribution across the face of a laser heated sample contained within a diamond cell. The method employed a narrow slit to scan across the image and a monochromator and solid state detector to measure the intensity of light produced across it at a number of selected wavelengths (see figure 1.2). The temperature distribution across the sample surface may be reconstructed from this data.

The main disadvantage of this method is the considerable time taken to collect the data for a single temperature reconstruction. It is only applicable for steady state measurements, and it is imperative that the experimental conditions remain stable throughout the whole data acquisition process, which may take several minutes. Also, the measurement of intensity distributions for only a small number of wavelengths makes the conversion to temperature distribution susceptible to significant error. As far as the author is aware Jeanloz's group has now ceased all work in this field.

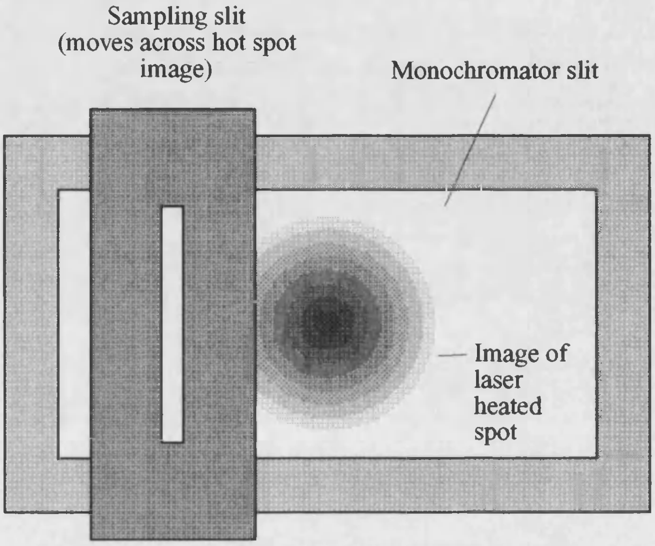

Figure 1.2. Image of laser heated spot in monochromator slit

Spectrograph and Solid State Detector

The main strength of using a spectrographic technique is that the light intensity across the whole image may be measured simultaneously for all wavelengths in the measurable range (determined by the spectrograph grating used). The system operates by passing the entire image of the hot spot formed on the sample into the entrance slit of a spectrograph. The grating within the spectrograph splits the image into its separate wavelength components and reflects these separate images onto the face of a solid state detector.

A more comprehensive comparison of optical pyrometry and spectroradiometry has been made by Heinz and Jeanloz (1987).

1.4. WORK OUTLINE

An apparatus which uses a spectroradiometric technique, employing a spectrograph and solid state detector, for the measurement of surface temperature distributions in laser heated samples has been described by Ladds (1994). The work described in this thesis involves an evaluation of this system, and may be summarised as follows:

- To establish the practical limitations of the apparatus and to determine the optimum experimental conditions.
- To define the conditions under which collected data may be validated.
- To perform an evaluation of the data analysis programs.
- To develop an understanding of the interaction between a laser beam and a material surface by a comparison of the microscopic appearance of the heated sample and the collected data.
- To explore the effect of target surfaces prepared by different techniques on the performance of the system.

- To determine the range of application of the experimental system with regard to different test materials.
- To quantify the effects of ambient temperature and humidity.
- To obtain data suitable for the calculation of thermal conductivity and thermal diffusivity by the methods described by Tytler (1995).

Note that although several additions to the apparatus described by Ladds (1994) are described, the analysis programs remain unchanged.

CHAPTER 2

2. THEORY

The basic principles behind the use of an infra-red laser and spectrographic technique to measure remotely temperature profiles formed across a laser heated surface were introduced in chapter 1. It is now necessary to consider in greater detail some of the theories behind the use of such an apparatus:

- A laser operating in its fundamental TEM_{00} mode should produce a Gaussian beam, that is one which has a Gaussian variation in light intensity along a line perpendicular to, and symmetric about, its axis. To understand the propagation of such a beam through an optical system and to quantify its physical properties, an understanding of Gaussian optics is required. The general features of Gaussian optics are considered in section 2.1 but for a more comprehensive description the reader should consult other texts such as those by O'Shea (1985), Pedrotti and Pedrotti (1987), and Levi (1980).

- When a laser beam is incident on a material surface it will cause localised heating. Provided sufficient laser power is absorbed by the surface, it will melt and then vaporise. The two classes of physical properties of the target material which govern the temperature response of the sample are described in section 2.2: light absorption characteristics, thermal properties. The different types of surface damage which may be caused by the laser are also considered.

- The light emitted by a hot body has a distinctive intensity versus wavelength relationship predicted by the Planck law of thermal radiation. The role of emissivity, and the temperature dependence of this relationship is considered further in section 2.3. The Wien law, which may be used as a useful approximation to the Planck law at low temperatures is also described.

- The Radon transform forms the basic mathematical framework for a large class of reconstruction problems. The work described within this thesis uses this technique to reconstruct the radial temperature distribution formed on the surface of the test sample from the condensed data collected by the optical detection system described in section 3.2. A brief outline of this theory is given in section 2.4, but for further information the reader should consult Deans (1983).

2.1. GAUSSIAN OPTICS

2.1.1. THE GAUSSIAN FUNCTION

The Gaussian function may be written

$$I(r) = I_0 \exp\left[\frac{-2r^2}{\omega^2}\right], \tag{2.1}$$

where I_0 is the on-axis intensity, and ω is the radius of the beam; and is illustrated in figure 2.1. (By definition, ω is the radius of the beam at which the intensity is $1/e^2$ of its peak value (I_0).)

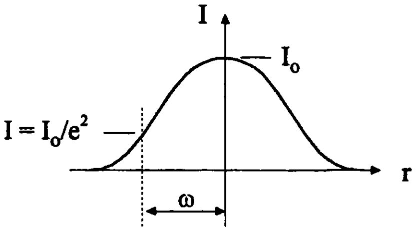

Figure 2.1. Gaussian beam profile.

THE FOURIER TRANSFORM OF A GAUSSIAN

Consider an aperture which is illuminated by parallel light, located in the front focal plane of a converging lens. The aperture scatters plane waves which are collected by the lens and brought to convergence at its back focal plane. The image formed at this plane has been shown (Hecht, 1987) to be equivalent to the Fourier transform of the electric field distribution across the aperture (also known as the aperture function).

A Gaussian is a unique mathematical function in that its Fourier transform is also Gaussian. The implication of this is that although the size of the beam will change as it is focused by lenses, the intensity distribution will remain Gaussian throughout the entire optical path of the beam, provided intensity is not lost from the edge of the image. In practice, the self Fourier Transform rule is maintained provided that the width of lenses and apertures used within the optical system is at least four times the beam width (Newport catalogue, 1990).

2.1.2. DIVERGENCE

In practice a Gaussian beam is either diverging from, or converging to, a region where it is narrowest. The width of the beam at its narrowest point is called the beam waist (ω_0) and is equivalent to the focal point of a geometric beam. It is only at the beam waist, and over an infinitesimally small distance, that the beam width can be considered constant (see figure 2.2).

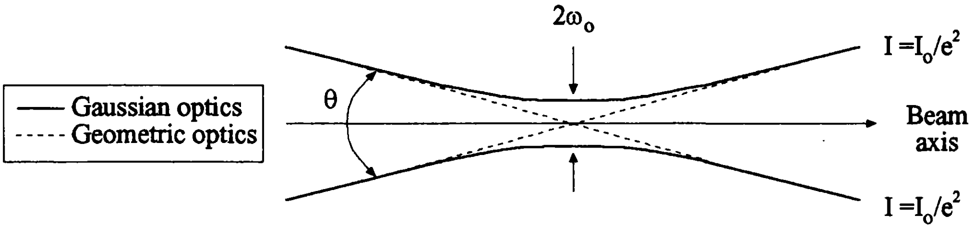

Figure 2.2. Schematic of a Gaussian beam waist.

The width of the beam as a function of the distance (x) from the beam waist is given by,

$$\omega^2 = \omega_0^2\left(1+\left(\frac{x\lambda}{\pi\omega_0^2}\right)^2\right)^2, \tag{2.2}$$

(Newport catalogue, 1990), where λ is the wavelength of the beam.

As the beam diverges from the beam waist, the line subtended by the $1/e^2$ intensity contours (ie where $I = I_0/e^2$), becomes straight. The full angle beam divergence (θ) is defined as twice the angle this line makes with the beam axis and is also shown in figure 2.2. The angle θ may be easily determined and used to calculate the size of the beam waist, which cannot always be measured directly (see section 3.1.2).

The application of simple geometry to the situation shown in figure 2.2 gives

$$\tan\left(\frac{\theta}{2}\right) = \frac{\omega}{x}, \tag{2.3}$$

which, because θ is small, may be written

$$x = \frac{2\omega}{\theta}. \tag{2.4}$$

Substitution for x (from equation 2.4) in equation 2.2, and simplifying gives

$$\frac{\omega}{\omega_0} - 1 = \frac{2\omega\lambda}{\pi\theta\omega_0^2}. \tag{2.5}$$

Since,

$$\frac{\omega}{\omega_0} \gg 1, \tag{2.6}$$

equation 2.5 may be written,

$$\omega_0 = \frac{2\lambda}{\pi\theta}. \tag{2.7}$$

Hence, provided the full angle beam divergence and wavelength are known, the calculation of beam waist radius from equation 2.7 is trivial.

2.1.3. POWER DISTRIBUTION AND SPOT SIZE

The power P(ω) contained within a radius ω of a Gaussian beam at the waist may be found by integrating the intensity distribution (equation 2.1) from 0 to ω to give

$$P(\omega) = P(\infty)\left(1 - \exp\left(\frac{-2\omega^2}{\omega_0^2}\right)\right), \tag{2.8}$$

where P(∞) is the total power contained in the beam (Newport catalogue, 1990). Calculated values of the percentage of the total laser power contained within a given radius are presented in table 2.1.

It is apparent from the values given in table 2.1 that 99.97% of the total laser power at the beam focus is contained within a radius of twice the beam waist. This would suggest that the hot spot formed on a sample by a focused laser will be ~4ω_0 in diameter. (In practice this is not strictly true, as discussed further in section 6.3.1). It also follows that 99.97% of the laser power is contained within a radius 2ω along the beam's entire axis, leading to the earlier statement (section 2.1.1) that the limiting diameter of any aperture is 4ω.

ω	$[P(\omega)/P(\infty)]\times100$ /%
$\frac{1}{4}\omega_0$	11.75
$\frac{1}{2}\omega_0$	39.35
$\frac{3}{4}\omega_0$	67.53
ω_0	86.47
$2\omega_0$	99.97

Table 2.1. Percentage of total power of a Gaussian distribution contained within a given radius.

2.1.4. DEPTH OF FOCUS

In Gaussian optics the depth of focus (D) is defined as the range along the beam axis for which the beam radius remains less than $\sqrt{2}\omega_0$. Substitution for $\omega = \sqrt{2}\omega_0$ in equation 2.2, and rearranging gives,

$$x = \frac{\pi\omega_0^2}{\lambda}. \qquad (2.9)$$

Since x is equivalent to the distance beyond the beam waist for which $\omega \leq \sqrt{2}\omega_0$, the depth of focus may be found by doubling x to take into account the distance in front of the sample for which $\omega \leq \sqrt{2}\omega_0$, giving

$$D = \frac{2\pi\omega_0^2}{\lambda}. \tag{2.10}$$

In practice it is almost impossible to position a sample precisely at the beam waist. However, provided the sample lies within the depth of focus there will be no serious deterioration of the hot spot formed on the test surface by the laser.

2.2. LASER INTERACTION WITH MATERIALS

2.2.1. OPTICAL PROPERTIES OF THE TARGET MATERIAL

The surface finish, surface oxidation and reflectivity of a material, all affect its thermal response to laser radiation. A highly polished surface will reflect more light than a greyed one (see section 4.1.1), as will a material with a high reflectance of the incident radiation. If a large proportion of light is reflected, little will be absorbed, and heating of the sample will be minimal. An oxidised surface is likely to absorb more radiation than the un-oxidised equivalent (Charschan *et al*, 1978).

Reflectivity (R) is defined as the ratio of the radiant power reflected from the surface to the radiant power incident on that surface, thus giving a dimensionless number between zero and unity. Note that reflectivity is sometimes discussed in terms of emissivity (ε), where

$$\varepsilon = 1 - R. \tag{2.11}$$

Most non-metals are effective absorbers of infra-red energy with typical reflectivities of 10% across the entire wavelength spectrum (Charschan *et al*, 1978). However, metals demonstrate more complex behaviour in their ability to absorb energy. The reflectivity as a function of incident wavelength of several metals with polished surfaces is shown in figure 2.3.

Because the reflectivity of a material is in practice a function of several conditions including its surface finish, temperature and the state of oxidation, the values given in figure 2.3 are not absolute, but demonstrate several general features. Both gold and copper have reflectivities which are low in the blue portion of the electromagnetic spectrum and approach unity at the red end. Other metals, such as silver, have a high reflectance of all visible radiation which accounts for their whitish appearance. Nickel, molybdenum and tungsten have lower reflectivity across the entire spectrum and ferrous metals have been shown to behave in a similar fashion (Charschan *et al*, 1978).

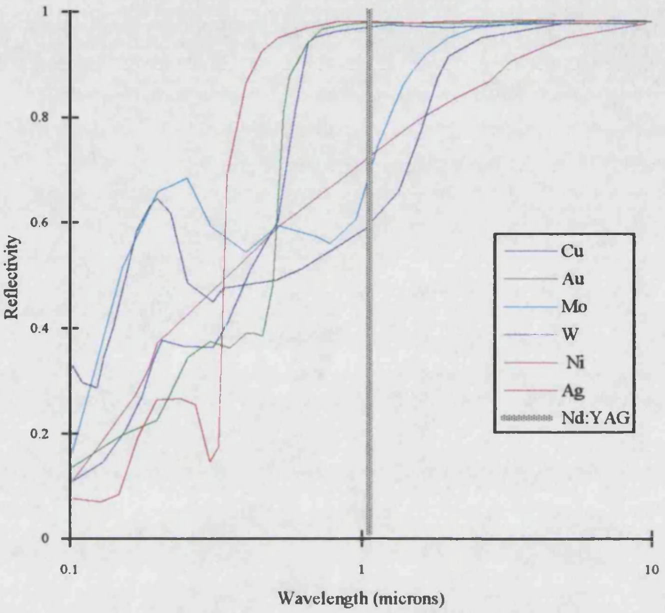

Figure 2.3. Reflectivity as a function of wavelength for various materials according to Palik (1985).

(The wavelength of a Nd:YAG laser is shown for reference.)

In general the reflectivity of metals is high at infra-red wavelengths, which would indicate a poor ability to absorb laser energy. However, when a focused laser beam is used to heat a metallic target, the effective absorptivity can approach values close to those observed in non-metals. For example, Charschan *et al* (1978) observed that an aluminium surface exposed to a laser pulse with a power per unit area of 10^7 $\mathrm{Wcm^{-1}}$, had an original reflectivity of approximately 70% which dropped to 20% after 0.2ms exposure and then remained constant for a further 0.8ms. This observation indicates the presence of a threshold value in laser power density, above which the reflectivity of a metal target reduces quite significantly.

2.2.2. THERMAL PROPERTIES OF THE TARGET MATERIAL

The flow of heat through a material is governed by its thermal properties, with thermal conductivity and thermal diffusivity being of particular importance. Phase transitions are governed by other properties such as melting and boiling temperatures and by the latent heats of melting and vaporisation. Thermal conductivity, thermal diffusivity and melting are discussed separately in the following sections.

THERMAL CONDUCTIVITY

Consider a parallel sided slab of cross-sectional area A. If one face is maintained at a higher temperature than the other, there will be a net flow of heat from the hot face to the cold one. Thermal conductivity (κ) may then be defined by

$$\frac{dQ}{dt} = -\kappa A \frac{d\theta}{dx}, \qquad (2.12)$$

where dQ/dt is the rate of flow of heat from the hot to the cold face, and $d\theta/dx$ is the temperature gradient established across the slab.

Materials with a high thermal conductivity conduct heat easily through their bulk and the temperature rise caused by a laser beam will be dissipated quickly. Conversely, low thermal conductivity materials conduct heat less readily and the diffusion of heat through their bulk will be slower.

The thermal conductivities, at room temperature, of some materials relevant to this study are presented in table 2.2.

Material	Thermal conductivity /$Wm^{-1}K^{-1}$ at 273.2K
Aluminium	236 [1]
Iron	83.5 [1]
Molybdenum	139 [1]
Tungsten	177 [1]
Zirconium	23 [1]
Uranium dioxide	12 (at 298K) [1]
Zirconia	1.8 (at 298K) [1]
$Bi_2Sr_2CaCu_2O_{8+\delta}$	4 [2]
Polycrystalline graphite	5.0 (at 293K) [3]

Table 2.2. Thermal conductivity of selected materials, according to: [1] Kaye and Laby (1986), [2] Ginsberg (1992), [3] Tennent (1988).

Metals tend to be good thermal conductors because of the contribution to heat transport of free electrons. The absence of free electrons in insulators would indicate a poor ability to conduct heat, but this is not necessarily true. For example, diamond is an excellent thermal conductor. However, ceramics tend to have short mean free paths due to the presence of grain boundaries and are thus poor thermal conductors. Although a pure single crystal of graphite would have a fairly high thermal conductivity, especially parallel to the basal plane, commercially available graphite is a far poorer thermal conductor due to the high concentration of lattice defects and its small grainsize.

The porous nature of ceramics results in an effective thermal conductivity which is lower than published values. A simplified relationship due to Loeb (1954) may be used to relate quoted values (which are for the theoretically dense material) and the measured values of thermal conductivity (κ_t and κ_m respectively) according to

$$\kappa_m = \kappa_t(1 - f), \tag{2.13}$$

where f is the fractional pore volume given by

$$f = \frac{\rho_t}{\rho_m} - 1, \tag{2.14}$$

where ρ_t is the theoretical density for a fully dense material, and ρ_m is the measured density.

Ross (1960) has shown that polycrystalline samples with a low density may have thermal conductivities even lower than those predicted by Loeb due to the presence of irregular or anisometric pores at the grain boundaries. Thus, equation 2.13 can only be used to give an approximate value for the thermal conductivity of a porous sample.

For further comparisons of the thermal conductivity of metals and non-metals the reader should consult texts by Berman (1976) or Slack (1972).

THERMAL DIFFUSIVITY

The thermal diffusivity (α) of a material is a measure of the speed with which heat will travel through a material and is defined by,

$$\alpha = \frac{\kappa}{\rho C_p}, \tag{2.15}$$

where ρ is the density, and C_p the specific heat of the material.

In general a material with a high thermal diffusivity will suffer significant heat penetration because heat is conducted quickly from its surface into the interior. As a result the location of heat boundaries, such as the edge of the sample, become more significant.

The thermal diffusivity at room temperature for some materials relevant to this study is given in table 2.3.

Material	Thermal Diffusivity /cm^2s^{-1}
Aluminium	0.91 [1]
Iron	0.21 [1]
Molybdenum	0.48 [1]
Platinum	0.25 [2]
Tungsten	0.62 [1]
Zirconium	0.13 [2]
Uranium dioxide	0.035 [3]
Zirconia	0.007 [3]
Polycrystalline graphite	0.031 [2]

Table 2.3. Thermal diffusivity of selected materials according to: [1] Charschan *et al* (1978), [2] calculated from equation 2.15 using data presented by Tennent (1988), [3] Morrel (1985).

The practical implications of thermal diffusivity values are well demonstrated by the principles of penetration depth and the thermal time constant.

Depth of Penetration and Thermal Time Constant

Consider a semi-infinite plate. The depth of penetration of heat (z) in a time (t) is given approximately by

$$z = \sqrt{4\alpha t}, \qquad (2.16)$$

(Charschan *et al*, 1978). Figure 2.4 shows the depth of penetration as a function of time, calculated from equation 2.16 using the data presented in table 2.3. Three materials have been considered; iron and aluminium which are typical of low and high thermal diffusivity metals respectively, and uranium dioxide which is a low thermal diffusivity ceramic.

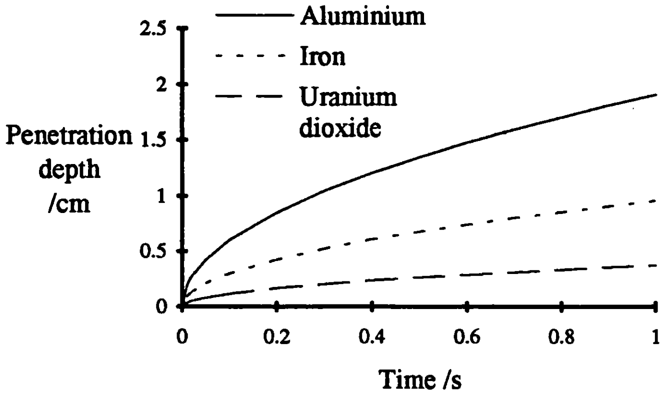

Figure 2.4. Penetration depth versus time for three selected materials.

It may be observed from figure 2.4 that after 1 second heat has penetrated almost seven times further in aluminium than in urania, but that even in urania the heat has travelled ~0.3cm within that time.

The thermal time constant (t_c) represents the laser pulse duration required for the heat to penetrate completely a semi-infinite plate of thickness x, and is given by

$$t_c = \frac{x^2}{4\alpha}. \tag{2.17}$$

Thermal time constants calculated from equation 2.17 for sheets of different thicknesses are shown in figure 2.5. The same three materials (aluminium, iron and uranium dioxide) have been considered.

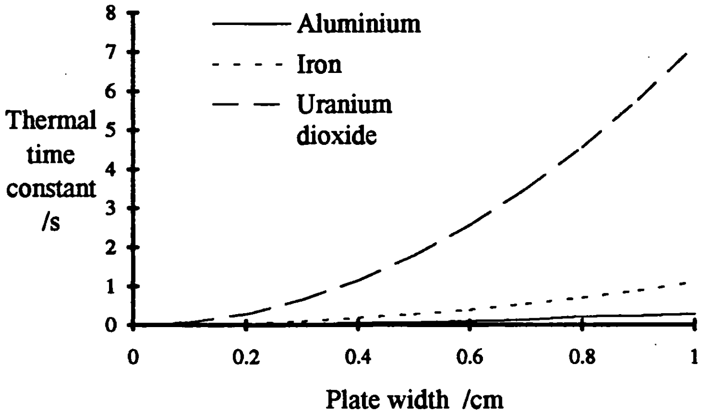

Figure 2.5. Thermal time constant versus plate width for three selected materials

Figure 2.5 indicates that heat will penetrate a 1cm thick sheet of aluminium in well under 1 second, whereas for uranium dioxide the same process will take in excess of 7 seconds.

The values presented in figures 2.4 and 2.5 support well the theory that a material with a high thermal diffusivity will conduct heat quickly through its bulk. In such cases the sample thickness becomes a crucial parameter and must be considered in any thermodynamic analysis.

MELTING

The purpose of the project on which this thesis is based was to develop a system to investigate the thermal properties of a refractory material. As such, the apparatus is unsuitable for a study of materials with too low a melting point because deformation of the surface will be too extreme for its temperature to be accurately measured (see section 6.4.3). However, materials with too high a melting point, although being suitable for temperature measurements, may not be appropriate for the determination of phase diagrams. The melting points of some materials relevant to this study are given in table 2.4.

Material	T_m/°C
Aluminium	659 [1]
Iron	1535 [1]
Molybdenum	2500 [1]
Platinum	1755[1]
Tungsten	3400 [1]
Zirconium	1852 [1]
Uranium dioxide	2880 [2]
Zirconia	2677 [2]
$Bi_2Sr_2CaCu_2O_{8+\delta}$	1203 [3]
Polycrystalline graphite	3350* [1]

Table 2.4. The melting temperatures of selected materials according to: [1] Weast (1976), [2] Kaye and Laby (1986), [3] Heeb *et al* (1993). (*Sublimes)

2.2.3. HOLE FORMATION

When a laser beam is incident on a surface, heat will diffuse into the material and raise its temperature. Surface reflectance and thermal effects (which were discussed in sections 2.2.1 and 2.2.2), and laser power density determine how great the temperature rise will be. Provided it is large enough, a melt puddle will form on the sample surface and the material will start to vaporise. When the target material has vaporised, a plasma, which absorbs the incoming light, is formed. Therefore, once vaporisation has occurred the incoming light is effectively cut-off and further laser heating will be minimal.

Table 2.5 lists the times taken to reach vaporisation for some metals with absorbed laser power densities of 10^5 to 10^7 Wcm^{-2}, which are typical of the power densities obtainable with a pulsed ruby, Nd:glass, or Nd:YAG laser, and simple focusing optics (Charschan *et al*, 1978).

	Absorbed laser power density /Wcm^{-2}		
Metal	10^5	10^6	10^7
Iron	1.86 ms	18.6 μs	186 ns
Aluminium	2.67 ms	26.7 μs	267 ns
Molybdenum	5.56 ms	55.6 μs	556 ns
Tungsten	10.46 ms	104.6 μs	1.05 μs

Table 2.5. The time taken to reach vaporisation for several common metals according to Charschan *et al* (1978).

It is apparent from the data presented in table 2.5 that vaporisation occurs very quickly in metals, thus indicating that laser heating of the surface will cease after a comparatively short time.

If sufficient laser power is delivered to the sample, a hole will form. Two major types of holes are observed; either all of the ejected material is vaporised and a 'clean' indentation occurs, or molten material on the surface of the hole is ejected in hot glowing globules. In the latter case, a hole starts to form, vapour pressure increases, and there is a flow of molten material towards the exit aperture of the crater. This type of hole formation results in greater mass removal than if all the removed material were vaporised. Experimental evidence of both types of hole formation is presented in section 6.4.1.

HOLE CHARACTERISTICS

Theory (section 2.1.3) predicts that the hole formed on the surface of the test sample by a laser will be ~$4\omega_0$ in diameter. However, due to heat diffusion, the heated area will be larger than $4\omega_0$, and the size of a hole created on the surface will be dependent upon the thermal properties of the sample as well as the characteristics of the heating laser beam. This is discussed further in section 6.3.1.

The geometrical characteristics of a laser drilled hole are best described in terms of their aspect ratio (A) defined by,

$$A = \frac{\ell}{d_m}, \tag{2.18}$$

where ℓ is the depth, and d_m the midpoint diameter of the hole as shown in figure 2.6.

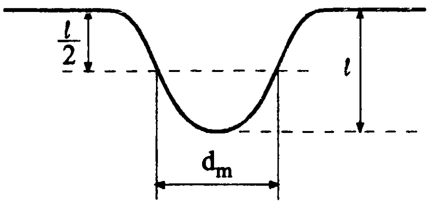

Figure 2.6. Sectional view of a laser drilled hole.

The limiting aspect ratio for a particular material depends upon both the optical characteristics of the beam and the optical and thermal properties of the material. Beams focused with a large convergence angle will have a smaller depth of focus and will tend to produce low aspect ratio holes. High thermal diffusivity will also assist in achieving low aspect ratio holes. Holes much deeper than the depth of focus may be drilled in some materials by a 'light pipe' mechanism. Multiple reflections of laser light from the hole walls at shallow angles of incidence are believed to channel the optical energy to the bottom of the hole. In general aspect ratios exceeding 25 have been obtained in ceramics, but limiting ratios of 8 to 12 are common for most metals (Charschan *et al*, 1978).

2.3. THE LAWS OF THERMAL RADIATION

2.3.1. PLANCK RADIATION LAW

Consider a hollow cavity containing a single body thermally insulated from the walls. If the walls are maintained at a constant temperature, thermal radiation will fill the cavity. The body will absorb radiation, and in turn emit it, until an equilibrium condition is established. An object which absorbs all radiation incident upon it is known as a black body and black body radiation is the term applied to the energy emitted by it in the form of photons.

In 1901 Planck derived an equation for the distribution, as a function of wavelength, of black-body radiation within a cavity. Unlike earlier theories (discussed in detail by Fowles, 1975) Planck's hypothesis was in total agreement with experimental observations. He assumed that energy could exist only in discrete multiples of some lowest amount: the basis of quantum theory. By considering the distribution of photons amongst the available modes within the cavity, he concluded that the distribution of radiative intensity as a function of wavelength (λ) and temperature (T) could be described by the equation,

$$I(\lambda, T) = \frac{2\pi hc^2\lambda^{-5}}{\exp\left(hc/k_B\lambda T\right) - 1}, \qquad (2.19)$$

where h is the Planck constant, c is the speed of light in a vacuum, and k_B is Boltzmann's constant.

EMISSIVITY

Equation 2.19 may be used to predict the radiative intensity, or spectral radiance, of a black body. However, actual temperature sources are not true black bodies and so produce intensities smaller than those predicted by this equation. Emissivity (ε) is defined as the ratio of the intensity of such a thermal source to that of a black body at the same temperature. Provided the intensity is measured in the same direction for both cases, emissivity can be written,

$$\varepsilon(\lambda, T) = \frac{I(\lambda, T)\big|_{\text{source}}}{I(\lambda, T)\big|_{\text{blackbody}}}. \tag{2.20}$$

Substitution into equation 2.19 yields,

$$I(\lambda, T, \varepsilon) = \frac{2\pi h \varepsilon c^2 \lambda^{-5}}{\exp\left(hc/k_B \lambda T\right) - 1}. \tag{2.21}$$

Equation 2.21 may be used to predict the spectral radiance for non-black bodies with an emissivity ε. An extensive description of the role of emissivity has been made by Boyd (1983).

TEMPERATURE DEPENDENCE

Figure 2.7 demonstrates how the intensity/wavelength distribution predicted by the Planck radiation law varies with temperature. As the temperature decreases, the distribution's peak moves towards the longer wavelength end of the spectrum, and becomes less distinct.

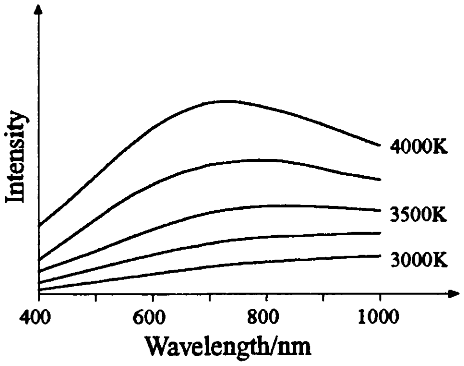

Figure 2.7. The Planck distribution at different temperatures.

The experimental implications of this observation are discussed further in section 4.5.5.

2.3.2. WIEN RADIATION LAW

The original model for black body radiation was derived by Wien in 1896 (Grant, 1977) and takes the form,

$$I(\lambda, \varepsilon, T) = \frac{2\pi hc^2 \varepsilon \lambda^{-5}}{\exp\left(hc/k_B \lambda T\right)}. \qquad (2.22)$$

Although this model is inaccurate at high temperatures, the difference between the Wien and Planck laws becomes insignificant at lower temperatures, as shown in figure 2.8. The Wien law is a useful approximation to the Planck law since it may be reduced to an expression which is linear in terms of inverse temperature. This makes its application to remote temperature measurement far less complex than the Planck distribution, as discussed further in sections 4.5.5 and 5.4.2.

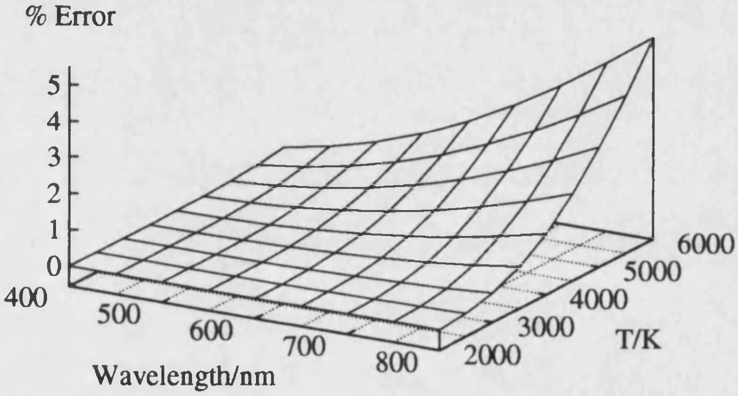

Figure 2.8. Percentage error between the Wien and Planck distributions.

2.4. THE RADON TRANSFORM

2.4.1. INTRODUCTION

If a probe acts upon an internal distribution within an object, it is able to produce a projected distribution, or profile. If the internal property of the object is represented by some function f, the profile can be approximated by the Radon transform of f, represented by

$$\check{f} = \mathcal{R} f . \qquad (2.23)$$

Each profile is in fact only a sample of the Radon transform. The form of the profiles at all angular positions must be known to constitute a full knowledge of the Radon transform. Figure 2.9 shows two profiles constructed from a two dimensional distribution by use of the Radon transform.

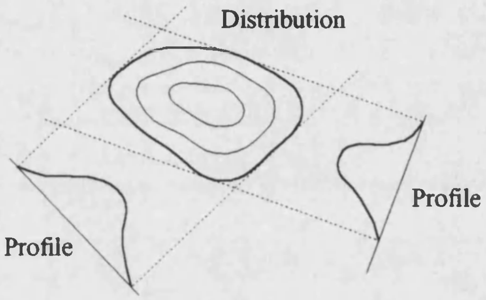

Figure 2.9. Two dimensional distribution and reconstructed profiles.

2.4.2. THE ABEL TRANSFORM

The Abel transform is a special case of the Radon transform in that angular symmetry is assumed. It is expressed by

$$\check{f} = \mathcal{A} f . \qquad (2.24)$$

The Abel transform may be used to calculate the profiles resulting from a distribution, but since all profiles are the same, only one profile need be determined. Figure 2.10 shows the profile constructed from a two dimensional angularly symmetric distribution.

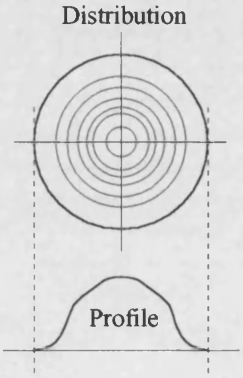

Figure 2.10. Angularly symmetric distribution and reconstructed profile.

2.4.3. THE INVERSE TRANSFORMS

The Radon and Abel transforms each have corresponding inverse transforms (see Deans, 1983) which may be used to reconstruct internal distributions from a set of measured profiles. In the case of the inverse Abel transform, radial symmetry is still assumed, and only one measured profile is required to make the conversion from the profile to the distribution. The practical application here of the inverse Abel transform is discussed in section 4.5.4.

CHAPTER 3

3. EXPERIMENTAL APPARATUS

The experimental apparatus consists of an infra-red laser, an optical system, a detection system and a test sample. The laser heats the test sample causing it to glow, the optical system manipulates the image formed and the detection system records the light intensity versus wavelength relationship of this image. A schematic diagram of the experimental apparatus is given in figure 3.1.

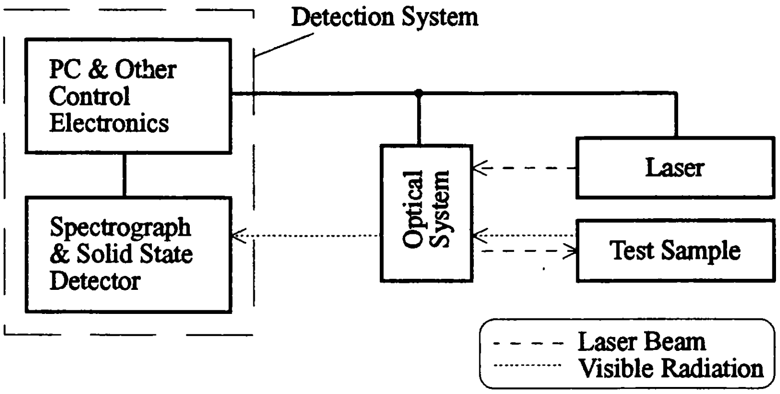

Figure 3.1. Schematic diagram of the experimental apparatus.

3.1. THE LASER

A model 117, Quantronix Series 100, 18W Nd:YAG laser is used to heat the test sample. It has been configured for continuous wave (CW) output and produces a beam with a wavelength of 1064nm. An intercavity aperture (mode selector) ensures that the laser operates in its fundamental mode (TEM_{00}) to produce a beam with a Gaussian transverse power distribution.

3.1.1. LASER STABILISER

The laser output may be stabilised using a model 366 Quantronix laser stabiliser. This unit continuously samples the laser beam by means of an output power monitor located behind the rear mirror housing (see figure 3.2) and compensates for any fluctuations in output by adjusting the power supplied to the flash lamp. An output from the stabiliser circuitry allows a scaled DC voltage measurement of laser output power whether the stabiliser is enabled or not. The output voltage is recorded by means of a chart recorder, which allows a more accurate measure of laser power than would the dial on the front of the power supply which measures laser flash lamp current.

During the period when the laser is stabilised, the electromechanical shutter situated next to the front mirror housing must remain open; so to protect the operator, an additional, external, shutter has been included in the optical system (see section 3.2.3). In the event of an emergency, 'panic' switches located around the laboratory are available to close the internal shutter at any time.

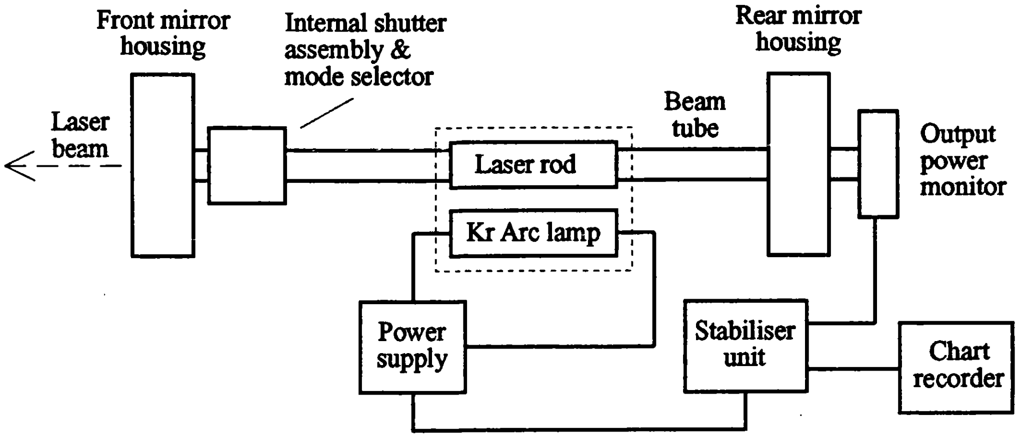

Figure 3.2. Nd:YAG laser components.

Further information on the operation of the laser and the laser stabiliser may be found in the appropriate instruction manuals (Quantronix, 1984, and Quantronix, 1990 respectively).

3.1.2. LASER BEAM PROFILER

The numerical analysis (section 4.5) assumes that the laser beam remains Gaussian throughout its operation. It is also imperative that the laser's output power remains stable during the data acquisition processes. An Optilas 2180 BeamScan beam profiler, consisting of a scan head and controller unit, is used to measure the shape and stability of the beam.

The beam profiler is a standard tool for the characterisation of a laser beam. The scan head measures the irradiance across the axis of the beam and is moved along the laser axis via an optical rail. The control unit is an MS-DOS based PC with a 3.5", 1.4 Mbyte, floppy drive and built-in monitor, on which the dedicated Laserbeam Analysis Program is run. This software enables the direct measurement of beam width (defined in section 2.1.1) and peak irradiance. It may also be used to fit an ideal Gaussian to the measured beam profile and provide a value for the goodness of fit (G) determined by,

$$G = \frac{\sqrt{\left(\sum_{i=0}^{N}(f(i)-d(i))^2\right)\Big/N}}{I_p} \qquad (3.1)$$

(Photon Inc., 1991) where f(i) is the fitted irradiance at a position i, d(i) the actual irradiance at the position i, N the number of samples and I_p the peak irradiance value. A small value of G corresponds to a good fit (G=0 is equivalent to a perfect fit), and conversely, a high value for G indicates that the measured intensity distribution is only poorly approximated by a Gaussian.

The region in which the shape of the beam is of most interest is at the test sample position which is shown later to be at a beam waist. The laser beam's power density is at a maximum at this point, and is too large to measure without damage being caused to the optical detector inside the beam profiler scan head. However, a measurement of beam divergence allows a calculation of the beam waist from equation 2.7 given on page 32. Results of a typical beam profiling measurement are presented in section 5.1. Further information on the operation of the beam profiler may be found in the instruction manual (Photon Inc., 1991).

3.2. THE OPTICAL SYSTEM

The optical system consists of a series of mirrors and shutters, a filter, a focusing lens, and an imaging lens. The focusing lens, dichroic mirror, and filter were purchased (contained within a protective box) from the US Laser Corporation as a self-contained viewing and focusing apparatus (model 1001-7). The external shutter, imaging lens, and the aperture, see figure 3.3, were added in a later modification.

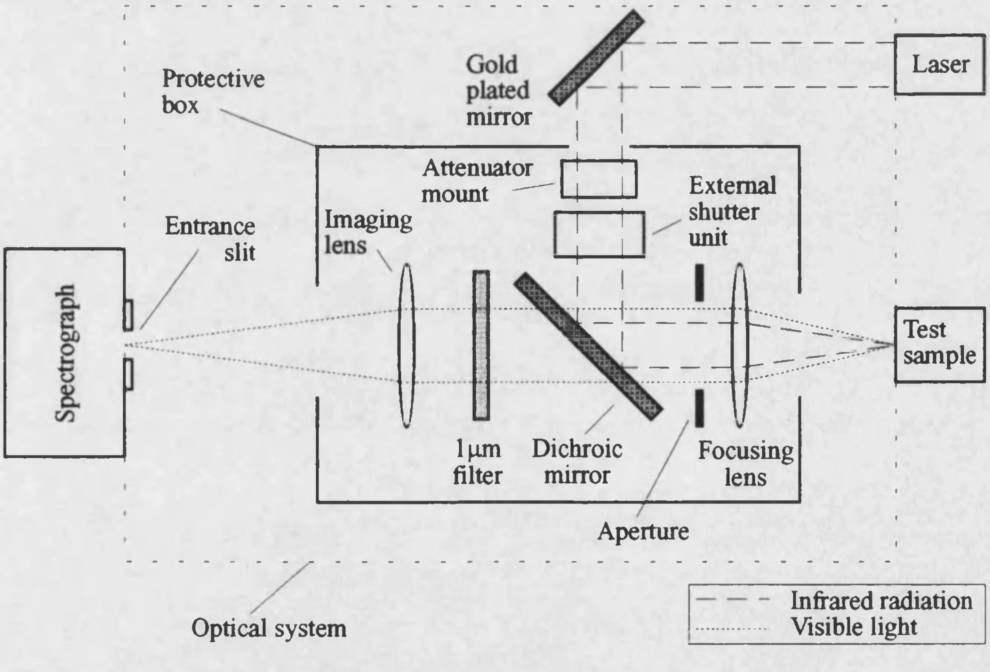

Figure 3.3. The optical system (plan view).

When the internal laser shutter is opened, the beam exits the laser cavity, is reflected through 90° by the gold plated mirror and directed, via the attenuator mount and external shutter, onto the dichroic mirror. Due to its orientation in the system, the dichroic mirror directs the incident laser beam onto the sample via the focusing lens whilst allowing the visible light emitted from the hot sample to pass back through the imaging lens towards the spectrograph.

The protective box shields the operator from any stray laser radiation whilst allowing the passage of laser and visible light, as appropriate. Hence, it is only when the external shutter is opened that any laser light is able to leave this box and be focused onto the test sample. (Beam tubes are used to contain all laser radiation travelling between the laser and external shutter unit). The addition of two cylindrical lenses, between the imaging lens and the spectrograph, improves the resolution of the detection system and will be discussed in section 3.2.6.

The operations of the individual components are now described separately.

3.2.1. GOLD MIRROR

Due to restricted space on the optical bench on which the optical system is mounted, it is necessary to turn the laser beam through 90°. A gold coated mirror is used because its high reflectance of infrared radiation protects it from laser damage and beam absorption losses can be minimised. Although there is some loss in laser energy at this point in the optical system, it is only of the order of 0.6% (Abelès, 1966) and can thus be ignored in future calculations.

3.2.2. ATTENUATOR MOUNT

Insufficient stability in laser output has been observed at low operating powers (section 5.1.4) and so an attenuator mount, into which neutral density filters can be slotted when required, is positioned between the gold mirror and the external shutter. Three filters made of ultra-pure fused silica, each with an optical density of 0.3 (corresponding to a beam power attenuation of ~26%) are available. Either one, two, or all three filters may be used in combination to reduce the power of the laser beam.

Thus the laser may be operated at a moderate power and the beam attenuated by either 26%, 45%, or 59% as appropriate.

3.2.3. EXTERNAL LASER SHUTTER

The external laser shutter is made from a piece of brass foil, with a reflective gold coating, which is mounted on the top of a relay. When the shutter is open the laser beam is allowed to pass through to the dichroic mirror, and when closed, reflected into a beam dump as shown in figure 3.4.

The relay is controlled from an ante-room by a control unit connected to the interlocking system which ensures that whenever the connecting door is opened, the external shutter closes automatically. The addition of this shutter to the existing optical system allows the radiation within the laser cavity to remain undisturbed, thus maintaining a steady laser output and allowing a series of temperature profile measurements to be performed using the same stabilised laser current.

The external laser shutter is also vital in controlling the time between the start of the laser heating pulse and data acquisition and is discussed further in section 3.3.3.

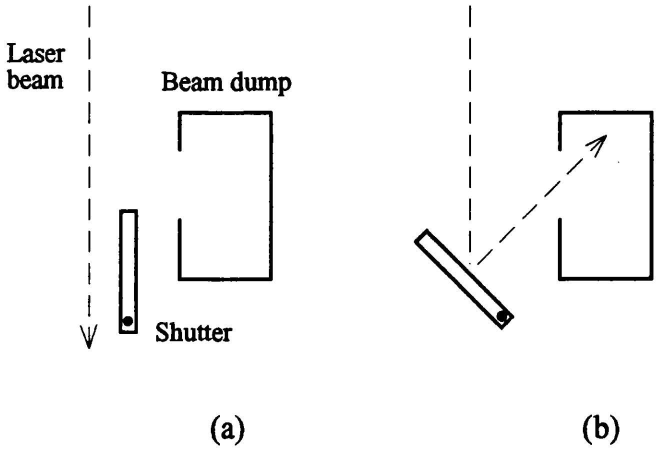

Figure 3.4. Plan view of the external laser shutter: (a) open, (b) closed.

3.2.4. THE DICHROIC MIRROR

Dichroic mirrors are colour selective beam splitters which transmit and reflect particular wavelengths. In the main they are constructed from anisotropic crystals, and fall into two main groups: 'hot' and 'cold' mirrors. Hot mirrors reflect infra-red ('hot') radiation whilst cold mirrors reflect visible ('cold') radiation. The dichroic mirror used here is a hot mirror, the typical transmission and reflection characteristics of which are shown in figure 3.5.

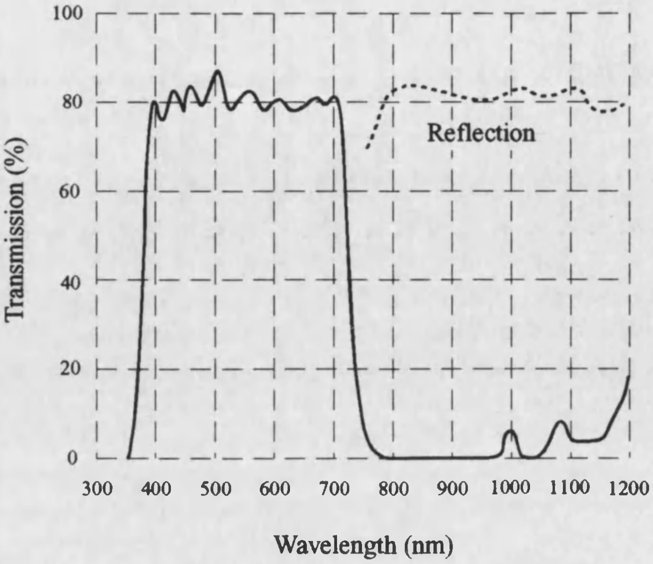

Figure 3.5. Typical transmission and reflection characteristics of a hot mirror.

Two observations can be made from figure 3.5: the mirror's transmission across the visible range of the spectrum is not uniform, its reflectance of infra-red radiation is not absolute. The experimental consequences are that a sensitivity correction has to be performed (see section 4.3.3), and that a high pass (1μm) filter must be placed behind the mirror to block any laser light it transmits (shown in figure 3.3). In addition, the construction of the mirror results in multiple reflections from its surface. An aperture is positioned between the dichroic mirror and the focusing lens shown in figure 3.3 to remove all but the central, most intense reflection. Although this ensures that the image arriving at the sample remains a simple Gaussian (confirmed by experimental measurements described in section 5.1.2), the total loss in power may be as much as 30% (Lambda Photometrics engineer, private communication).

3.2.5. FOCUSING AND IMAGING LENSES

A lens with a focal length of 70mm is used to focus the laser beam onto the test sample and a lens of 300mm focal length to focus the hot spot image onto the entrance slit of the detector; the focusing and imaging lenses shown in figure 3.3. Ladds (1994) considered this two lens system in some detail and concluded that the ratio of their focal lengths may be used to predict the magnification of the hot spot image formed at the detector according to,

$$M = \frac{I}{S} = \frac{f_i}{f_f}, \tag{3.2}$$

where M is the image magnification, I the diameter of the image formed at the detector, S the diameter of the hot spot in the sample plane, f_i the focal length of the imaging lens and f_f the focal length of the focusing lens. Substitution of 300mm and 70mm for f_i and f_f respectively in equation 3.2 yields an image magnification (M) of 4.29. Thus, the image formed on the CCD detector face is 4.29 times larger than the original hot spot created on the surface of the test sample by the laser. The formation of the magnified image is discussed further in section 3.2.6.

The focusing lens forms an integral part of the Laser Corporation viewing and focusing apparatus and cannot be easily removed. Therefore, a change in image magnification is achieved by exchanging the imaging lens for one with a different focal length.

3.2.6. CYLINDRICAL FOCUSING SYSTEM

A condition of the data analysis procedures, section 4.5, is that the entire image of the hot spot must enter the spectrograph entrance slit. If the image remains circular, see figure 3.6(a), the image entering the spectrograph slit will be small and there will be little spatial resolution as the image will only cover a small area of the CCD detector surface. To improve resolution, the size of the circular image is increased by choosing a long focal length imaging lens, see figure 3.6(b). Although this causes a larger area of coverage on the CCD detector the image is now wider than the spectrograph entrance slit and hence invalidates the mathematical analysis. This problem is overcome by using a cylindrical lens system to compress the image into an ellipse as shown in figure 3.6(c).

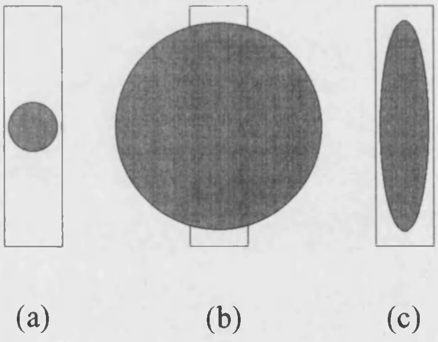

Figure 3.6. Image formed within the entrance slit of the spectrograph: (a) circular image contained entirely within slit, (b) magnified circular image, (c) image compressed by cylindrical lenses.

Two cylindrical lenses are introduced to the optical system as shown in figure 3.7. Their purpose is to compress the hot spot image in the horizontal direction whilst leaving it unchanged in the vertical direction. Lens C_1 creates an intermediate focus in the horizontal direction: this is not a true focus point since the beam has undergone no additional focusing in the vertical direction. Lens C_2 moves the horizontal focus of the beam to the focal point of the imaging lens, but like C_1 has no effect in the vertical axis. The image formed at the spectrograph slit has therefore been horizontally focused by lenses C_1, C_2, and the imaging lens, and vertically by the imaging lens alone. The resultant image is a tall thin ellipse. As a result the entire image of the hot spot enters the slit and covers a large number of vertical CCD detector pixels.

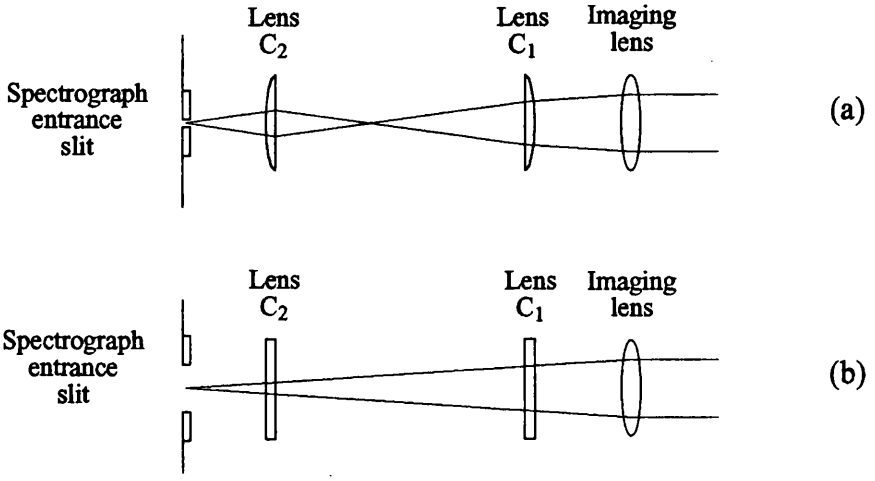

Figure 3.7. Use of cylindrical lenses to compress the hot spot image in the horizontal direction: (a) plan view, (b) side view.

3.3. THE DETECTION SYSTEM

A spectrograph and charge coupled device (CCD) form the core of the detection system. The spectrograph is used to form a 'wavelength sorted' image of the hot spot formed on the sample surface, which is then recorded by the CCD. Dedicated software run on a PC is used to manipulate this information to provide numerical data for further analysis. The entire system is controlled by the laser interlocking and control circuits.

3.3.1. THE SPECTROGRAPH AND CCD

The compressed image formed by the optical system enters the entrance slit of a Jobin Yvon CP200 spectrograph where it is split into its separate wavelength components and detected by an EG&G Model 1430-P CCD. The detector face is comprised of 576 × 384 silicon detector pixels, each one 23μm square, giving a total area of 13.248mm × 8.832mm. An electro-mechanical shutter governs the exposure time of the detector. Two cooling systems, a Peltier cooler mounted on the detector face, and a liquid coolant run through the detector, are employed to reduce thermally generated noise in the collected data by maintaining a detector temperature of between -15°C and 5°C. The formation of water droplets and ice crystals on the detector face is inhibited by passing nitrogen gas around the main detector casing. A de-humidifier in the laboratory is used to reduce ambient humidity.

Figure 3.8 shows the arrangement of the plane mirror and supercorrected holographic diffraction grating used to reflect the image of the hot spot formed in the entrance slit of the spectrograph, onto the detector face.

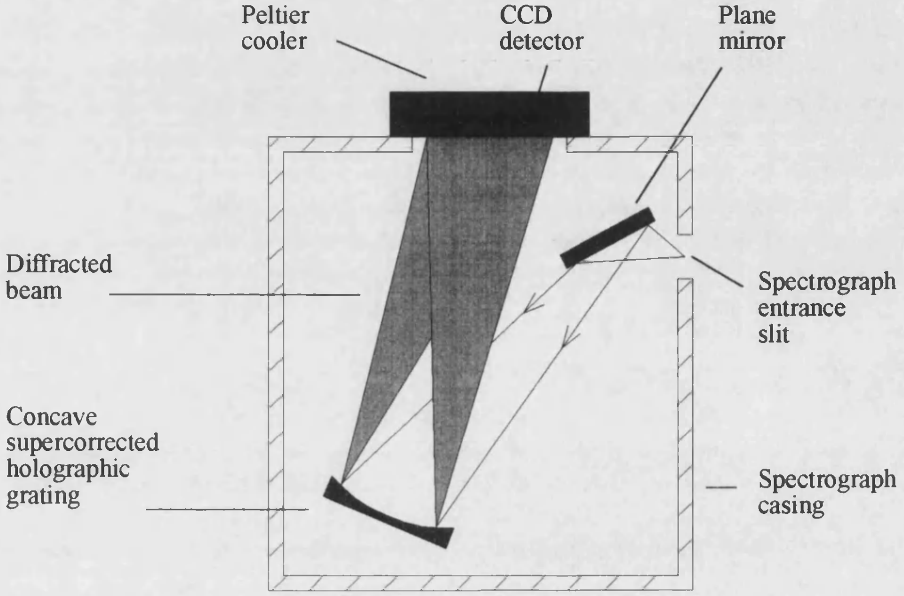

Figure 3.8. Spectrograph and CCD assembly.

To explain the operation of the spectrograph, first consider a monochromatic image formed at its entrance slit. The image is reflected by the plane mirror onto the grating and then diffracted onto the detector, which is positioned in the focal plane of the grating. An exact copy of the original image is formed on the detector with its horizontal position determined by its angle of diffraction off the grating, and hence its wavelength.

The image of the laser heated spot formed at the entrance slit of the spectrograph has a continuous wavelength distribution, and so a continuum of overlapping images is formed on the detector face. Provided that the spectrograph slit is sufficiently narrow (50μm or less), the extent of this overlap, or wavelength convolution, has been shown (Tytler, 1995) to make no significant difference to the calculated temperature profiles.

The data retrieved from the CCD is in the form of a two dimensional array where one dimension contains all the spectral information, and the other all the spatial information across the image of the hot spot. In this text, the horizontal lines of pixels are referred to as wavelength slices, and vertical lines as vertical tracks. A wavelength slice describes the variation of intensity with wavelength in a narrow strip of the hot spot image, whilst a vertical track describes the variation of intensity with position across the image at a particular wavelength.

The CCD on which this image is recorded forms part of an Optical Multichannel Analysis (OMA) system manufactured by EG&G Instruments. The detector cooling system, the shutter operation and signal digitisation are all governed by a model 1430-1 detector controller. This contains a 14 bit analogue to digital converter to enable measurements of a possible 16384 discrete intensities. An IEEE (1464 scan control) interface passes signals between the controller and a 486 PC. The OMA2000 software supplied by EG&G with the equipment is used here to govern the entire detector operation.

3.3.2. TIME DELAY UNIT

To permit a pre-selected delay to occur between the commencement of laser heating and data acquisition, a programmable delay unit was built. The inclusion of this unit in the interlocking and control circuit (described in section 3.3.3) allows a study of the test sample temperature as a function of time (experimental results are presented in section 7.1.6). A schematic diagram of the time delay unit is given in figure 3.9. A full circuit diagram, and the logic circuit which connects the unit to the OMA system are given in appendix A.

The operator sets the length of the required delay with three BCD (binary coded decimal) switches[1] mounted on the front of the unit. The first switch sets the number of required seconds, the second sets 10ths of seconds, and the third 100ths of seconds, to give a possible range of 10ms to 9990ms.

When the external shutter is opened, the delay unit receives a signal from the shutter controller (see section 3.2.3) and a train of clock pulses is sent to three cascaded BCD decade counters[2] which start counting. The clock pulses are provided by a 16MHz miniature crystal oscillator[3] which is frequency divided (on the chip itself) to 1MHz, and four more cascaded BCD decade counters which further divide this frequency to 100Hz.

---

[1] RS components. Stock number 337-447.

[2] Motorola LS162A.

[3] RS components. Stock number 296-891.

At each clock pulse the output from the first counter is compared with the output of the first of the BCD switches by a 4 bit magnitude comparator[1]. The same procedure is adopted for the other two counters and switches. When the outputs from each of the counters and their associated switches match, a signal is sent to the OMA system causing the CCD shutter to open and the clock pulses to stop. The counters are automatically reset when the operator closes the external laser shutter. The time delay unit thus acts as a means of controlling the time between laser heating and temperature measurement.

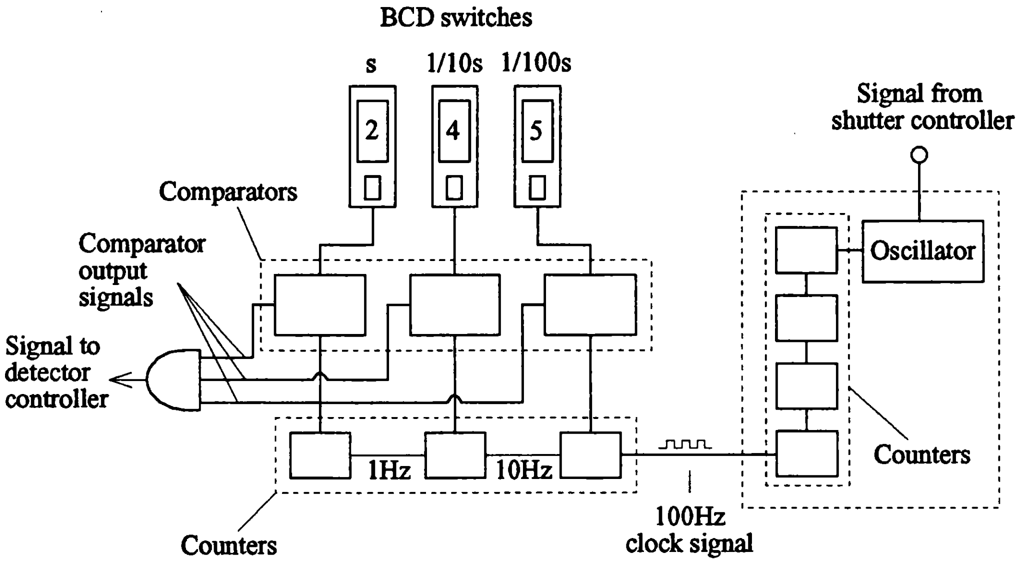

Figure 3.9. Schematic diagram of the time delay unit (with the BCD switches set to 2.45s).

---

[1] National Semiconductor Corporation DM74LS85.

3.3.3. THE INTERLOCKING AND CONTROL CIRCUITS

An interlocking system, which is described fully by Ladds (1991), is used to ensure that the external laser shutter closes when the door to the laser room is opened, and forms the basis of a control circuit which connects the PC (on which the OMA software is run), the external shutter controller, the time delay unit, and the detector controller. The control circuit is shown schematically in figure 3.10.

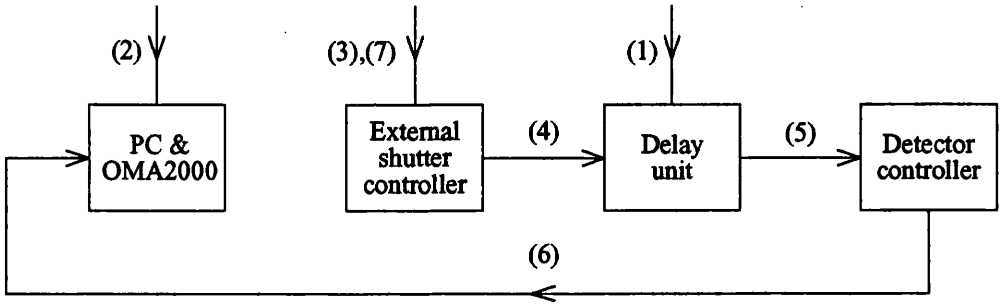

Figure 3.10. Schematic diagram of the control system with individual experimental procedures numbered.

Each of the numbered processes shown in figure 3.10 is described below.

1. The operator sets the delay required between the opening of the laser shutter and the commencement of data acquisition.
2. The operator sets the required CCD scan set up and exposure time using the OMA software, see section 4.4.2.
3. The operator opens the external shutter.
4. A signal is sent from the shutter controller to the delay unit and it starts counting.
5. Once the delay unit has counted to the time set by the operator, it sends a signal to the detector controller to open the CCD shutter.
6. After the pre-set exposure time the CCD shutter closes and the experimental data is transferred to the PC.
7. The operator closes the external laser shutter and the apparatus is ready for the entire process to be repeated.

The complete experimental procedure, of which this process is only a part, is described fully in chapter 4.

3.4. CONTAINMENT AND POSITIONING OF THE TEST SAMPLE

3.4.1. PHYSICAL DIMENSIONS OF THE TEST SAMPLE

The controlled atmosphere chamber designed specifically for the research described in this thesis, and described fully in the next section, has a metal plate on which the test sample is mounted. For the sample to fit this plate it must be less than 20mm long and 5mm wide. However, in order to reduce edge effects it is preferable for the sample to be as large as possible whilst remaining within these limits. The thickness of the sample is less critical, although it must be sufficiently thick to maintain a flat surface. For most of the samples used this was approximately 1.5mm. Note that the sample mounting plate was made specifically to hold urania samples supplied by AEA Technology which were approximately 15mm×2mm×4mm.

Other properties desirable in an effective test sample were introduced in section 2.2 and are discussed further in chapters 6 and 7.

3.4.2. THE CONTROLLED ATMOSPHERE CHAMBER

Although the detection and analysis systems described were designed for ultimate use with a diamond anvil cell, all of the experimental work described in this thesis was performed at ambient pressure in a controlled atmosphere chamber (CAC) which was built ‘in-house’. The specification for this apparatus was to provide accurate positioning of the test sample whilst maintaining it in either a specific or inert atmosphere. The purge gas used depends upon the test material and is discussed further in chapter 7.

The CAC is a stainless steel construction consisting of three main sections: a base plate, a sample mounting plate, the main casing. A simplified view of the entire construction is shown in figure 3.11, but note that the sample mounting plate is located inside the main casing and is not visible in this figure; it is shown later in figures 3.12 and 3.13. The base plate is attached to an x-y-z positioning stage constructed from three micropositioners and a right-angled bracket. The whole assembly is mounted on an optical bench via a spacer block which ensures that the y-axis micropositioner operates over the required range. Slotted holes in this block also permit the coarse adjustment of position along the z-axis (laser axis).

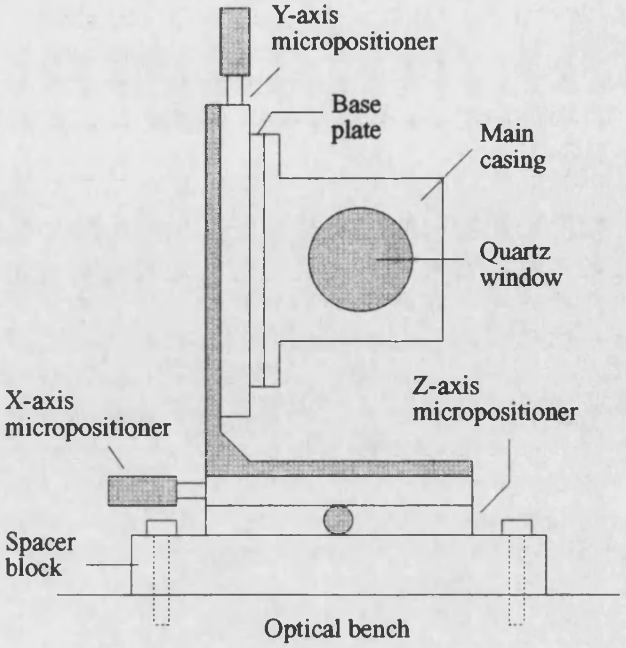

Figure 3.11. Simplified view of the controlled atmosphere chamber and positioning apparatus.

THE BASE PLATE

The base plate is fixed to the positioning stage and has the sample mounting plate attached to it via four threaded posts, as shown in figure 3.12. Four wing nuts are used to hold the mounting plate securely in place. The base plate has an O ring embedded in it to provide an airtight seal with the main casing (shown later in figure 3.14). The base plate was manufactured to very strict tolerances because it is imperative that the surface of the test sample remains perpendicular to the laser axis.

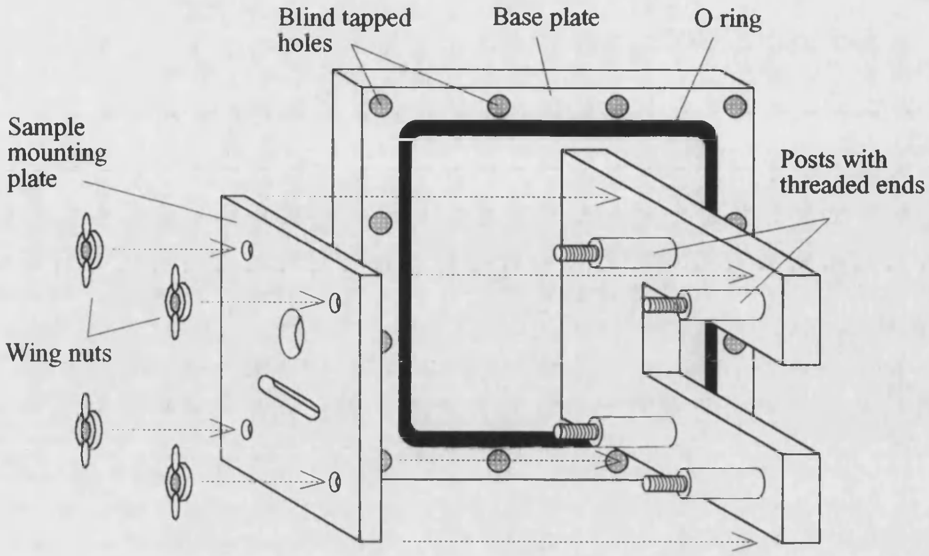

Figure 3.12. CAC base plate construction.

SAMPLE MOUNTING PLATE

The sample mounting plate holds not only the test sample but also a piece of steel shim which is used in positioning the CAC along the laser axis (see section 4.2), and in the calibration procedures described in section 4.3. To explain the assembly of this plate, figure 3.13 shows individual stages of the sample mounting process.

Figure 3.13(a) shows the basic design of the plate. Two recesses, in which the sample and shim are placed, have been milled to the same depth with a hole behind each to allow laser beam access. The test sample lies directly on the plate, but the shim is thermally insulated from it by strips of Kapton®[1] which are laid on top of,

---

[1] Kapton is a polyimide film with a thermal conductivity of between 0.10 and 0.35 $Wm^{-1}K^{-1}$ at 23°C. A complete material specification is given by Goodfellow (1994) .

and beneath the shim as shown in figure 3.13(b). These insulate the shim from the plate thus allowing the laser beam to raise the temperature of the shim high enough to burn a hole through it; the purpose of this procedure is discussed in chapter 4. The calibration procedures, described in section 4.3, require the surface of the test sample and shim to lie equidistant from the laser along the beam axis. However, the use of the Kapton strips violates this condition and a correction must be made by moving the whole CAC using the micropositioning stage. Once the test sample, shim, and Kapton strips are in place, two securing plates are used to hold everything firm. These are shown in figure 3.13(c).

During the wavelength and sensitivity calibration procedures (see section 4.3), a light is shone through the pin hole created in the shim and collected by the spectrograph and CCD assembly. To prevent any light other than that through the pin hole from falling on the spectrograph slit, a sample cover plate is fitted across the sample as shown in figure 3.13(d).

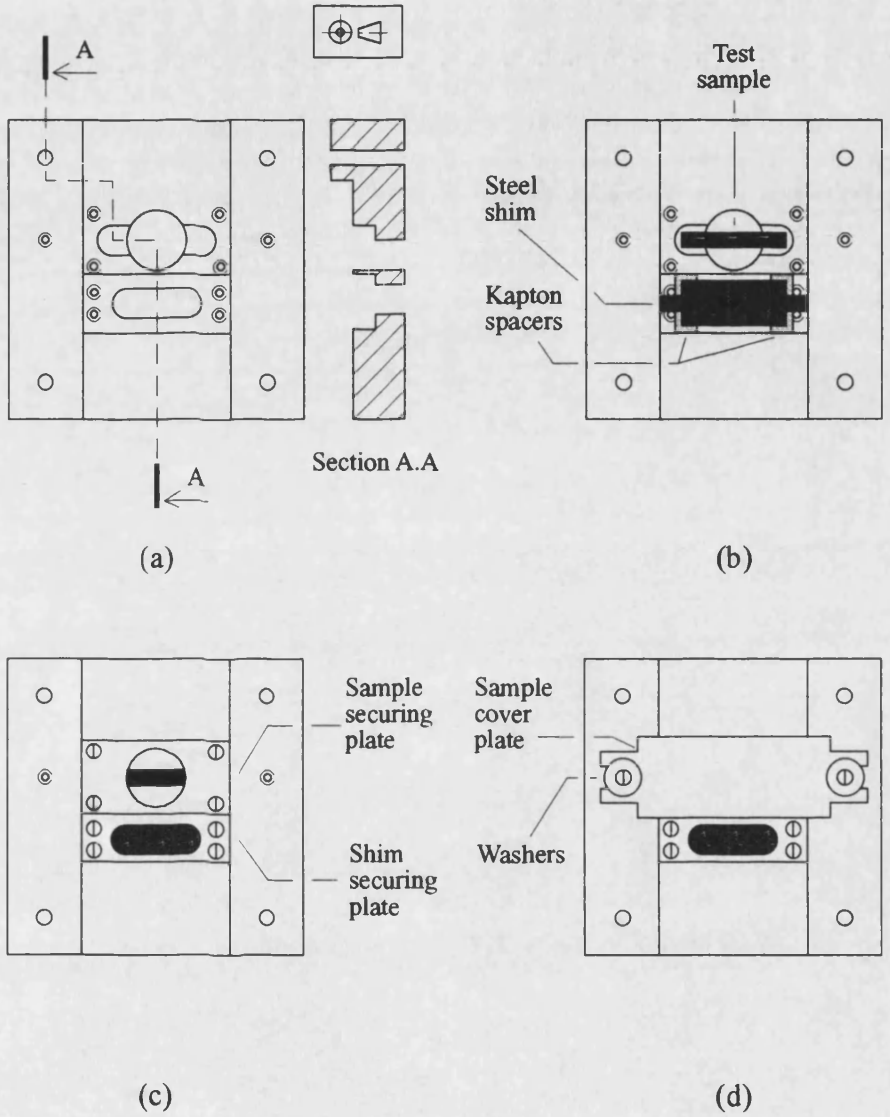

Figure 3.13. Individual stages of mounting a test sample and shim on the sample mounting plate for laser heating in the CAC. (a) Sample mounting plate: (b) with sample and shim in place, (c) with securing plates in place, (d) with sample cover plate in position. Note that the laser beam direction is out of the page.

MAIN CASING

The main chamber casing consists of a flanged box which bolts onto the base plate with twelve socket cap screws, as shown in figure 3.14. An O ring positioned in a milled groove in the base plate lies beneath the flange to make the seal between the base plate and the main casing airtight. The main casing has two threaded holes machined in it, into which the window assemblies (also shown in figure 3.14) are screwed. Each of these assemblies consists of two metal plates with a quartz window sandwiched between them. O rings are used to make the seals airtight. Note that only one window is shown in figure 3.14, but that two windows are required to allow back illumination of the pin hole, which is described in chapter 4. The second window is positioned on the opposite side of the main casing.

To position the sample mounting plate in the CAC, one of the window assemblies is removed, the mounting plate inserted through the hole in the main casing, and the assembly replaced, thus avoiding the need to dismantle the CAC each time a new sample is used. The location of the threaded posts shown in figure 3.12 is such that when the mounting plate is positioned in the CAC, the test sample and shim are located in the centre of the quartz windows.

The required purge gas is passed through the CAC via two gas pipes connected to the main casing as shown in figure 3.14. The gas inlet pipe connects directly to the regulator of the gas bottle used, whilst the gas from the outlet pipe passes through a gas bubbler and out of the laboratory through a roof vent.

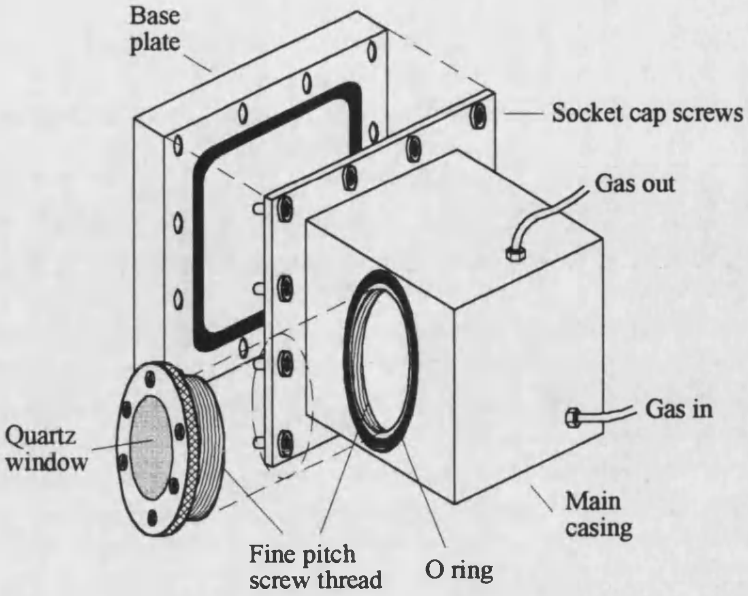

Figure 3.14. Main casing of the controlled atmosphere chamber.

(The base plate has been left incomplete for clarity).

CHAPTER 4

4. TEMPERATURE PROFILE MEASUREMENT

The process by which a temperature distribution is created on the face of the test sample and then measured employing the principles discussed in chapter 2 may be divided into five parts:

1. A suitable test sample has to be cut and polished, and mounted in the controlled atmosphere chamber (CAC) .
2. The CAC must be correctly positioned.
3. Various alignment and calibration procedures must be performed.
4. The Nd:YAG laser is used to create a hot spot on the sample, the image of which is manipulated and stored in the form of a two dimensional data array.
5. The collected data is mathematically converted to a radial temperature distribution which may be used for further analysis.

4.1. SAMPLE PREPARATION

4.1.1. CUTTING AND SURFACE PREPARATION

The urania samples used for the work described in this thesis were supplied by AEA Harwell as small blocks approximately 2mm×15mm×4mm. Due to the radioactive and toxic nature of the material, no further processing could take place 'in-house' and they were used as supplied. All other samples were prepared in the School of Physics, with assistance from the School of Materials Science in some instances.

Samples were cut using either a Discotom silicon carbide disc cutter, or an Anshaw Instruments low speed peripheral diamond blade saw, to achieve a size nominally equivalent to that of the urania samples. They were then attached individually to the mounting plate of a PP5 precision polishing jig using a cyanoacrylate adhesive, and lapped and polished on a Logitech PM2 polishing machine. Lapping was achieved with a silicon carbide powder and Hyprez polishing oil on a cast iron plate until the sample thickness was approximately 2mm. Greyed surfaces were given no further preparation although polished ones were given an additional treatment using Hyprez fluid and 6μm diamond impregnated paste on a solder plate. Thus, the resultant samples were extremely flat and had either greyed surfaces or had been polished to remove surface damage caused by the lapping process. The experimental implications of these different surface preparations are discussed in section 6.1.1.

4.1.2. MOUNTING A SAMPLE IN THE CAC

The test sample and steel shim are positioned on the sample mounting plate as shown in figure 3.13 on page 78. One of the quartz window assemblies is removed to permit the sample mounting plate to be inserted into the CAC and attached to the base plate as shown in figure 3.12 on page 76. The window assembly is replaced.

SAMPLE MAPPING

Because the laser interlocking system does not permit the operator to enter the same room as the laser whilst the external shutter is opened, the position of the test sample and shim, in terms of micropositioner settings, must be determined by some other means before laser heating commences. This is achieved as follows.

The output power monitor (see figure 3.2 on page 56) is removed and a HeNe (visible) laser shone through the Nd:YAG cavity, the optical system, and onto the test sample. By adjusting the x- and y-axis micropositioners, the spot formed by the HeNe laser can be moved about the sample surface and the x and y co-ordinates of the sample edges found. This process is repeated for the shim in order to locate a suitable site for the laser drilling of a hole for the calibration procedures described in section 4.3.

So that a record may be kept of the exact position on the sample corresponding to a particular data set, the above information is used to map the surface of the test sample with a series of numbered heating sites. The surface of an iron sample after a series of laser exposures using this technique is shown in figure 4.1.

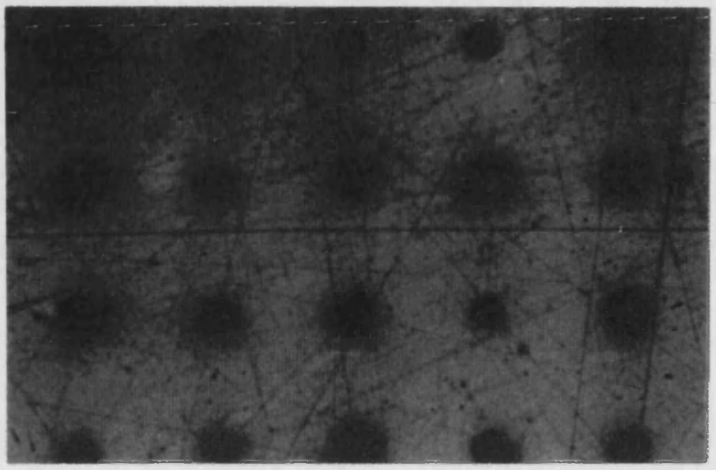

Figure 4.1. Surface of an iron sample after laser heating, to demonstrate the effect of the surface mapping procedure.

The optimum separation and position of the test sites is considered further in section 6.6.2.

4.2. POSITIONING THE TEST SAMPLE

Laser characterisation (section 5.1) is used to find the position of the beam waist caused by the focusing lens, and the correct location of the spectrograph is then calculated from the application of geometric optics to the lens system shown in figure 3.3 on page 58. However, both of these techniques are susceptible to inaccuracies so that the spectrograph may not be at its optimum position after their completion. To compensate, the CAC is moved along the laser axis, while ensuring that the test sample remains within the depth of focus of the laser beam, until the image of the hot spot is correctly located at the entrance slit of the spectrograph. This is achieved as follows:

A hot spot formed on the test sample is simulated by back illumination of a pin hole located at the sample position. This is done by first using the Nd:YAG laser to burn a hole through the steel shim located on the sample mounting plate. (Note that the shim does not need to lie exactly at the beam waist for this to occur). A calibrated white light source is then shone through this hole and the CAC moved backwards and forwards through the region surrounding the beam waist by adjustment of the z-axis micropositioner (see figure 3.11 on page 75). The CCD is used to record the image of the light through this hole for different z-axis CAC positions. (The use of the CCD to record an optical image is described fully in section 4.4.) The CAC position for which the intensity of the white light image is at a maximum will ensure a focused image at the spectrograph. The practical need for the shim and sample to lie at different distances along the beam axis was discussed in section 3.4.2, and care must be taken to ensure that the CAC is moved by 130μm (the thickness of the Kapton® strips) between use of the shim and sample.

The spectral response of the dichroic mirror, which was discussed in section 3.2.4, introduces a series of peaks to the data recorded by the CCD. As the

CAC is moved backward and forward along the laser axis, the relative heights of these peaks change. The peak intensities measured across a single horizontal slice of the white light image as a function of wavelength position are plotted in figure 4.2. Each line represents a series of measurements at a different CAC position (solid lines to one side of the focus, and dashed lines to the other).

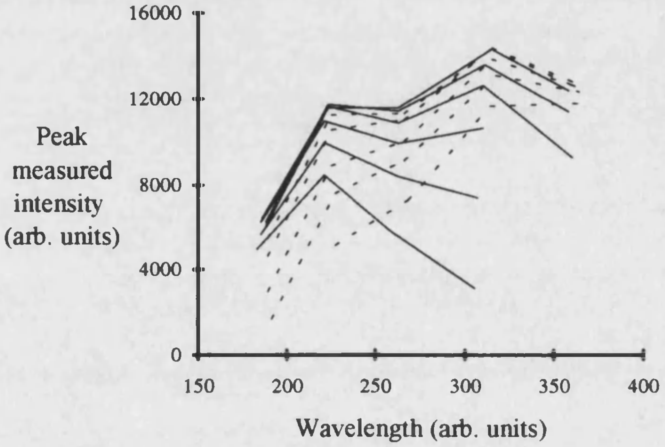

Figure 4.2. Peak measured intensities for different CAC positions.

It is apparent from figure 4.2 that the heights of each peak in the intensity distribution rise to a maximum and then fall again as the CAC is moved through the optimum position. To determine accurately this location, the intensity of the highest peak has been measured as a function of CAC position for two different CCD exposures. Results are presented in figure 4.3.

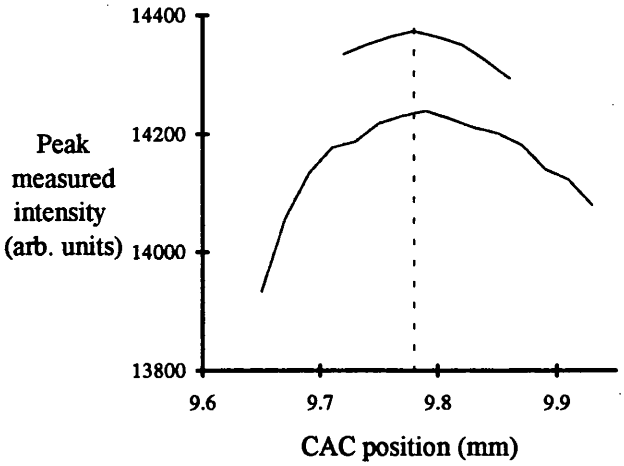

Figure 4.3. Peak intensity as a function of CAC position.

In both cases the peak intensity occurs for a CAC position of 9.78mm on the optical rail. Hence the CAC must be located at z=9.78mm for the shim to be at the beam waist, and at z=9.65mm (9.78mm less 0.13mm allowing for the thickness of the Kapton® strips) for the test sample surface to be at the beam waist position. Note that a CAC z-axis position of 9.78mm is later referred to as z_0.

4.3. ALIGNMENT AND CALIBRATION

The alignment and calibration of the experimental system may be divided into two parts: routine operations which are done at regular intervals, and those that are required before the acquisition of each set of experimental data. Laser beam characterisation (which has already been described in section 2.1) and optical system alignment fall into the first category, whereas wavelength and sensitivity calibrations belong to the latter.

4.3.1. OPTICAL SYSTEM ALIGNMENT

In order to maintain a correctly aligned optical system, it is necessary to check the alignment of the individual optical components at regular intervals. During data acquisition, any asymmetry of the hot spot image indicates the presence of severe misalignment of the optical system (discussed further in section 4.4.4).

The Nd:YAG laser used here is a high power laser which operates in the infrared region making it an impractical light source for alignment of the optical system components. For this reason a HeNe laser, operating in the visible part of the spectrum (632nm), is used. The output power monitor of the Nd:YAG laser is removed to allow access to the laser cavity through the rear mirror, and the HeNe laser beam shone through it. Each of the lenses and mirrors is adjusted in turn until the beam is observed to remain horizontal and follow the optical path shown in figure 3.3 on page 58. The lateral position of the spectrograph, and the rotational alignment of the CCD with respect to the spectrograph, must also be adjusted to ensure that the image recorded by the CCD is 'square' with relation to the detector pixel grid. The output power monitor is replaced to permit operation of the Nd:YAG laser.

4.3.2. WAVELENGTH CALIBRATION

Before use, the CCD must be calibrated for wavelength to enable a direct inference of absolute wavelength from the horizontal position of an image on the detector face. This is done as follows:

The HeNe laser is shone through the pin hole made in the shim (section 4.2). A CCD scan is taken and the pixel position of the wavelength peak (p_{HeNe}) identified by the OMA2000 software. The manufacturer of the spectrograph quotes a spread of 39.68μm on the CCD for a 1nm range of wavelength incident on the grating. This corresponds to a value of 0.5797nm for the wavelength increment (m) between adjacent detector pixels. The base wavelength (λ_B), which is the wavelength corresponding to the first pixel on the CCD array, may then be found from

$$\lambda_B = \lambda_{HeNe} - mp_{HeNe}, \tag{4.1}$$

where λ_{HeNe} is the wavelength of the HeNe laser (632nm). Substitution for λ_B in the analysis programs (section 4.5) allows the direct conversion of horizontal detector position to wavelength.

4.3.3. SPECTRAL SENSITIVITY CALIBRATION

The dichroic mirror which forms part of the optical system, has a complex spectral response (see section 3.2.4) and so although the light emitted by the hot spot on the test sample follows a typical Planck intensity/wavelength distribution (section 2.3.1), the light recorded by the CCD does not. To overcome this problem, a spectral sensitivity calibration must be performed.

A calibrated white light source, for which the spectral intensity as a function of wavelength has been tabulated (NPL certificate of calibration, 1986), is shone through the pin hole created in the steel shim on the sample mounting plate (section 4.1.2). A CCD scan is taken and recorded. A comparison of this information and the known intensity/wavelength relationship of the lamp enables a spectral calibration of the system; this is described in section 4.5.1. A new calibration is performed for each group of experimental results.

The measured spectral intensity response of the calibrated light source may be written $M(\lambda_i,x_j)$, where λ_i represents the i'th pixel on the wavelength axis, and x_j the j'th pixel on the spatial axis, of the CCD pixel array. The temperature of the lamp is assumed to be spatially constant, and so $M(\lambda_i,x_j)$ can be written $M(\lambda_i)$. Spectral correction coefficients $C(\lambda_i)$ are calculated according to

$$C(\lambda_i) = \frac{P(\lambda_i)}{M(\lambda_i)}, \qquad (4.2)$$

where $P(\lambda_i)$ is the tabulated intensity/wavelength relationship of the calibrated lamp. $P(\lambda_i)$, and typical values of $M(\lambda_i)$ and $C(\lambda_i)$ are shown in figure 4.4.

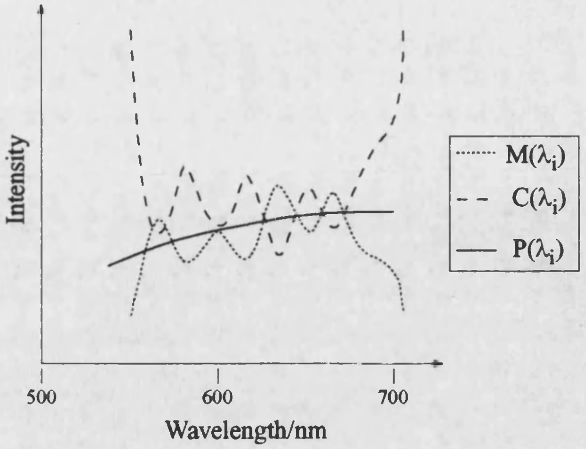

Figure 4.4. Schematic of the measured spectral response M(λ_i), Planck distribution P(λ_i), and spectral correction factors C(λ_i) for the calibrated white light source.

Note that the measured intensity of the white light source is low at either wavelength extreme, and the correction factors very large. To avoid anomalies in the resultant temperature calculations, data which has a correction factor above a chosen limit will be omitted from any subsequent analysis. (The value at which this limit is set can have quite a significant effect on the resultant temperature distributions and is considered further in section 5.3.2.)

4.4. DATA ACQUISITION

4.4.1. EXPERIMENTAL SYSTEM PREPARATION

The delay imposed by the time delay unit must be set, and the appropriate purge gas chosen. In most cases argon is used to inhibit oxide formation on the sample surface, although a hydrogen/argon mixture is required for urania (discussed further in section 7.1). The gas is passed through the CAC and into a gas bubbler at the rate of two to three bubbles a second. Approximately fifteen minutes are usually allowed for all of the air in the system to be displaced prior to any heating experiments.

The laser is switched on and allowed to run for several minutes before the stabiliser is used to smooth its output. A delay is allowed because there tends to be a drift in output laser power for several minutes after switching on the flash lamp. During this 'warm-up' period, dry nitrogen is passed over the CCD detector face to dry it. Initial experiments indicated that if the apparatus had not been used for a few days, several hours were needed to dry the face completely; when in regular use, ten minutes are sufficient. The water for the liquid cooler may then be turned on, and then the detector controller itself. Once the temperature of the detector has reached -5°C, the equipment is ready for use.

4.4.2. SETTING THE OMA2000 SYSTEM PARAMETERS

Before data acquisition commences the operator has to set the scanning parameters and CCD exposure time.

SCANNING PARAMETERS

In full window mode, the CCD measures the light intensity incident on an array of 576×384 pixels. However, in most cases many of the vertical tracks will have no light falling on them. To make the data measurement faster and the subsequent analysis less cumbersome, the operator can select a region of the array to be inactive.

The OMA2000 program may be configured to collect data from repeated CCD exposures and then average them. Under steady state conditions it is wise to do this in order to reduce the effects of random error, but if the sample has not attained thermal equilibrium, multiple data acquisitions will combine images of hot spots with different temperature distributions, thus producing an inconsistent result. In such cases it is provident to record data for a single CCD exposure.

CCD EXPOSURE TIME

The appropriate exposure time of the CCD must be set by the operator. If it is too long the image will saturate the detector, or 'top-out', and if it is too short, information at lower intensities will be lost and the subsequent data analysis made more susceptible to inaccuracies.

The experimental implications of CCD exposure times are discussed in sections 5.2.2 and 5.3.2.

4.4.3. CCD IMAGE COLLECTION

Once the laser has been stabilised if required, all the preliminary experiments have been performed, and the OMA2000 scan parameters set, the laser heating of the test sample and experimental measurements may commence.

The external shutter is opened by the operator, the delay unit starts counting until it reaches the predetermined delay set by the operator, and a signal is returned to the OMA system. The CCD shutter opens for the required exposure, the hot spot image is recorded in the form of a two dimensional array, and the data returned to the OMA system for display on the PC screen. The operator closes the external shutter and begins a stop watch to record the time between this and the next exposure of the sample to laser heating. The data is written to a file on the PC hard disk, the OMA2000 program is re-initiated and the test sample moved to its next position. The operator allows the test sample to cool and the entire process may be repeated once the stopwatch has reached a predetermined delay time. The time allowed between successive exposures of the test sample depends upon the type of study being performed and the test material, and is discussed further in chapter 7.

The data returned by the CCD to the PC for each exposure of the sample to laser heating contains the numerical value of the intensity measured at every pixel in the selected detector range. This information constitutes a 'data set'.

4.4.4. DATA VISUALISATION

Immediately after data collection, the OMA2000 software plots the data to screen allowing a preliminary qualitative analysis of the data. A typical data set is shown in figure 4.5.

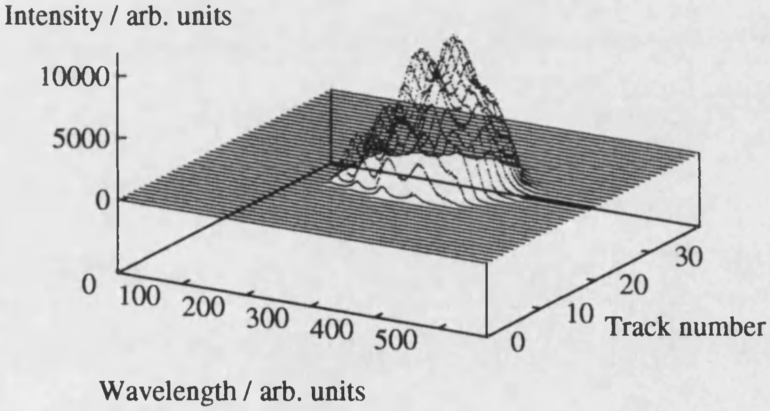

Figure 4.5. Typical data set plotted by the OMA2000 software.

Several important deductions can be drawn from data presented in this form. For example, an immediate check of the peak intensity can be made and the CCD exposure altered accordingly. If the intensity is too low, the exposure must be increased, or if it is too high and 'top-out' of the image is evident, it must be reduced. Also, contamination of the detector surface will be apparent in the form of localised peaks or troughs corresponding to water droplet or ice crystal formation, respectively (see section 4.5.2). Misalignment of the optical system will introduce an asymmetry into the data which is readily visible.

The experimental data may also be viewed later during the data analysis process as an RLE (Run Length Encoded) picture using the Utah Raster Toolkit imaging package which is discussed further in appendix B.

4.5. NUMERICAL ANALYSIS

Several discrete mathematical processes are needed to reconstruct a radial temperature distribution from the two dimensional image of the hot spot recorded by the CCD. These are outlined, in order of execution, in the following sections. The author only aims to provide a general overview of the analysis programs, which were written and have been fully documented, by Ladds (1994).

4.5.1. SPECTRAL SENSITIVITY CORRECTION

The spectral sensitivity correction (introduced in section 3.2.4) is performed using the correction coefficients $C(\lambda_i)$ determined in section 4.3.3.

A raw data set $D(\lambda_i, x_j)$ undergoes a correction for the spectral sensitivity of the dichroic mirror according to

$$D'(\lambda_i, x_j) = C(\lambda_i).D(\lambda_i, x_j) \qquad (4.3)$$

where $D'(\lambda_i, x_j)$ represents the corrected data set.

Note that in practice the application of a set of calculated correction factors will not produce perfectly smoothed data and some ripple will remain, the implications of which are discussed further in section 5.4.2.

4.5.2. ARTEFACT REMOVAL

Initial experimental data demonstrated two types of localised abnormality, which appeared as either light or dark spots on the CCD surface, covering an average area of nine pixels each. It was concluded that water droplet and ice crystal formation were at the root of the problem. By scattering the incident light, ice crystals form a dark spot on the CCD surface, whilst water droplets act as thin lenses to focus the light striking them to a small bright spot. Although practical steps are taken to alleviate this problem (see section 3.3.1), it is impossible to ensure a perfectly dry detector face and if contamination does occur, steps must be taken to remove the resultant noise from the data.

Fourier transform filtering is a general technique for the removal of anomalies in data. By taking the Fourier transform of a data set, the noise will appear in the high frequency components whilst the data will be contained within the low frequency components. The high frequency components can be filtered out by applying a lag window to the transformed data. This is done by including a multiplication factor (λ_k) for each component in the inverse discrete Fourier transform equation to give

$$f(x) = \sum_{k=-\infty}^{\infty} \lambda_k F(k\omega) e^{ik\omega t}. \quad (4.4)$$

The values of the multiplication factors are determined by the shape of the chosen lag window. Although the analysis programs were written to use Heaviside, Tukey-Hanning, or Parzen windows (see figure 4.6), the Parzen window is used by default because it is the least likely to introduce ripple into the smoothed data. The removal of local anomalies from the experimental data requires two dimensional Fourier smoothing, and hence two dimensional lag windows. A more comprehensive description of the application of lag window filtering has been made by Chatfield (1984).

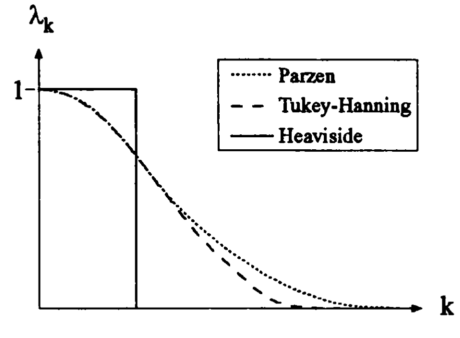

Figure 4.6. A comparison of the Heaviside, Tukey-Hanning, and Parzen lag windows.

4.5.3. DATA SYMMETRISATION

The Abel inversion (section 2.4.3) assumes that the experimental data is axially symmetric about the central horizontal slice, which in theory is true. However, random noise or a minor misalignment of the optical system will invalidate this assumption. Note that any major misalignment of the optical components will have been identified by observation of the raw data on collection, and corrected for. To overcome any remaining asymmetry, the centre slice of the two dimensional CCD image is identified and the data on either side symmetrised.

Firstly the spatial centre is determined by an equal integrals method. This technique is based upon the principle that the total irradiance on either side of the centre of the hot spot image should be equal. The central data position is used as a starting point and a bisection type algorithm used to shift the assumed centre until the integral on either side of it is equal. Although this method is relatively immune to random noise, it will only work successfully for reasonably symmetrical data. Since the optical system is realigned if data asymmetry is observed, this condition is not violated.

Once the central pixel row has been identified, a Fourier transform technique is used to symmetrise the data. Firstly a discrete Fourier transform is performed and the complex part discarded. An inverse discrete Fourier transform is then executed, and again, the complex part rejected. The data which remains is a symmetrised version of the original. A full mathematical description of this technique has been given by Ladds (1994).

4.5.4. APPLICATION OF THE INVERSE ABEL TRANSFORM

Consider a single vertical track of CCD pixels. There is an intensity distribution along the track with a peak at the centre. The information contained within the track corresponds to a monochromatic image of the hot spot. In order to reconstruct the temperature distribution, the radial intensity distribution across the sample surface at each wavelength has to be regenerated in turn. The inverse Abel transform is used to do this.

Consider pixel 1 in figure 4.7. The transform assumes that the intensity of this pixel is equivalent to the total intensity across slice 1 of the radial distribution. The intensity measured by pixel 2 is equivalent to the total intensity across slice 2, and so on. The Abel transform is used to make an estimate of the intensity distribution across slice 2 based upon the information contained in pixels 1 and 2 (since some points in slice 2 have the same intensity as points in slice 1). The intensity distribution across slice 3 is then found from the information contained in pixels 1, 2, and 3 (since some points in slice 3 have the same intensity as points in slices 1 and 2). This process is repeated until the centre point is reached. As the distribution is symmetric, only one half needs to be considered to produce a full reconstruction.

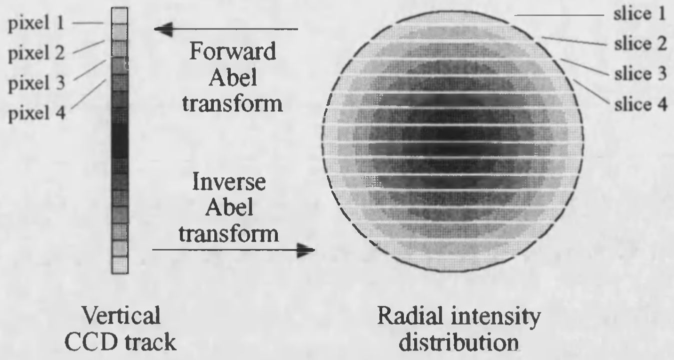

Figure 4.7. Schematic representation of the inverse Abel transform.

4.5.5. TEMPERATURE FITTING

Once the raw data has undergone the analytical processes described in sections 4.5.1 to 4.5.4, the temperature at each radial position may be found in turn, thus reconstructing the original temperature distribution. Two methods each assuming a different thermal radiation law may be used. These are the Planck and Wien laws.

Note that all calculated temperature profiles presented in this thesis are constructed from the surface temperature of the test sample as a function of vertical CCD pixel number, and that data for negative pixel numbers are produced by a reflection of the data for positive pixel numbers.

THE PLANCK LAW

A modified Gauss Newton non-linear curve fitting routine (Bates and Watts (1988), Gill *et al* (1981), Hartley (1961)) is used to fit the experimental data directly to the Planck distribution represented by equation 2.21 on page 49. Initial estimates are made of the sample's temperature and emissivity, and are then substituted into equation 2.21 to generate a first estimate of the intensity/wavelength distribution. This distribution is compared with the experimental data and the sum of squared residuals found. The initial guesses of temperature and emissivity are adjusted accordingly, and the process repeated until the sum of squared residuals has converged to a minimum. This final estimate of temperature is assumed to be the same temperature (within the limits of experimental error) as that generated on the test sample at that radial position.

THE WIEN LAW

The Wien law,

$$I(\lambda, \varepsilon, T) = \frac{2\pi hc^2 \varepsilon \lambda^{-5}}{\exp\left(hc/k_B \lambda T\right)}, \tag{4.5}$$

was discussed in section 2.3.2 as a suitable approximation, at low temperatures, to the Planck law of thermal radiation. Taking natural logs of equation 4.5 and rearranging gives

$$\ln\left(\frac{I}{2\pi hc^2 \lambda^{-5}}\right) = -\frac{1}{T}\frac{hc}{k_B \lambda} + \ln\varepsilon, \tag{4.6}$$

which is linear in terms of reciprocal temperature. By plotting the modified co-ordinate

$$y = \ln \frac{I}{2\pi hc^2\lambda^{-5}}, \tag{4.7}$$

against the modified co-ordinate

$$x = \frac{hc}{k_B\lambda}, \tag{4.8}$$

a straight line with a gradient of $-1/T$, and a y intercept of $\ln \varepsilon$, results; hence temperature and emissivity can be inferred directly.

A linear regression technique is used to find the gradient of the linearised Wien curve. However, because a basic regression method would assume all data points to have equal variance, and because linearisation of the Wien curve and the sensitivity calibration alter the variance of each data point, an iteratively reweighted method is used.

CHOICE OF TEMPERATURE CALCULATION METHOD

Figure 4.8 shows the intensity/wavelength distribution predicted by the Planck law of thermal radiation, together with the experimental wavelength range imposed by the spectrograph grating. It is apparent that below approximately 4000K, the peak of the Planck distribution does not fall within the experimental wavelength range, thus making it an inaccurate method to use below this temperature. However, it has been noted in section 2.3.2 that below 4000K the error between the Wien and Planck distribution is no greater than 1%. Therefore, above 4000K use of the Planck law would appear preferable, whereas below 4000K the Wien law is more appropriate. Note: the better method may not be apparent until temperature fitting has been performed; it is proposed that both methods are used until it is clear which will offer the most accurate result.

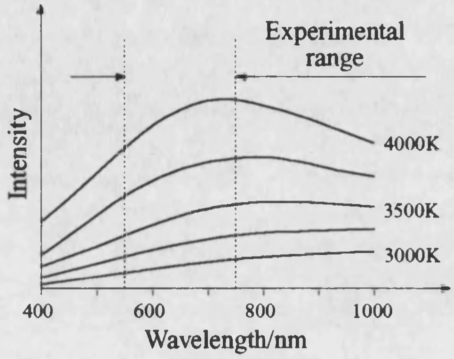

Figure 4.8. The Planck distribution at different temperatures indicating the experimental wavelength range.

A comparison of the practical performance of the Wien and Planck methods is made in section 5.4.2.

CHAPTER 5

5. EXPERIMENTAL SYSTEM PERFORMANCE

The work contained within this thesis was concerned primarily with establishing (and extending) the experimental capabilities of the apparatus described, the validity of the analysis programs, and the suitability of different test materials. An evaluation and comparison of the different materials studied is described in chapter 6. This chapter aims to quantify the experimental performance of the system as follows:

- Laser characterisation data is presented. Calculated values for the beam waist and its position are discussed. Laser stability and observed output power characteristics are also examined.

- The data acquisition process is analysed, and the preferred attributes of a data set defined by a consideration of the optimum experimental parameters. The unsatisfactory operation of some of the experimental elements is described, and their influence on collected data discussed.

- The dependence of the wavelength and sensitivity calibrations on their input data is investigated.
- A comparison, and investigation into the practical limitations, of the temperature calculation programs is described. The influence of observed test sample behaviour on the use of temperature profiles to determine thermal conductivity, thermal diffusivity, and melting temperature is discussed.

5.1. Nd:YAG LASER CHARACTERISATION

The Optilas 2180 BeamScan beam profiler described in section 3.1.2 was used to measure the variation in laser beam width along the beam axis, the shape of the beam perpendicular to its axis and to monitor the stability of the laser output. The laser output power characteristics were also investigated. Results are presented in the following sections. Note that all errors in this section are quoted to the 95% confidence limit.

5.1.1. VARIATION IN BEAM WIDTH ALONG LASER AXIS

The beam width was measured as a function of distance along the beam axis, on either side of the beam waist corresponding to the test sample location, for five nominal laser flash lamp currents: 25A, 24A, 23A, 22A, 21A; this gives ten data sets in all. The DC voltage output from the laser stabiliser (section 3.1.1) was recorded in each case to allow the beam power versus beam waist relationship to be determined more accurately. Results are presented in figure 5.1.

A linear regression technique was used to find the gradient (m) and y-axis intercept (c) of each of these lines. The full angle beam divergence, the beam waist and its position, and the depth of focus of the laser were determined from these data.

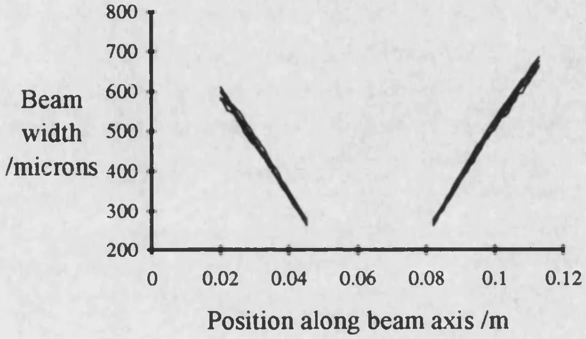

(a)

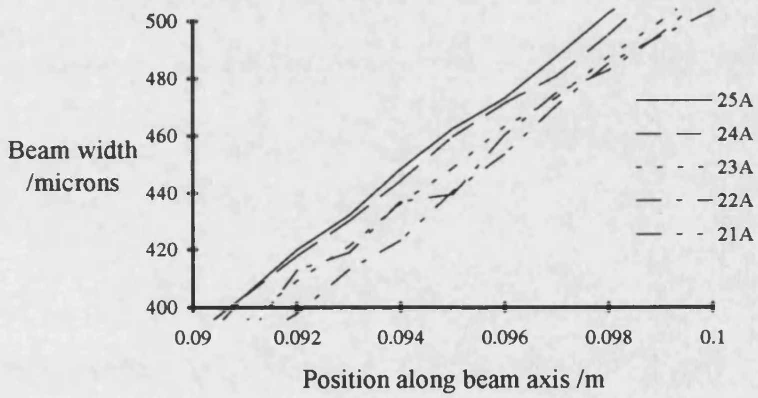

(b)

Figure 5.1. Beam width as a function of distance along the laser beam axis: (a) showing all data, (b) using an expanded scale for clarity.

FULL ANGLE BEAM DIVERGENCE

The full angle beam divergence (θ) may be found from the gradients of the lines shown in figure 5.1 according to,

$$\theta = 2\tan^{-1}m. \tag{5.1}$$

Full angle beam divergences calculated using equation 5.1 are presented in table 5.1. Note that two such calculations were made for each laser power: one for the beam converging to the waist, one for the beam diverging from the waist. Both values were determined for each flash lamp current to allow the verification of experimental results.

Laser current /A	Full angle beam divergence /rads	
	Converging beam	Diverging beam
25	0.0268 (±0.0002)	0.0266 (±0.0002)
24	0.0266 (±0.0002)	0.0261 (±0.0002)
23	0.0260 (±0.0002)	0.0261 (±0.0001)
22	0.0258 (±0.0003)	0.0258 (±0.0002)
21	0.0253 (±0.0002)	0.0255 (±0.0002)

Table 5.1. Full angle beam divergence as a function of laser flash lamp current.

It is apparent from table 5.1 that the full angle beam divergence decreases with decreasing laser power. This trend may be attributed to a grading of the refractive index of the laser's YAG crystal caused by an increase in flash lamp intensity. At low powers the refractive index of the crystal is uniform and light is reflected off the cavity mirrors as shown in figure 5.2(a). The light travels along this path because the aperture also shown in figure 5.2 will filter out any light which is not travelling in a direction perpendicular to these mirrors. However, an increase in current through the flash lamp causes a grading of the refractive index of the crystal and as a result a beam entering at an angle (as shown in figure 5.2(b)) would bend as it passes through the crystal. Note that the situation portrayed in figure 5.2(a) has been idealised and that in practice the beam leaving the laser cavity will never have constant width.

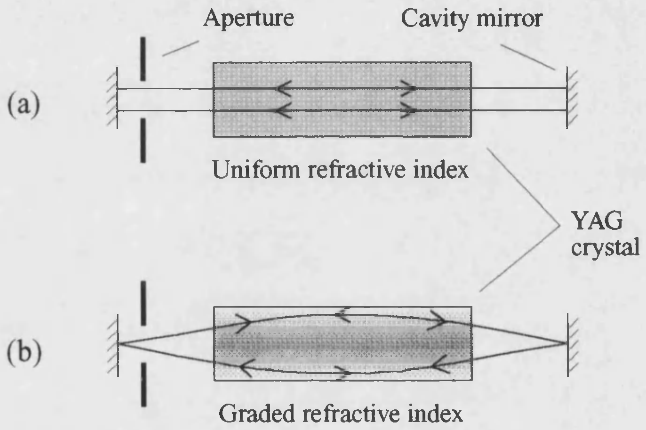

Figure 5.2. Light path through the laser's YAG crystal: (a) at low laser powers, (b) at high laser powers.

Off axis components retained within the laser beam cause it to appear to diverge on exit from the laser cavity. As the current delivered to the flash lamp increases, there is stronger convergence at a beam waist and hence the full angle beam divergence is greater. In this way, the full angle beam divergence is observed to increase with increasing laser power and vice versa.

BEAM WAIST

The beam waist was found for each of the ten data sets by substitution of the values for beam divergence given in table 5.1 and the wavelength of the Nd:YAG laser (λ=1064nm) into equation 2.7 on page 32. Calculated values are presented in table 5.2 (with their calculated errors) and plotted as a function of the scaled DC laser output voltage in figure 5.3.

Laser output		Beam waist/µm	
Current/A	Scaled voltage/mV	Converging beam	Diverging beam
25	203	25.3±0.2	25.5±0.2
24	161	25.4±0.2	26.0±0.2
23	138	26.0±0.2	26.0±0.1
22	105	26.2±0.3	26.3±0.2
21	76	26.7±0.2	26.5±0.2

Table 5.2. Beam waist as a function of laser power

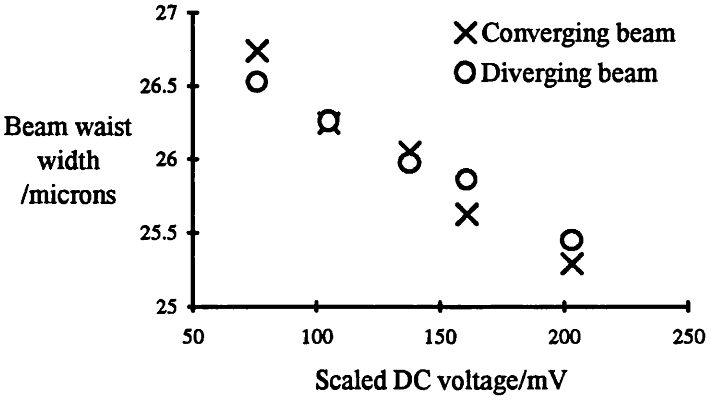

Figure 5.3. Beam waist as a function of laser power.

It is apparent from figure 5.3 that the beam waist decreases with increasing laser power as a direct consequence of the trend in beam divergence discussed in the previous section. Although the variation is comparatively small (of the order of 5%) it could prove significant in terms of subsequent thermal calculations and is discussed further in section 5.4.3.

To allow a direct calculation of beam waist from the laser output power, a linear regression of the data presented in figure 5.3 was performed. The empirical formula

$$\omega_0 = 27.3(\pm 0.2) - 10(\pm 1)\times 10^{-3}V, \qquad (5.2)$$

where V is the scaled DC voltage in mV, and ω_0 is quoted in μm, was thus determined.

Equation 5.2 was determined from data collected for laser flash lamp currents of between 21A and 25A. However, the calculated errors are small enough to allow the application of equation 5.2 at all laser powers for which the output remains stable (see section 5.1.4).

BEAM WAIST POSITION

The beam waist position (W_p) was found for each set of data by finding the x axis intercept of the calculated regression lines according to the equation,

$$W_p = -\frac{c}{m}. \qquad (5.3)$$

Results are presented in table 5.3. Note that these values represent the optical rail settings of the profiler detector head and are not the same as CAC micropositioner values quoted later.

Laser current /A	Beam waist position /cm	
	Converging beam	Diverging beam
25	6.62 (±0.09)	6.07 (±0.12)
24	6.56 (±0.07)	6.04 (±0.12)
23	6.65 (±0.08)	6.08 (±0.07)
22	6.63 (±0.11)	6.08 (±0.14)
21	6.65 (±0.09)	6.08 (±0.12)

Table 5.3. Beam waist position as a function of output laser power.

It may be observed from table 5.3 that although there is very good numerical agreement between the values in each set (those measured at the same optical rail position), the consistency between the two sets is weaker. The experimental data, from which the values presented in table 5.3 were calculated, were measured at one optical rail position for each power in turn and then for the same series of powers at the second optical rail position. This method of data collection, combined with the difficulty involved in moving the detector along the optical rail without inadvertently rotating the scan head, provides some explanation of the discrepancies demonstrated in the data shown in table 5.3. However, the calculated values of beam waist position act as a valuable guide to the required location of the test sample as the conversion of beam profiler head position along the optical rail, to the approximate CAC z-axis micropositioner setting is trivial.

DEPTH OF FOCUS

The laser beam depth of focus may be calculated by substitution of ω_0 (from table 5.2) into equation 2.10 given on page 34. Results are presented in table 5.4.

Laser current /A	Depth of focus /mm	
	Beam converging	Beam diverging
25	3.78 (±0.07)	3.82 (±0.06)
24	3.76 (±0.06)	3.98 (±0.06)
23	4.01 (±0.06)	3.98 (±0.04)
22	4.07 (±0.09)	4.07(±0.07)
21	4.22 (±0.08)	4.16 (±0.06)

Table 5.4. Depth of focus as a function of laser flash lamp current.

As before, a laser flash lamp current dependent trend is evident in the data presented in table 5.4. However, note that the smallest calculated depth of focus (3.76mm) is still sufficiently large to allow straightforward positioning of the test surface within the laser focus, and it may be concluded that the change in depth of focus with laser power has no significant experimental implications.

5.1.2. LASER BEAM SHAPE

The temperature calculation procedures (section 4.5) assume that the radiation incident on the sample surface induces an axially symmetric hot spot. Therefore, it is necessary to have an axially symmetric laser beam, which in turn implies that the laser must operate in the TEM_{00} mode thus providing a beam with a Gaussian transverse power distribution. In order to confirm that the Nd:YAG heating laser was operating in this manner, the beam profiler head was placed at a fixed position on the beam axis, and rotated through 180° with the intensity distribution of the beam being recorded at 10° intervals. The detector was then moved along the laser axis to the other side of the beam waist and the process repeated. A low laser power, corresponding to a stabilised flash lamp current of ~23A was used throughout these measurements so that damage to the detector, discussed in section 3.1.2, could be minimised.

By plotting the measured beam width as a function of profiler head angle, the line traced by the $1/e^2$ intensity contour perpendicular to the beam axis may be observed. Because the beam profiler determines the width of the beam from a measurement of intensity distribution across the entire beam, the measured data has a centre of symmetry; thus the beam width at 10° will be the same as that at 190°, and so on. The width of the beam for angles between 0° and 360°, for both optical rail positions, is plotted in figure 5.4 to show the shape of the $1/e^2$ intensity contour formed across the laser beam axis.

The theoretical width of the beam at the measured position was determined by the substitution of the appropriate experimental parameters into equation 2.2 given on page 31. The position x was calculated by subtracting the optical rail position of the detector from that corresponding to the calculated beam waist positions given in table 5.3. The calculated beam width was used to determine the 'ideal' $1/e^2$

intensity contour, which is also plotted in figure 5.4. This procedure was followed for both sets of experimental data.

It is apparent from figure 5.4 that the $1/e^2$ contour is circular in both cases, and in fact has a maximum deviation from the ideal value of only 3%. Although the shape of the beam's cross-section at the waist position cannot be found directly using this technique, it may be assumed that if the beam is circular both before and after it reaches the waist, it is also circular at the beam waist itself.

To confirm that the laser beam has a Gaussian transverse power distribution the 'goodness of fit' was calculated at each angular position using equation 3.1 given on page 57. For the data in the converging section of the beam, the goodness of fit was between 0.004 and 0.007, and for the diverging section, it was between 0.003 and 0.007. These low values indicate that the laser has a transverse power distribution which is very closely approximated by a Gaussian.

Thus, the assumption that an axially symmetric laser beam with a Gaussian transverse power distribution is incident upon the sample has been confirmed by experimental investigation.

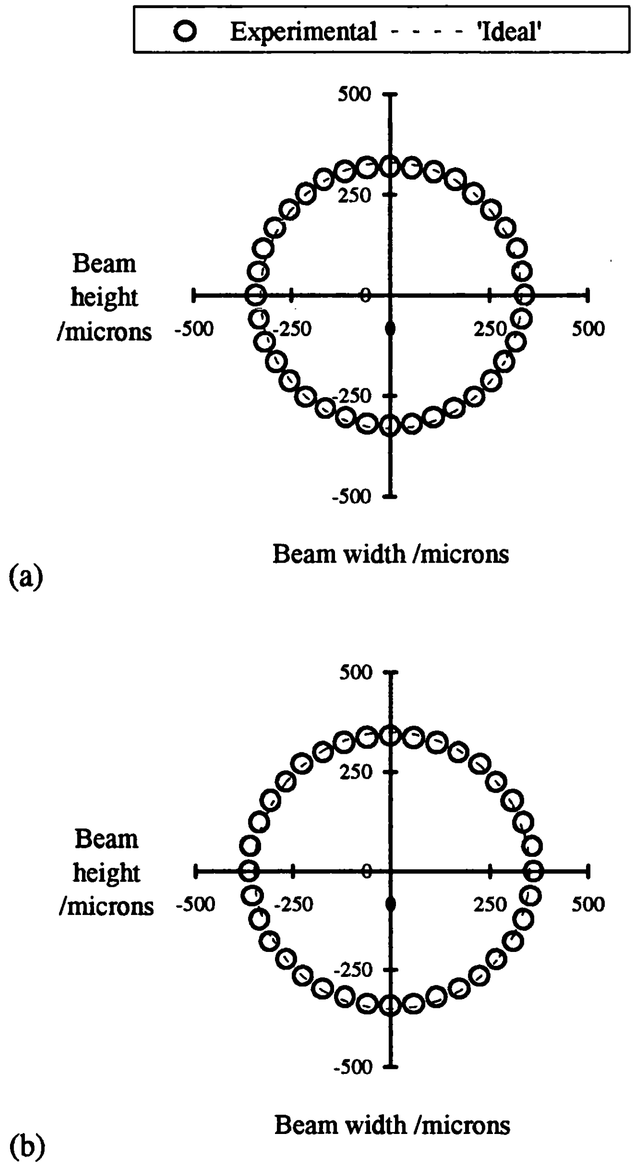

Figure 5.4. Shape of the line traced by the $1/e^2$ intensity contour perpendicular to the beam axis: (a) converging beam, (b) diverging beam.

5.1.3. LASER STABILITY

During laser operation, the stability of the laser output power is monitored by a chart recorder to measure the scaled DC voltage output by the stabiliser unit. Although correct stabilisation of the laser significantly decreases the noise observed in this DC signal (particularly at higher laser currents), it provides no information on the uniformity of the beam shape. To investigate the effect of the stabiliser on beam shape consistency, the beam profiler was used to perform synchronised measurements of beam width and peak intensity at 5s intervals for three different laser operating currents: 21A, 23A, 25A. The results are presented in figures 5.5, 5.6, and 5.7 respectively. A 5s interval was chosen to allow the manual recording of beam width and peak intensity values.

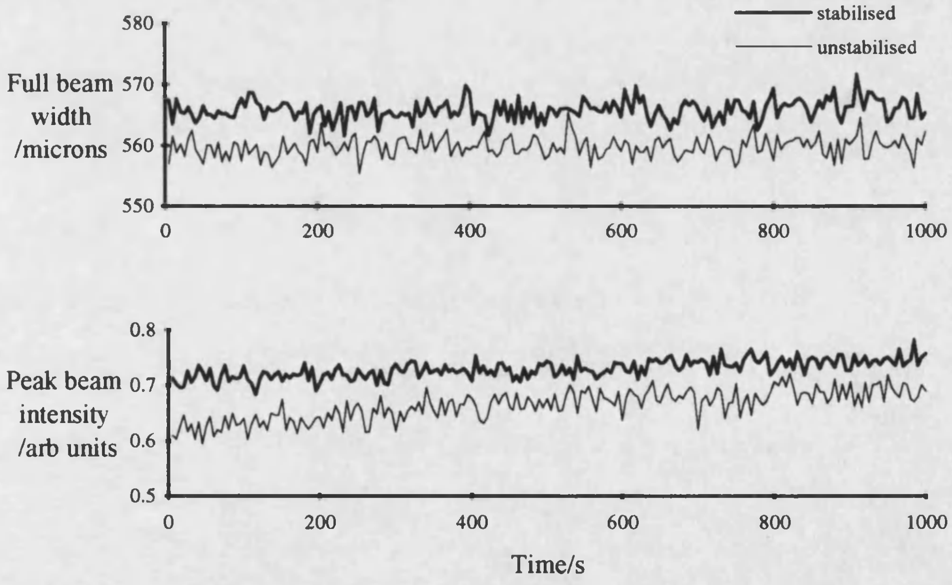

Figure 5.5. Full beam width (2ω) and normalised peak intensity as a function of time at 21A.

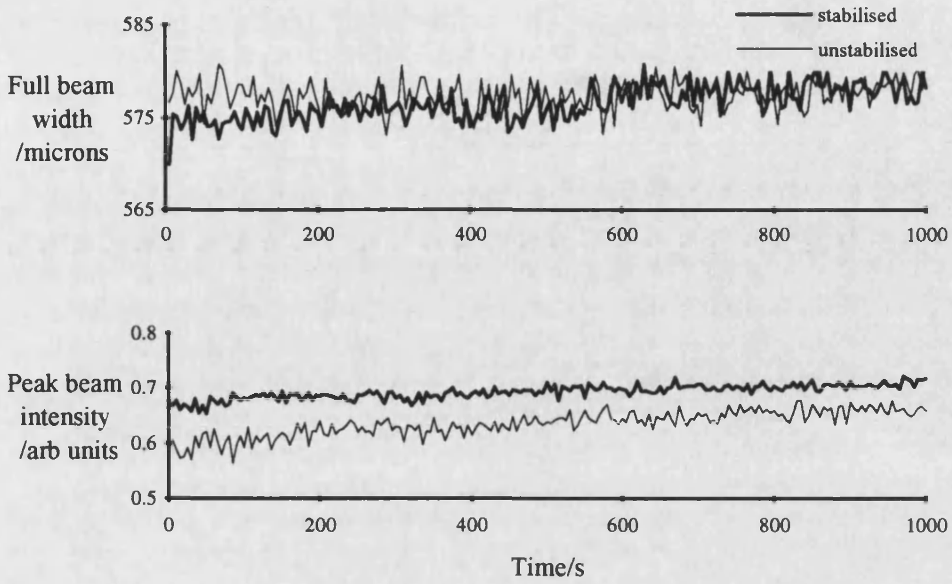

Figure 5.6. Full beam width (2ω) and normalised peak intensity as a function of time at 23A.

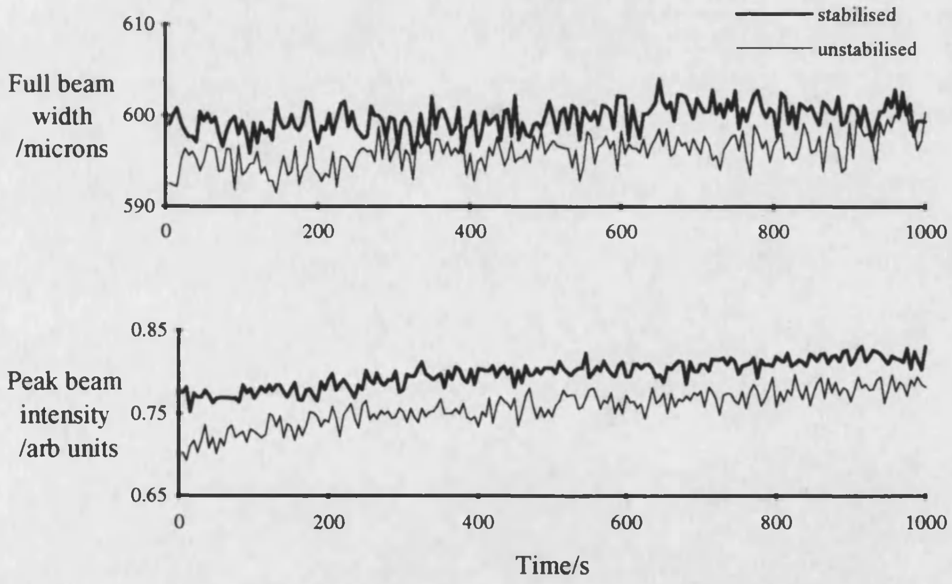

Figure 5.7. Full beam width (2ω) and normalised peak intensity as a function of time at 25A.

Before analysis of the data presented in figures 5.5, 5.6, and 5.7 can be discussed, it is important to consider several points. Firstly, the peak intensity has been scaled by a manual adjustment of the detector gain in each case, and therefore it is invalid to compare the numerical values of data collected at different laser powers. Also, the relative values of stabilised and unstabilised data result from the subjective nature of the stabilising process, and must be disregarded.

To allow a quantitative analysis of the data presented in figures 5.5, 5.6, and 5.7, the gradients of the beam width versus time graphs were determined. The standard deviation of residuals for the peak intensity data presented in figures 5.5, 5.6, and 5.7 were also found and used to determine the extent of random fluctuation present in the data once any underlying trend had been removed. Results are presented in tables 5.5 and 5.6.

These quantities were determined because it was considered that beam width drift and peak intensity fluctuations were most likely to effect the consistency of the hot spot created on the test surface by the laser. Conversely, the fluctuation in beam width was assumed to have comparatively little effect on the formation of the hot spot since light intensities collected from the edges of such an image are so small. Also, an overall drift in peak intensity was considered unlikely to have a significant influence on beam shape consistency compared to the effects caused by intensity fluctuations.

	Gradient/$\times 10^{-5}\mu ms^{-1}$		
	21A	23A	25A
Unstabilised	7.09	6.59	6.35
Stabilised	3.85	3.59	5.09

Table 5.5. Calculated gradients of the beam width as a function of time for laser flash lamp currents of 21A, 23A, and 25A.
(Original data is presented in figures 5.5, 5.6, and 5.7.)

	Standard deviation of residuals /arbitrary units		
	21A	23A	25A
Unstabilised	0.0178	0.0126	0.0110
Stabilised	0.0120	0.0075	0.0081

Table 5.6. Calculated standard deviation residuals of the peak intensity as a function of time measured for laser flash lamp currents of 21A, 23A, and 25A.
(Original data is presented in figures 5.5, 5.6, and 5.7.)

Several conclusions may be drawn from the data presented in tables 5.5 and 5.6. Firstly, although the drift in beam width with time is small in the unstabilised case, laser power stabilisation has been shown to improve beam width stability at all the laser powers considered. However, despite the fact that stability improves with increasing laser power in the unstabilised case, the trend is not repeated in the data collected with a stabilised power output. The reason for this disagreement is that laser stabilisation is a subjective process; that is, adjustments are made via the stabiliser unit until the output appears to have been optimised, and so the same degree of improvement will not always be achievable. Also, because laser stability inherently improves with increasing power (discussed further in section 5.1.4), stabilisation will have less effect at higher laser powers.

The data presented in table 5.6 follows similar trends to the data presented in table 5.5, although the magnitude of the calculated deviation is more significant in all cases. Therefore, it may be concluded that the primary contributor to the observed inconsistency in laser beam shape is the fluctuation in peak intensity with time. It would also appear that although stabilisation of the laser will reduce the drift in beam width and the fluctuation in peak intensity of the beam, the greatest stability is to be achieved by operating the laser at a moderate power, and using optical attenuators to reduce the power delivered to the sample.

EFFECT OF AMBIENT CONDITIONS

The results presented in figures 5.5, 5.6, and 5.7 were collected within an ambient temperature range of 11-13°C. Similar results were collected in the higher temperature range of 21-23°C, but no significant differences or trends were observable; it was concluded that ambient temperature, whilst maintained within the range 11-23°C, has no effect on the optical performance of the laser. However, the drift in output power, which the laser shows directly after being switched on, is more extreme under cooler ambient conditions and extra time must be allowed for the output to stabilise.

All experimental data has been collected with relative ambient humidities in the range 61% to 82%, which have been determined from measurements made with a 'wet-and-dry' thermometer. Ambient humidity has not been observed to have any noticeable effect on the calculated temperature distributions, although it was necessary to inhibit the formation of water droplets and ice crystals caused by elevated humidity on the detector pixel face, as discussed in section 3.3.1.

5.1.4. LASER OUTPUT POWER CHARACTERISTICS

OPERATING RANGE

To determine the operating power range of the laser, the scaled DC voltage output by the stabiliser unit (section 3.1.1) was plotted as a function of the laser flash lamp current. Results are presented in figure 5.8. Note that for flash lamp currents at which there was a significant range in measured laser output, the upper and lower limits are represented by separate data points joined by a dashed line.

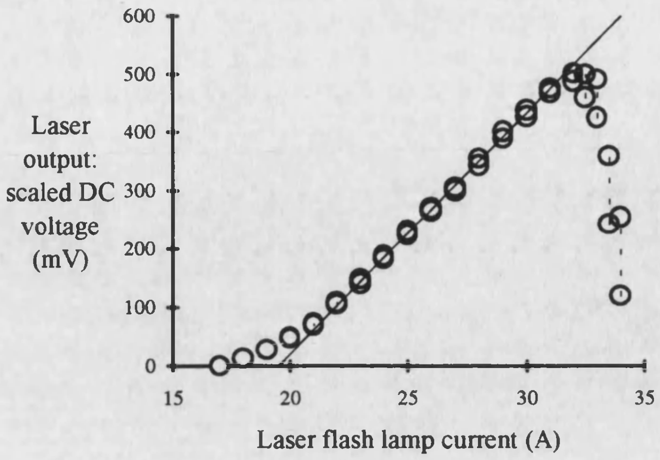

Figure 5.8. Laser power output as a function of laser flash lamp current.

It may be observed from figure 5.8 that the relationship between the flash lamp current and laser power output is linear for currents of approximately 22A to 31A. Above 31A the output power falls drastically and becomes highly unstable, and below 22A the laser ceases to have a linear output power response. Stability is at a maximum for a flash lamp current of approximately 26A.

At very low operating currents, there is insufficient population inversion to allow successful lasing, and the spontaneous emission of photons dominates. At high flash lamp currents the bending of the emitted laser beam due to the grading of the refractive index of the YAG crystal, which was discussed in section 5.1.1, becomes so extreme that only minimal light is able to pass through the aperture shown in figure 5.2, and then exit the laser cavity. In addition, the laser mode selector, which is used to select the TEM_{00} mode, ceases to operate effectively at high powers, and some multimode lasing occurs. However, because the mode selector continues to filter out all non-TEM_{00} modes, a reduction in overall laser output power occurs.

The general, and useful conclusion of these observations is that the optimum laser flash lamp current of 26A corresponds to a power at which the problems described above have little effect. Hence, operation of the Nd:YAG at this flash lamp current has been used wherever possible.

POWER DENSITY AT THE SAMPLE

The manufacturers (Quantronix) of the Nd:YAG laser quote a maximum laser output power of 18W for the laser operating in the TEM_{00} monomode. It is apparent from figure 5.8 that this corresponds to a flash lamp current of ~31A (equivalent to a scaled DC voltage of ~480mV). The gold mirror introduces minimal attenuation of the laser beam, but the dichroic mirror will reduce the laser power by approximately 20%. A further loss in laser power of 30% is caused by the aperture between the dichroic mirror and focusing lens, see section 3.2.4, giving the laser an effective power of ~10W at the sample. The beam waist (ω_0) corresponding to a laser power of 31A may be calculated from equation 5.2 on page 112, giving a value of 26.8μm. If the diameter of the hot spot is assumed to be equivalent to $4\omega_0$ (section 2.1.3), then the hot spot area is $\sim 0.90\times10^{-4}cm^{-2}$. Thus the power density delivered to the sample is $\sim 11.1\times10^{5}Wcm^{-2}$. The results of similar calculations for different flash lamp currents are presented in table 5.7.

Note that laser powers have been calculated by assuming that the potential across the flash lamp remains constant.

Nominal laser flash lamp current/A	Approximate laser power density at the sample $/\times10^5$Wcm^{-2}
31	11.1
28	10.0
25	8.8
22	7.8

Table 5.7. Laser power density at the surface of the test sample as a function of flash lamp current.

The absorbed power density of different materials at different laser powers, and how it can affect sample vaporisation and the type of laser damage it can cause, will be considered in section 6.2.

5.2. DATA ACQUISITION

The main strength of the data acquisition process employed here is its ability to measure simultaneously, and very rapidly, light intensities over a broad wavelength range. However, there are several experimental limitations both in terms of the data acquisition process itself and the generation of an acceptable image of the hot spot formed by the laser on the surface of the test sample. These two types of restriction are now considered separately.

5.2.1. THE ACQUISITION PROCESS

EXTERNAL SHUTTER OPERATION

The operation of the external shutter is relatively slow and because it functions by a sweeping action does not expose simultaneously all areas of the laser target (ie the sample). When long sample exposures are used, any effect this has on the resultant temperature profile should be minimal; however, for shorter sample exposures, the effect may be more significant.

To overcome problems associated with the external shutter, the delay between the exposure of the sample to laser heating and data acquisition may be increased. However, if the evolution of the temperature of the sample with time is under investigation, such a delay would be impractical for the successful study of transient temperatures. A faster shutter which allows the uniform, or near-uniform, exposure of the test sample to laser heating is required.

The effect of the speed of operation of the external shutter on the collection of data by the CCD is discussed further in section 5.2.2, and a recommended minimum delay between the start of laser heating and temperature measurement, determined.

HIGHLY REFLECTING TEST SURFACES

During experiments performed on polished samples, a large peak in the scaled DC laser output was observed when the external shutter was opened. The output returned to normal when the external shutter was closed. It was concluded that infra-red radiation not absorbed by the sample was being reflected back onto the photodetector housed in the output power monitor. The stabiliser circuits were detecting a peak in laser output and decreasing the power to the flash lamp accordingly.

The inclusion of a one-way infra-red filter between the dichroic mirror and external shutter would alleviate this problem by permitting the passage of infra-red light to the sample, but not back to the laser.

5.2.2. IMAGE GENERATION

To record successfully the image of a hot spot formed on the sample surface by the laser, the CCD exposure must be appropriate to the sample, the laser power, and the delay imposed by the delay unit. The following sections describe the qualities demonstrated by a 'good' data set, how to achieve one, and some basic guide-lines which may be used to determine the necessary system parameters: CCD exposure, sample surface preparation, laser power, programmable delay unit setting.

DEFINITION AND ACHIEVEMENT OF A 'GOOD' DATA SET

A 'good' data set may be defined as an image which covers a large number of horizontal CCD slices. If the image is too narrow, errors introduced to the temperature calculation by the inverse Abel transform are extreme (see section 5.4.1). Also, because the temperature calculation procedures assign an average temperature to each slice of pixels, it is wise to ensure that a pixel does not record the intensity generated by a large range of temperatures emanating from the hot spot. Sufficient light intensity incident on each of the pixels in the active array should be ensured, since low measured intensities introduce further inaccuracies to the numerical analysis.

Provided the measured CCD image does not cover more than the 384 pixels available (see section 3.3.1) it is best to make the image it measures as wide as possible. Note that in the course of this work the image entering the spectrograph has never been too wide for the CCD array to record. However, wide CCD images can cause an accumulation of errors due to the inverse Abel transform, towards the centre of a calculated temperature profile, as observed in temperature calculations made in section 5.3.2. Several investigations have been made of this phenomenon (Ladds, 1994), but as yet no solution has been found. Thus, although it is wise to create and measure broad images on the CCD, care must be taken to ensure that any distortion of the resultant temperature profile is not too severe.

Some materials, for example those with low surface reflectance and low thermal diffusivity, are able to provide broad optical images of the laser heated spot using the experimental system described. However, other materials are not so applicable for use with the specified apparatus. Surface vaporisation of metals renders them unsuitable for the creation of broad CCD images because there is minimal conduction of heat throughout their bulk. Also their relatively high thermal diffusivities mean that any surface heat generated by the laser is quickly conducted away into the sample interior. A further description of heat diffusion in different test materials is made in section 6.3.

The quality of the temperature profiles measured from the surface of laser heated metallic samples may be improved by an increase in the magnification of the optical system. By exchanging the imaging lens for one with a longer focal length, the image magnification is increased according to equation 3.2 on page 63, and the image of the hot spot covers more CCD tracks. However, since in some metallic samples (see section 7.3) the measurable light intensities have emanated from regions of severe sample damage, the validity of such a procedure requires further investigation. Attenuation of the laser beam may help to minimise surface damage, but the CCD exposure will have to be significantly increased to compensate, and for reasons given in section 4.4.2, long CCD exposures are best avoided.

An alternative method for increasing the size of the hot spot created by the laser beam on metallic surfaces would be to position the test sample slightly away from the laser's beam waist. By decreasing the power density of the laser beam incident on the sample, the probability of vaporisation could be reduced, and the chance for more heat to travel through the sample by conduction increased. However, such a procedure would require the complete rearrangement, and possible redesign, of the optical system. Under these conditions the laser would have no depth of focus at the sample position and hence the positioning of the test sample and detector, see section 4.2, would be further complicated. Also, in the light of the values given in table 2.5 on page 45, a small decrease in laser power density would make little difference to the speed with which vaporisation occurs, and hence the image recorded by the CCD.

Thus, although small improvements would be made to the performance of the experimental system, none of these would significantly enhance the image recorded by the CCD, and as a result some materials are inherently less well suited to an examination by the apparatus described than others.

SELECTION OF THE CORRECT CCD EXPOSURE

A very short CCD exposure is required for near instantaneous temperature measurements, which is imperative if the evolution of temperature profiles with time is under investigation. The recorded image should have a high intensity but without causing 'top-out' of the detector. In some cases the minimum CCD exposure (10ms in this case) may still be too long and the laser power must be reduced accordingly. If the CCD exposure is too short, the time taken for the CCD shutter to open and close becomes a significant parameter and the exposure of the CCD would be non-uniform. For example, the CCD shutter takes between 2ms and 3ms to open or close completely (Ladds, private communication), and so a set exposure of 10ms would result in some parts of the detector being exposed for ~12ms and others for ~8ms. The non-uniform illumination of the CCD results in a non-uniform image being recorded and the subsequent data analysis, particularly the data symmetrisation, will be adversely affected. The final choice of exposure time must be a compromise between these two conflicting demands.

The effect of chosen CCD exposure on the calculation of temperature distributions was investigated by using the calibrated lamp and pin hole apparatus (section 4.2) to simulate a hot spot formed on the surface of the test sample. The CCD exposure was increased in steps of 40ms until saturation of the recorded image was observed. CCD exposures of 200ms, 240ms, 280ms and 320ms were used. To demonstrate the extent of top-out in each case the intensity/wavelength distribution measured across the central CCD track for each exposure is given in figure 5.9. Temperature profiles were calculated for each data set and are shown in figure 5.10.

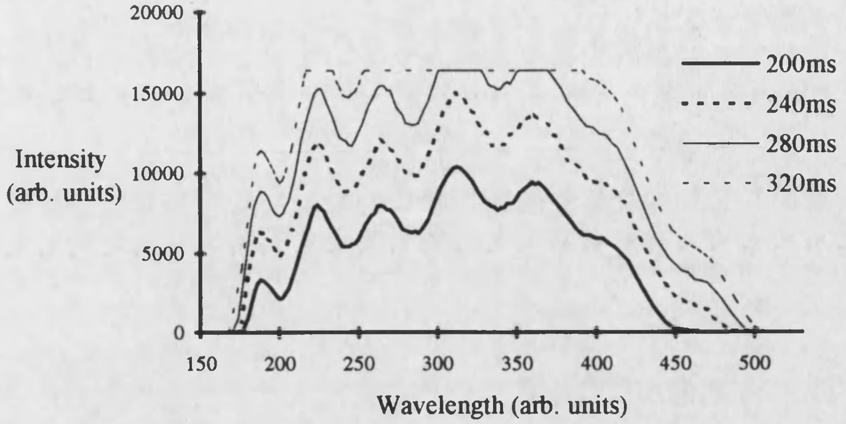

Figure 5.9. Measured spectral response of the calibrated lamp along a single CCD track for different detector exposures.

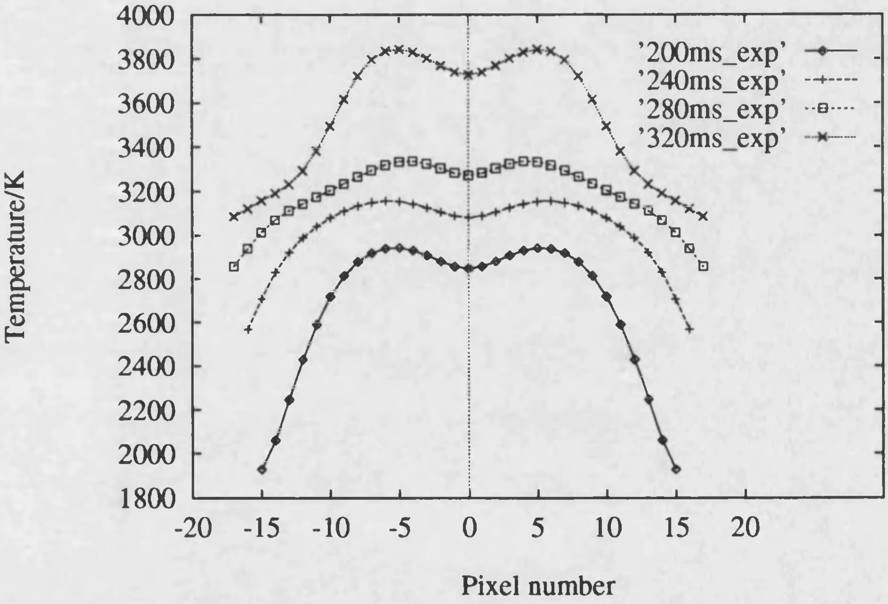

Figure 5.10. Temperature profiles calculated from CCD data collected using different exposures.

Note that the calculated temperature distributions, rather than having uniform temperature across their central region as expected, demonstrated a dip in the centre due to the accumulation of errors towards the centre of the profile caused by the inverse Abel transform. This problem cannot be avoided and is discussed further in section 5.4.1.

It is apparent from the data presented in figures 5.9 and 5.10 that a change in CCD exposure results in a shift of the calculated temperature profile. Of particular interest is that the difference in temperature between the 200ms exposure curve and the 280ms exposure curve is approximately the same as that between the 280ms and 320ms curves despite the fact that there is no top-out of the 200ms and 240ms exposure data, while there is of the intensity/wavelength spectrum collected for a 280ms CCD exposure. The displacement of the temperature curve for the 320ms CCD exposure data is more pronounced.

These observations indicate that provided the peaks of the measured spectral response can be resolved, top-out of the image recorded by the CCD does not introduce any additional error in the temperature calculation. Of more significance is the noticeable shift in temperature observed for different CCD exposures, which has significant experimental implications. These are investigated further in section 5.3.2.

SURFACE PROPERTIES OF THE TEST SAMPLE

The physical properties of a material which govern its response to laser radiation have been considered in section 2.2. By far the most significant is the reflectivity, since it determines the relative amounts of energy absorbed and reflected by the material. For uranium dioxide, reflectivity is inherently low, energy absorption high, and a comparatively low CCD exposure needed, whereas in most metals the reverse is true. Thus for metals it is preferable to minimise reflectance so that CCD exposure times may be reduced. The use of different surface preparations to change the optical properties of the test material is discussed in section 6.1.1.

CHOICE OF LASER POWER

The optimum laser flash lamp current, determined from stability requirements, is 26A (section 5.1.4). However, operation of the laser at this current is not always practical. The effective laser power can be reduced by the inclusion of optical attenuators, as described in section 3.2.2, but higher powers can only be achieved by increasing the flash lamp current, thus incurring reduced stability. For some materials a hot spot image may only be recorded for flash lamp currents within the higher, less stable range.

It is important to recognise the concept of high and low laser powers with regard to different samples. For example, for a given laser power, uranium dioxide may demonstrate surface damage typical of a high laser power whereas a metal such as iron will suffer damage typical of a low laser power. Therefore, it is invalid to make a direct comparison of different samples for a given laser output unless their optical properties are identical. This is discussed further in section 6.2.

SETTING THE PROGRAMMABLE TIME DELAY UNIT

The preferred delay between the commencement of laser heating and data acquisition should be solely dependent upon the type of study being undertaken: either a time dependent or a time independent study. In the first case, different delays combined with short CCD exposures may be used to build up a series of 'snap-shots' of the temperature distribution created on the surface of the test sample, as a function of time. In the second case, the test sample is left to assume thermal equilibrium before its temperature is measured.

However, experimental studies have shown that for reasons given earlier in this section, the delay unit should always be set above a minimum threshold. Figure 5.11 shows temperature profiles measured on uranium dioxide using delays of 0.8s and 1s. Temperature profiles for a delay of 0.5s are shown in figure 5.12. A laser flash lamp current of 22A, with all three neutral density filters in place, was used throughout.

It is apparent from the data presented in these figures that for delays of 0.8s and longer there appears to be reasonable agreement between temperature profiles measured under the same experimental conditions. However, for shorter delays (0.5s), the temperature calculation becomes significantly unstable. Note that asymmetry of the hot spot, caused by the inadequate operation of the external shutter, introduces an instability into the symmetrisation and inverse Abel transformation of the experimental data, which results in the calculation of a corrupted temperature profile. Thus, it is provident to impose a minimum delay between the exposure of the sample to laser heating and the commencement of data acquisition by the CCD; in this case it should be set at 0.8s.

Although this recommendation is only valid for the chosen sample under the specified experimental conditions, it acts as a guide to the treatment of other materials. It is certainly clear that a minimum delay must be allowed between heating of the sample and measurement of its temperature, although the exact value of this figure remains unknown for specific materials. Throughout the course of this work, 1 second was used as a default value, although it is important to note that the OMA2000 operating system also has an inherent delay which acts in addition to that set by the programmable delay unit.

Further experimental implications of the ineffective operation of the external laser shutter are discussed in section 6.3.2.

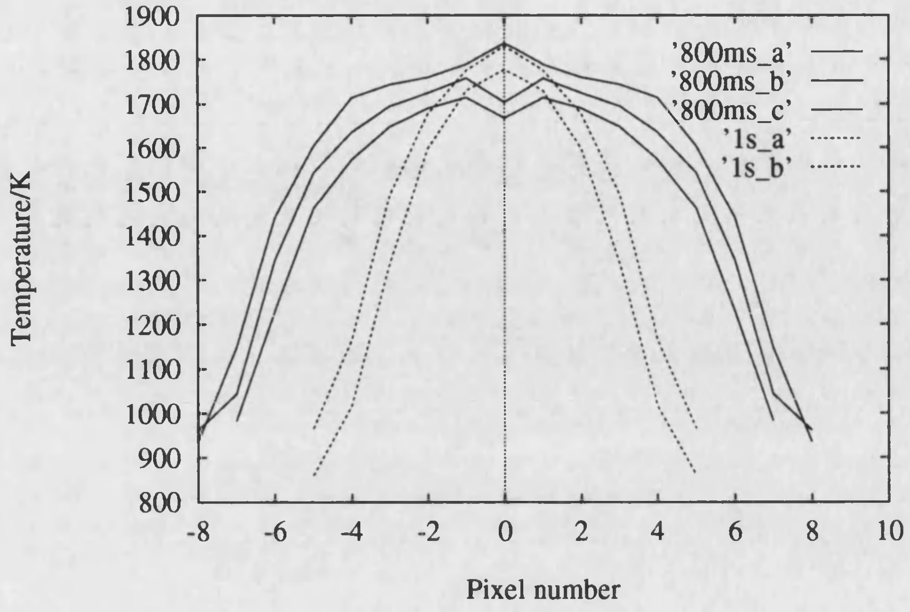

Figure 5.11. Temperature profiles measured using a delay of 1s and 0.8s.

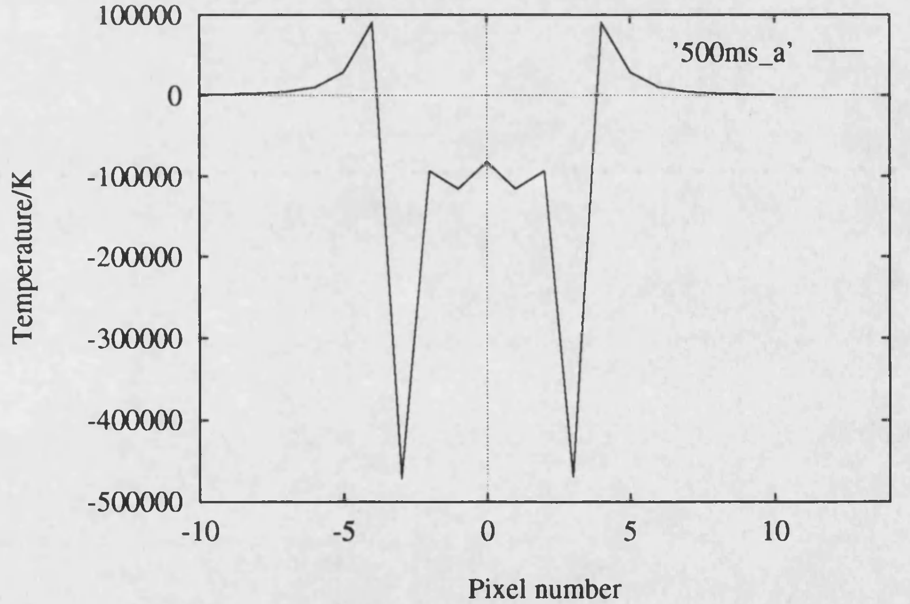

Figure 5.12. Temperature profiles measured using a delay of 0.5s.

5.3. CALIBRATION PROCEDURES

5.3.1. WAVELENGTH CALIBRATION

Vertical tracks of CCD pixels are calibrated for wavelength by identification of the pixel number corresponding to the wavelength emitted by a HeNe laser (p_{HeNe}), see section 4.3.2. However, the peak in the measured intensity distribution often covers a strip on the CCD wider than one pixel and the allocation of a single pixel number to p_{HeNe} becomes a subjective process; inaccuracies may result. To investigate the practical implications of a poor estimate of p_{HeNe}, wavelength calibrations using a range of values for p_{HeNe} were performed, and then used to make calculations of temperature distributions from the same raw data using both the Wien and Planck fitting methods. Results for each of the temperature fitting techniques are now considered separately.

THE WIEN METHOD

Figure 5.13 shows temperature profiles calculated from CCD data collected from the heated surface of a UO_2 sample, using three different values of p_{HeNe}: 327, 319, 311. Note that 319 was the value of p_{HeNe} measured with the HeNe laser and the pinhole arrangement described in section 4.3.2, and that in practice the introduction of an uncertainty in p_{HeNe} as large as ±8, by a poor judgement of the position of the HeNe intensity peak on the detector, would be unlikely.

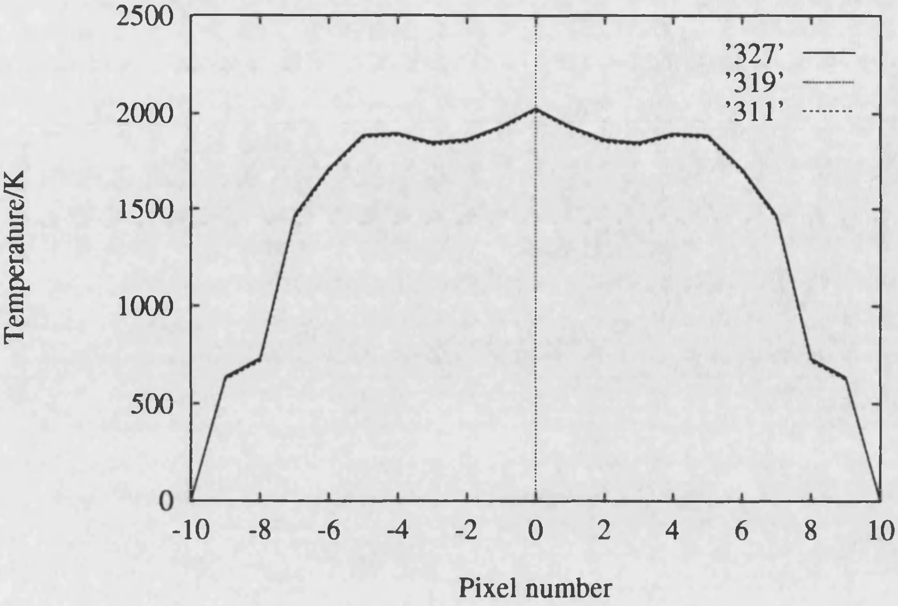

(a)

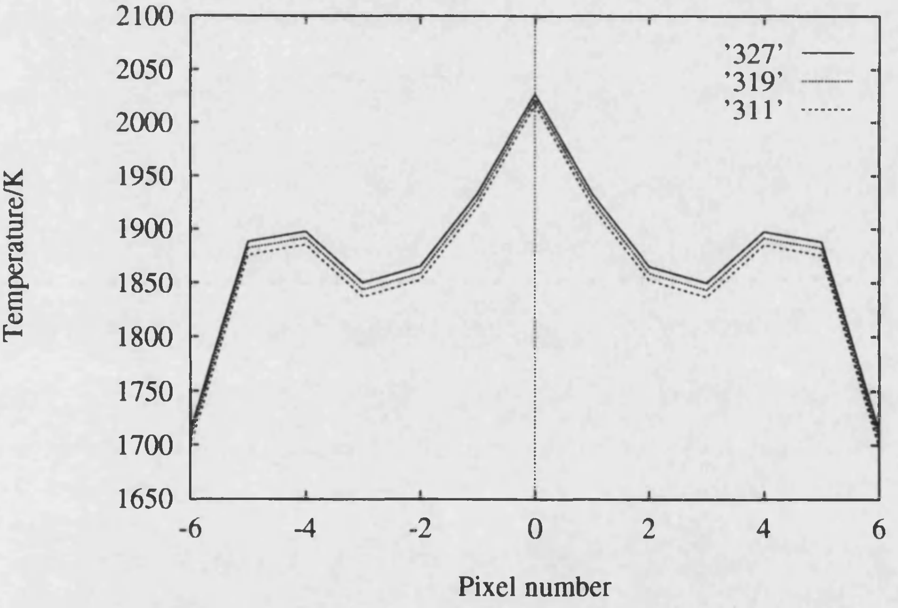

(b)

Figure 5.13 . Effect of a poor estimate of p_{HeNe} on the subsequent calculation of temperature by the Wien technique: (a) full profile, (b) expanded scale.

It is apparent from the data presented in figure 5.13 that an extremely poor estimate of p_{HeNe} introduces an error in temperature of the order of 5K. Hence it was concluded that a poor judgement of the position of the intensity peak created on the CCD by the HeNe laser has very little effect on temperatures calculated by the Wien method.

The extreme tolerance of the Wien technique to an erroneous wavelength calibration may be explained by an examination of the expressions for the modified x and y co-ordinates used to calculate temperature. These were quoted in section 4.5.5 as

$$x = \frac{hc}{k_B \lambda}, \tag{5.4}$$

and

$$y = \ln \frac{I}{2\pi hc^2 \lambda^{-5}}. \tag{5.5}$$

Taking the partial derivative of equation 5.4 with respect to λ gives

$$\frac{\partial x}{\partial \lambda} = \frac{-hc}{k_B} \frac{1}{\lambda^2}. \tag{5.6}$$

Substitution for x from equation 5.4 into equation 5.6 gives the expression

$$\frac{\Delta x}{x} = \frac{\Delta \lambda}{\lambda}, \tag{5.7}$$

for the fractional error ($\Delta x/x$) introduced to x by a given uncertainty ($\Delta\lambda$) in the value of λ. Substitution of the wavelength spread across one CCD pixel (0.5797nm) for $\Delta\lambda$, and the wavelength of the HeNe laser (632nm) for λ in equation 5.7 gives

$$\frac{\Delta x}{x} \sim 10^{-3}. \qquad (5.8)$$

Thus an uncertainty of ±1 in the measurement of p_{HeNe} results in an error of 0.1% in the modified x co-ordinate given by equation 5.4.

Now consider the modified y co-ordinate given by equation 5.5. The partial derivative of this expression with respect to λ is

$$\frac{\partial y}{\partial \lambda} = \frac{5}{\lambda}, \qquad (5.9)$$

and so the error (Δy) in y caused by an uncertainty in λ may be written,

$$\Delta y = \frac{5}{\lambda}\Delta\lambda. \qquad (5.10)$$

Substitution of 632nm and 0.5797nm for λ and $\Delta\lambda$ respectively, into equation 5.10 gives an uncertainty in y (Δy) of $\sim 5\times10^{-3}$. The substitution of a typical value of 10,000 for the intensity (I) (see section 3.3.1) in equation 5.5 gives a characteristic value of ~30 for y. Thus, the error introduced to the modified y co-ordinate (equation 5.5) by an uncertainty of ±1 in p_{HeNe} is ~0.02%.

Hence, by introducing a very small uncertainty into the modified x and y co-ordinates (equations 5.4 and 5.5 respectively), a poor estimate of p_{HeNe} has been shown to have very little effect on temperatures calculated by the Wien technique.

THE PLANCK METHOD

Although temperature calculations made by the Wien method are insensitive to the accuracy of the wavelength calibration, those made using the Planck law are quite different. The Planck method fits experimental data directly to a theoretical distribution of intensity versus wavelength, and so an incorrect calibration of the wavelength scale will have significant effects.

Figure 5.14 shows the temperatures calculated from three wavelength slices (see section 4.4.3), plotted as a function of the different pixel numbers assigned to the HeNe intensity peak (p_{HeNe}). Slice 0 corresponds to the temperature at the centre of the distribution, slice 1 the next calculated temperature, and so on. Note that the test sample/experimental system configuration were unable to generate temperatures sufficiently high for the Planck fitting method to work effectively, although calculations suitable for a relative comparison have been made. Temperatures are not shown for all values of p_{HeNe} due to non-convergence of the fitting method as described in section 5.4.2.

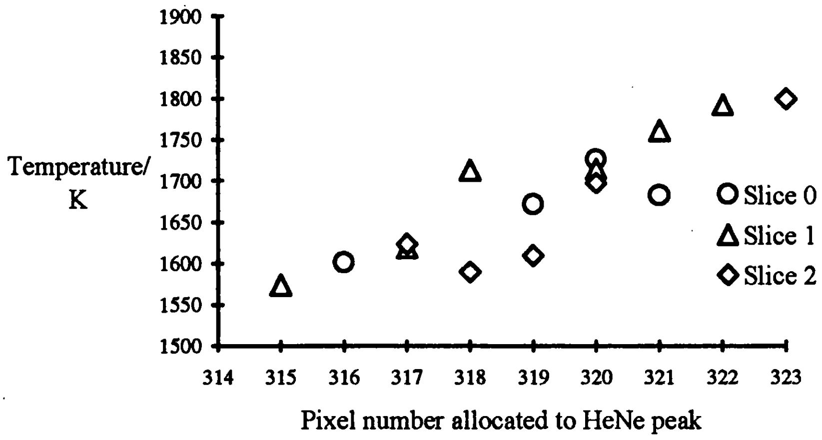

Figure 5.14. Temperatures calculated from the same raw data at three different pixel positions using different values for the pixel number allocated to the HeNe intensity peak (p_{HeNe}).

The data presented in figure 5.14 demonstrates an upwards trend in temperature with p_{HeNe}, which may be explained by reference to the principle upon which the Planck fitting routine is based. The temperature dependence of the Planck intensity/wavelength relationship has been shown in figure 2.7 on page 50, from which it is evident that as temperature increases, the peak of the distribution moves towards the low wavelength end of the spectrum. By assigning too high a pixel number to p_{HeNe} the wavelength scale has been artificially shifted in the low wavelength direction, and calculated temperatures are too high. If p_{HeNe} is set too low, the peak of the Planck distribution is moved towards the high wavelength end of the spectrum and the calculated temperatures are too low. In the worst case, the distribution may be moved so far to the right (as viewed in figure 2.7) that the peak no longer lies within the experimental wavelength range and correct temperature fitting becomes impracticable.

Another observation, which may be deduced from figure 5.14, is that temperatures calculated for the same wavelength slice with values of p_{HeNe} only one apart, may be as different as 100K. However, the temperatures plotted in figure 5.14 are not within the ideal range of the Planck method, and therefore it is unreasonable to assume that such a discrepancy in p_{HeNe} would cause an error as large as ±50K at all calculated temperatures.

Although it is impracticable, at this time, to quantify the inaccuracies introduced into the calculated temperature profiles by the wavelength calibration, the strong wavelength dependence of the Planck fitting routine will always render it susceptible to errors caused by an erroneous measurement of p_{HeNe}.

5.3.2. OPTICAL SENSITIVITY CORRECTION

The use of a spectral sensitivity correction to take into account the spectral response of the dichroic mirror was discussed in section 3.2.4. Temperature calculations described by Ladds (1994) and Tytler (1995) used only a single calibrated light measurement, with a standard coefficient cut-off (section 4.3.3) of 2, to perform this conversion. During repeated measurements of the spectral response of the calibrated light source under identical experimental conditions made as part of this study, it was observed that the wavelength positions of the maxima and minima remained constant whilst their intensities did not.

An investigation is now made into the preferential value of correction coefficient cut-off, and the experimental implications of a poor choice. The inability of the experimental system to detect a constant spectral response from the calibrated lamp is studied and an exploration of the experimental consequences of the CCD exposure used to obtain this data described.

SPECTRAL CORRECTION COEFFICIENT CUT-OFF

Resultant temperature distributions can vary significantly depending on which calibration set is used for the spectral correction of the raw temperature data. Figure 5.15 shows eight temperature profiles calculated from a single hot spot image generated on uranium dioxide, by the application of eight different spectral sensitivity calibration sets; a correction coefficient cut-off of 5 was used. Note that all spectral sensitivity data was collected under identical experimental conditions and that the Wien method was used for all temperature calculations.

It is apparent from figure 5.15 that although there is good agreement between six of the eight profiles, the other two differ greatly. The effect of reducing the cut-off further (to 2) is shown in figure 5.16. The spread in calculated temperature profiles is extreme; this is due to insufficient data being drawn from the spectral responses of the calibrated light source.

An iterative process to determine the coefficient cut-off which would provide the greatest agreement between calculated temperature profiles was performed; an optimum value of 4.2 was found. The resultant temperature profiles are shown in figure 5.17. Now there is much better agreement between the curves, although there remains a scatter of ~100K (equivalent to ~5% of the peak temperature).

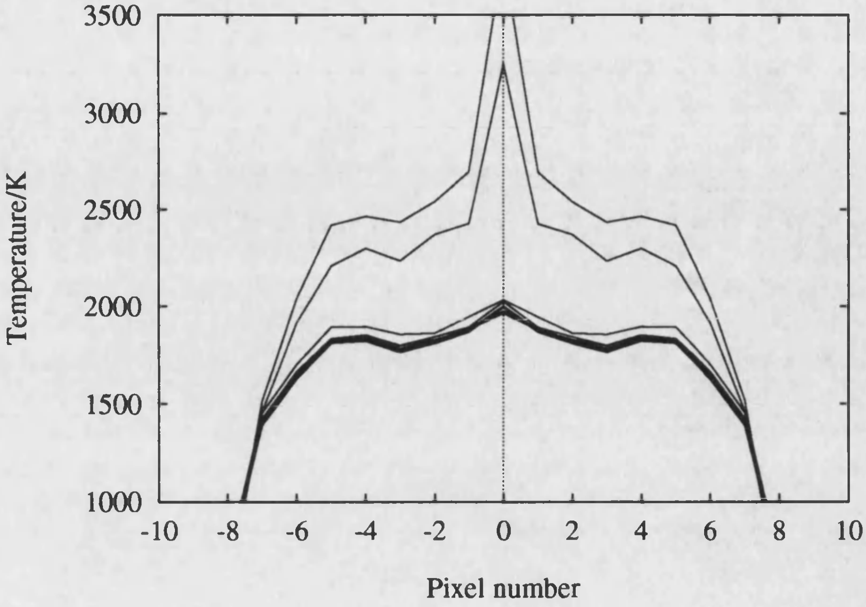

Figure 5.15. Temperature distributions calculated from the same raw data, using eight different white light calibration sets (coefficient cut-off is 5).

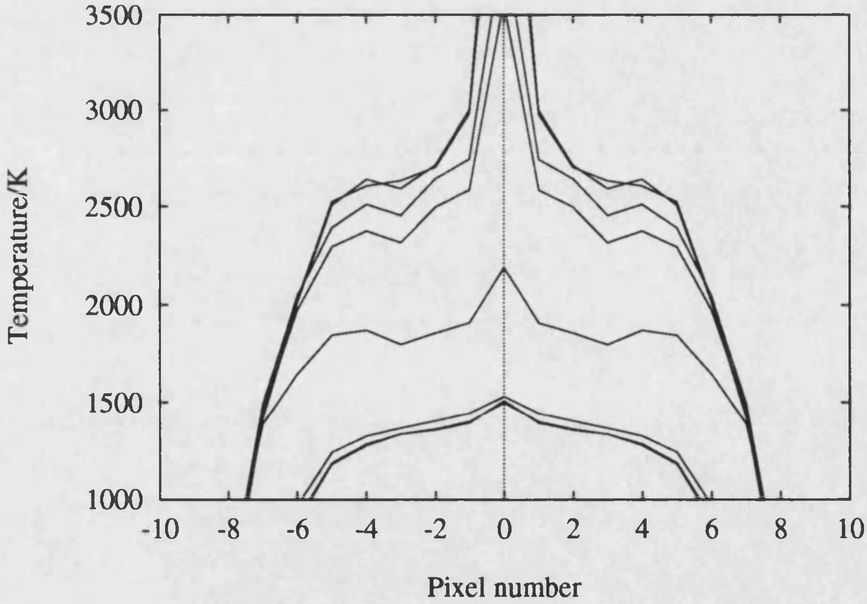

Figure 5.16. Effect of reducing calibration coefficient cut-off to 2.

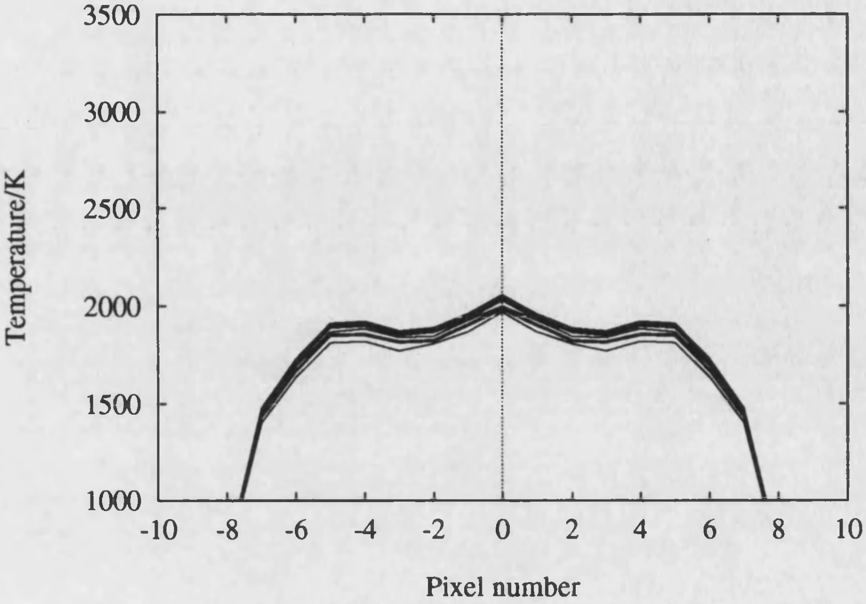

Figure 5.17. Temperatures calculated with the optimum coefficient cut-off value of 4.2.

The spectral correction coefficients used to produce the temperature profiles shown in figures 5.15, 5.16, and 5.17 are shown in figure 5.18. A cut-off in correction coefficient of 5 would include all of the coefficients, whereas a value of 2 would exclude a large proportion. The optimum value of 4.2 includes nearly all coefficients, except those at the tops of the large peaks at either wavelength extreme. It may be observed that it is at these extremities that the greatest disagreement between the spectra occurs. Thus it is provident to include very nearly all of the spectral coefficients except for those approaching the peak values if good agreement of calculated temperature profiles is to be achieved.

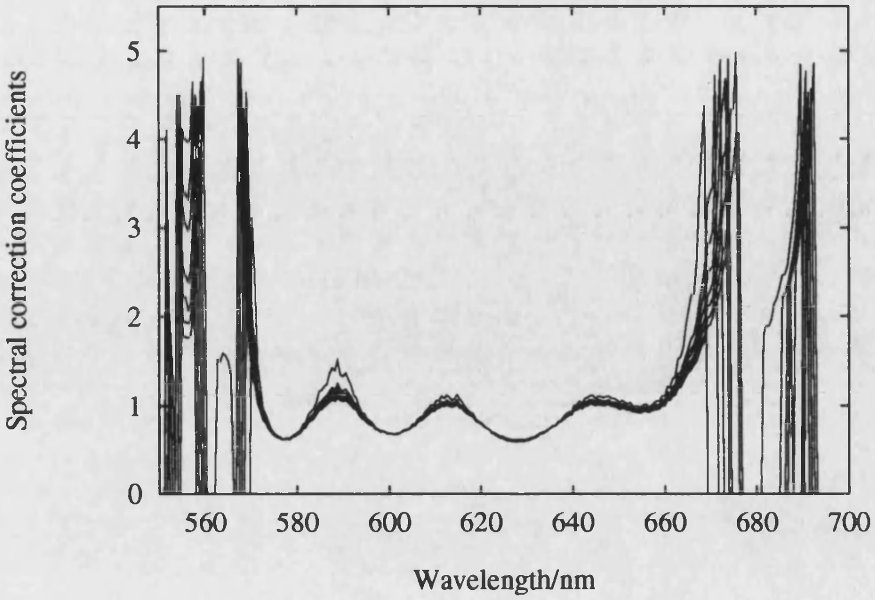

Figure 5.18. Spectral correction factors used to generate the temperature profiles shown in figures 5.15, 5.16, and 5.17.

The correct choice of coefficient cut-off will depend upon the exposure of the CCD. A long CCD exposure results in a high intensity distribution for $M(\lambda_i)$ (see section 4.3.3), correspondingly low values for $C(\lambda_i)$ (according to equation 4.2), and a relatively low cut-off value will be required. Conversely, if the CCD exposure is shortened, the cut-off value must be increased. It can be concluded that the chosen cut-off value must be altered to suit the measured white light spectrum used in the sensitivity correction procedure.

NON-UNIFORM SPECTRAL RESPONSE OF THE CALIBRATED LAMP

To investigate the inability of the experimental system to generate and measure reliably the intensity/wavelength spectrum of the calibrated lamp, the following study was performed. With a CCD exposure of 220ms, the spectral response of the lamp was measured 30 times. The central wavelength slice of each image was selected, and the intensity of each of the peaks along that track recorded.

The main objective here was to determine the nature of the instability in the sensitivity correction coefficient measuring process, which it was proposed would take one of two forms. The first was that within each wavelength slice the heights of the peaks in the distribution were changing relative to each other between measurements, due to a small fluctuation in the temperature of the calibrated lamp. The second was that the intensity of the whole wavelength slice was changing by a scaling factor between measurements, implying a non-uniformity in the sensitivity of the CCD/spectrograph apparatus.

Consider the intensity distribution across a wavelength slice shown in figure 5.19. To discover which of the above situations was more probable, the mean and standard deviation of the intensity of the third peak ($\overline{P}_3$ and σ_3 respectively) were calculated from each wavelength slice. For each spectral image the intensity of this third peak was normalised relative to the fourth peak (the highest) and the mean and standard deviation ($\overline{(P_3/P_4)}$ and $\sigma_{3/4}$ respectively) re-calculated.

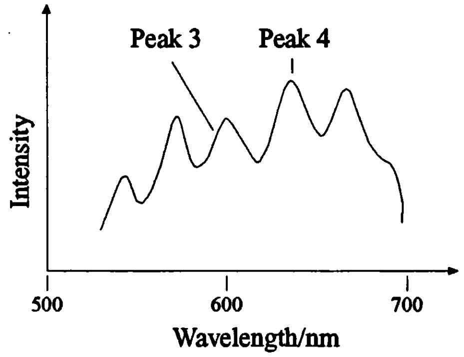

Figure 5.19. Intensity/wavelength distribution of the calibrated light source along a single CCD track showing numbered peaks.

To allow a direct comparison of the normalised and non-normalised data, the standard deviation was expressed as ratio of the mean value, giving

$$\sigma_3/\overline{P_3} = 0.0028, \qquad (5.11)$$

and,

$$\frac{\sigma_{3/4}}{\overline{(P_3/P_4)}} = 0.0040\,. \qquad (5.12)$$

Although the standard deviation for the normalised is larger than that for the non-normalised data, both values are so small that the result was considered inconclusive; the instability of the measured spectral response was not attributed solely to either a random fluctuation or a general offset of the intensity distribution. Extensive experimental and statistical work would be needed to determine the cause of the observed variation in the measured intensity/wavelength relationship of the calibrated light source.

EFFECT OF CCD EXPOSURE

In the course of a study to determine the effect of 'top-out' of recorded CCD images on the subsequent calculation of temperature, the presence of a relationship between the CCD exposure used and the resultant temperature profile was highlighted (see section 5.2.2). To investigate this phenomenon further, a set of sensitivity correction coefficients were calculated from an intensity/wavelength spectra collected from the calibrated lamp, using a CCD exposure of 240ms. Further spectra were collected for different exposures and used to determine temperature profiles from the calculated correction coefficients. Note that none of the recorded images indicated any sign of 'top-out' and that measured intensities were very similar. Results are presented in figure 5.20.

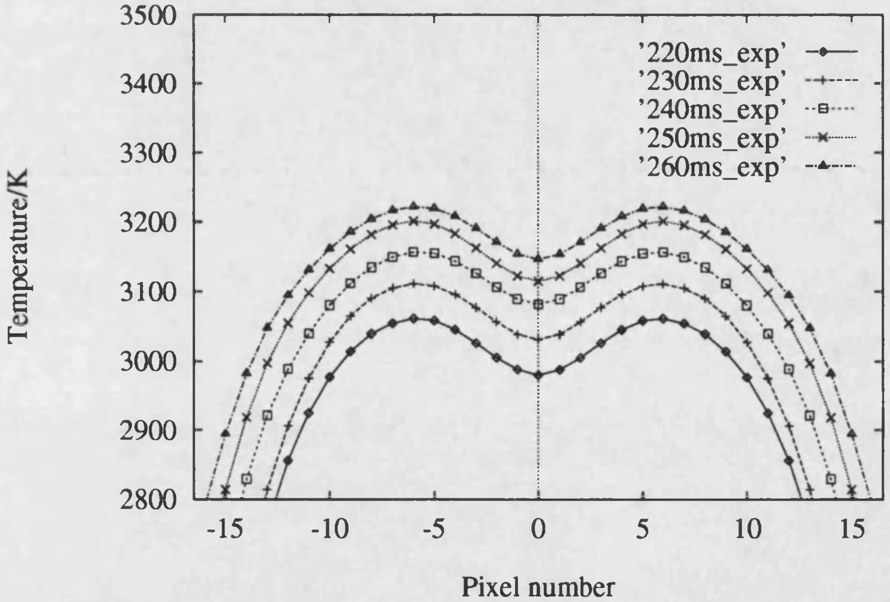

Figure 5.20. Temperature profiles calculated from simulated hot spots using different CCD exposures.

It is apparent from the data presented in figure 5.20 that the smallest possible increment in CCD exposure (10ms) has a marked effect on the calculated temperature. In this case an increase in exposure time of 10ms corresponds to a shift in temperature profile of approximately 30K. Data collected using a CCD exposure in excess of that used for the measurement of correction coefficients results in an increase in calculated temperature, and vice versa. This may be explained as follows:

A long CCD exposure will result in the collection of a broader image of the hot spot by the detector and as a consequence, light intensities from the extremities of the wavelength axis will be recorded. Now consider the wavelength/intensity distribution shown in figure 5.19 on page 151. At long wavelengths the distribution falls away rapidly, whereas at short wavelengths the reduction in intensity is more gradual. Therefore, as the wavelength range over which data is recorded increases, the additional data collected at long wavelengths will be less than the extra information measured at short wavelengths. As a consequence, the temperature fitting routines assume that the presence of extra data at low wavelengths implies an increase in temperature.

A solution to this problem could be to impose maximum and minimum wavelength limits so that all CCD images would cover the same number of wavelength slices. However, selection of these limits would not be straightforward. If they were set too close together, the analytical benefits gained from recording a broad image (see section 4.4.2) would be lost, and if they were too far apart, there would be a danger of recording the edge of CCD images, as is currently the case. By contrast, if the performance of the experimental system were improved, thus increasing the repeatability of experimental measurements, the size of CCD images could be predicted more easily, and the solution outlined above could be implemented.

5.4. TEMPERATURE CALCULATIONS

5.4.1. ANALYTICAL LIMITATIONS

THE INVERSE ABEL TRANSFORM

The inverse Abel transform assumes that the edge slice of the hot spot has a uniform temperature (see section 4.5.4) and as a consequence, the extremities of a calculated temperature profile are susceptible to large errors. There is also an increased uncertainty in the temperature of the central position because as the inverse Abel transform works in from the edge of the image to the centre, errors are accumulated. The temperature profile, shown in figure 5.21, demonstrates these features in terms of the large error bars associated with the two edge pixels and the increase in size of the error bars towards the centre of the image. Note that the errors shown are only those resulting from mathematical processing and do not act as an indication of experimental error.

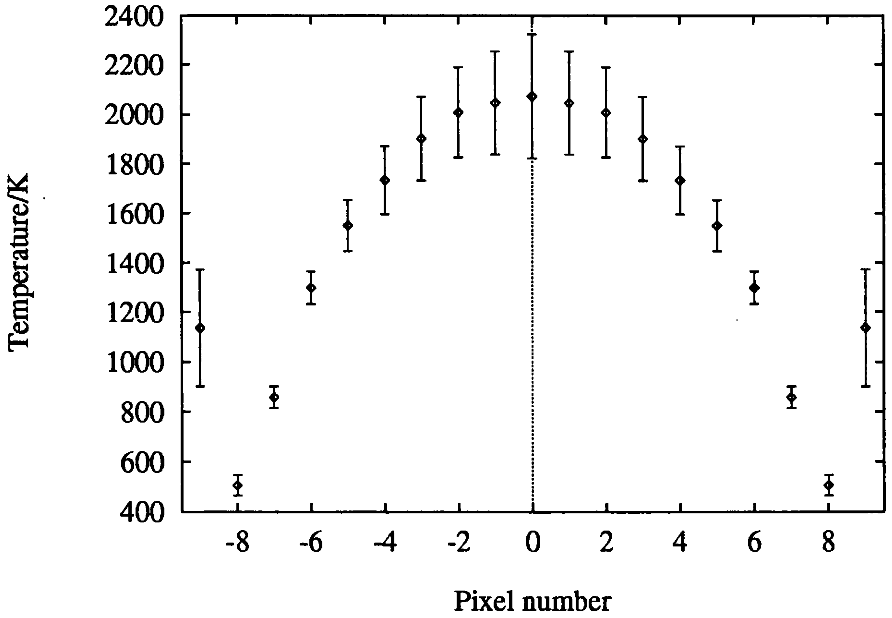

Figure 5.21. Temperature profile formed on a uranium dioxide sample to demonstrate errors introduced to temperature calculations by the inverse Abel transform.

LOW MEASURED LIGHT INTENSITY

A typical OMA2000 data set has been shown in figure 4.5 on page 95. The low values of intensity at the edges of this distribution make the analysis of the data within these regions more susceptible to inaccuracies, resulting in further uncertainty in the temperatures measured at the edge of the hot spot. Hence, data at the edges of calculated temperature profiles is always ignored in any further analysis.

5.4.2. COMPARISON OF TEMPERATURE CALCULATION TECHNIQUES

The most appropriate temperature ranges for each of the two temperature calculation techniques were described in section 4.5.5. It was concluded that although the Wien method was most suited to lower temperatures, the Planck method offered greater accuracy at temperatures above 4000K. However, temperatures this high were not achieved due to the experimental limitations imposed by the external shutter, see section 6.3.2.

In the course of the work described in this thesis a comparison was made of the Wien and Planck methods, and a number of conclusions drawn. Figure 5.22 shows the temperature across a simulated hot spot (created by the calibrated lamp and pin hole apparatus, see section 4.2) as calculated by both the Wien and Planck methods. Note that the central point of the temperature distribution calculated by either method is always susceptible to higher inaccuracies due to the use of the inverse Abel transform (see section 5.4.1).

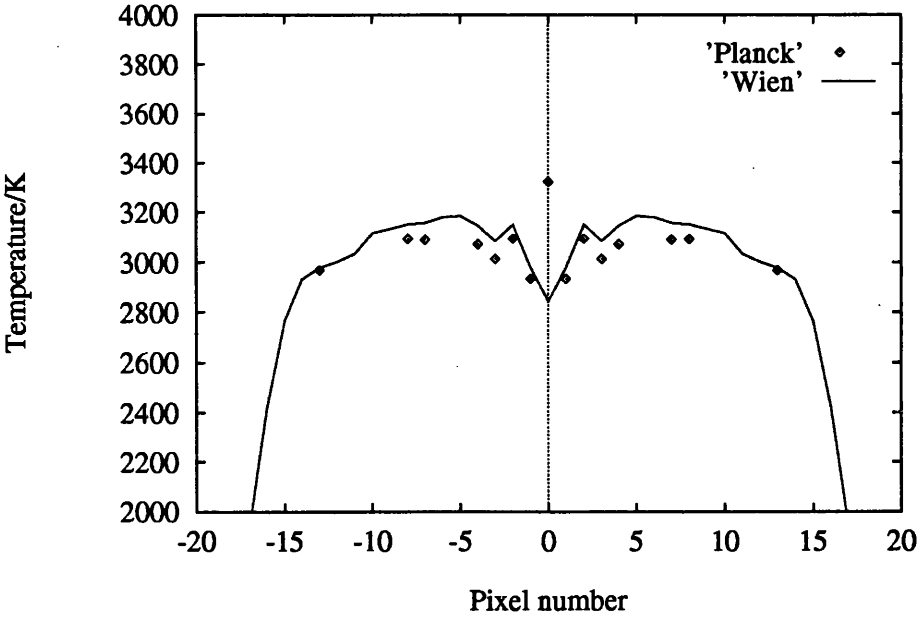

Figure 5.22. Comparison of the Wien and Planck temperature calculation techniques.

Several features may be observed from the data presented in figure 5.22. Firstly, some of the temperatures calculated by the Planck technique have been omitted because they were impossibly high (greater than 10000K in some cases). One explanation for these miscalculations is that in attempting to minimise the sum of squared residuals, the analysis program has found a localised minimum which may in turn be due to an inaccurate first estimate of temperature and/or emissivity. Also, there seems to be little relation between the data points demonstrating this extreme behaviour and their relative positions within the profile. Thus, although theory would indicate a decrease in accuracy of the Planck method with decreasing temperature, experimental measurements do not necessarily support this prediction.

Another observation, which may be drawn from the temperature profiles shown in figure 5.22, is that temperatures, which do not exhibit this extreme behaviour, are all in reasonable agreement with those calculated by the Wien method. However, with the exception of the central point, temperatures calculated by the Planck technique are slightly lower than those found by linearisation of the Wien distribution. The iterative reweighting regression technique used by the Wien method to determine temperature often includes superfluous data from the long wavelength end of the spectrum when the gradient of the linearised Wien curve is determined. As a consequence, the calculated gradient is too low and the calculated temperature, too high. A series of linearised Wien curves and calculated gradients determined from a laser heated spot are shown in figure 5.23.

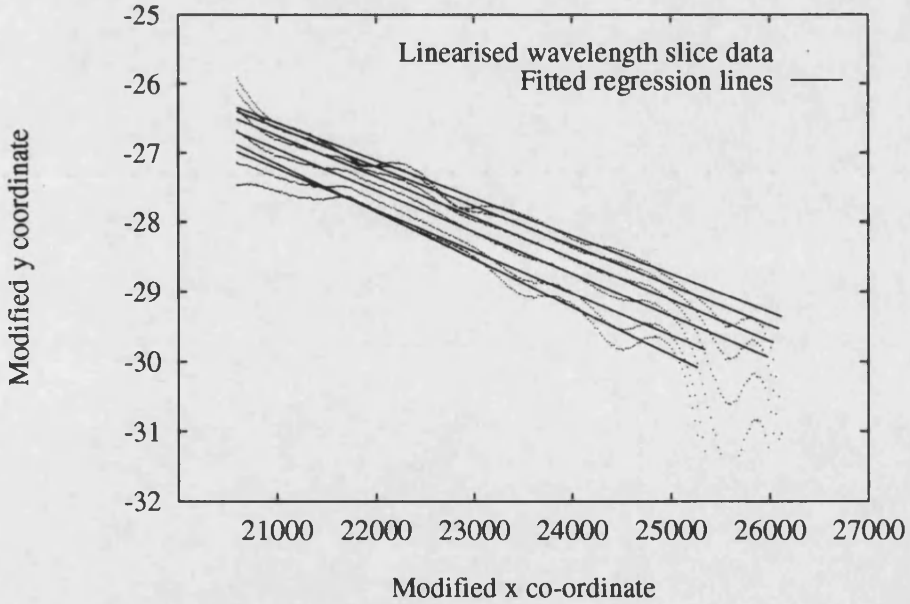

Figure 5.23. Linearised Wien curves and fitted gradients.

The high susceptibility of the Planck method to errors introduced by the wavelength calibration (discussed in section 5.3.1) may also be partially responsible for an observed shift between temperatures calculated by the two techniques. In conclusion, it would seem reasonable to use both temperature measurement techniques but to disregard temperatures calculated by the Planck method which are in considerable excess of the mean value. It has been observed that temperatures found using the Planck technique are either in reasonable agreement with those found by the Wien method, or are wildly different and it is proposed that there would be a very low probability of discarding valid data.

5.4.3. THE APPLICATION OF MEASURED PROFILES

MELTING TEMPERATURE

If the hot spot created on the sample surface contains a region of molten material, the latent heat of melting should cause a plateau in the resultant temperature profile corresponding to the melting temperature of the material. Although Ladds (1994) has used the technique to determine melting temperatures in close numerical agreement with published values, it is suggested that they were unreliable due to the effects of surface deformation discussed in section 6.4.3. Therefore, in order to make a true measurement of melting temperature, a melt puddle must be formed on the sample without deformation of the surface becoming too severe. The results of experiments designed to achieve this in different materials are presented and discussed in chapter 7.

THERMAL CONDUCTIVITY

Tytler (1995) has investigated a number of methods for the determination of the thermal conductivity of a material from a knowledge of the temperature profile formed on its surface by a laser. However, the work described now has highlighted several restrictions which have overlooked in the previous study.

For example, consider a hot spot of diameter d formed on the surface of the test sample. Tytler (1995) concluded that provided the edges of the sample are further than 2d from the centre of the spot, generated temperature profiles would not be affected. In the light of calculations made in section 2.2.2, in which the depth of penetration and thermal time constants were found for a selection of materials, this claim would appear to be unfounded: some allowance for boundary conditions must be included. The position of the hot spot with relation to the sample boundaries has not been found to have any obvious effect on the shape of either the calculated temperature profile or the laser heated site itself. However, this observation is not considered to be conclusive evidence of there being no relationship between the position of the heating site and the resultant data. It is suggested that any trend present is merely masked by the influences of grain boundaries, surface contamination, and/or laser instability, which have been shown to be responsible for corruption of the sample's thermal response.

In addition, characterisation of the laser beam (section 5.1) has highlighted a variation in the size of the beam waist with laser output power. Since a calculation of thermal conductivity requires a knowledge of the input energy characteristics, the appropriate value for beam waist must be included in any calculation of thermal conductivity.

THERMAL DIFFUSIVITY

The inclusion of the programmable time delay unit in the experimental apparatus allows the acquisition of data appropriate to a finite element calculation of thermal diffusivity, that is a series of temperature profiles representing the development of the surface temperature distribution with time. However, the need to maintain a minimum delay between the commencement of laser heating and data acquisition by the CCD/spectrograph assembly (discussed in section 5.2.2) means that materials with a relatively high thermal conductivity will achieve thermal equilibrium too quickly to allow the collection of such data. A series of temperature distributions created on the surface of uranium dioxide (which has a relatively low thermal conductivity, see section 2.2.2) as a function of the delay imposed by the delay unit, have been obtained. These distributions and a discussion of their validity, in terms of surface damage to the sample, are presented in section 7.1.6.

It is now found that to enable the measurement of data for thermal diffusivity calculations on higher thermal conductivity materials, the external laser shutter must be replaced by one which is faster and capable of providing uniform exposure of the sample to laser heating. This would permit a reduction in the minimum heating-acquisition delay time referred to above.

CHAPTER 6

6. EXPERIMENTAL RESPONSE OF THE TEST SAMPLE

The thermal and physical responses of the tested materials have been studied, and comparisons made. The effect of the surface preparation on the optical properties of the test sample has been investigated, and the extent of vaporisation and heat diffusion compared for different materials. The consequence of surface damage in terms of calculated temperature profiles has been quantified, and a study made of the limiting effect of grain boundaries on the flow of heat through the sample. The experimental performance of the sample containment and positioning apparatus has been examined.

Experimental results for individual materials are presented separately in chapter 7.

6.1. THE TEST SURFACE

6.1.1. SURFACE PREPARATION

The need for the surface of the test material to have a reasonably low reflectance of the incident laser radiation was introduced in section 2.2.1. Although the use of a 'greyed' surface (section 4.1.1) has been shown to increase the ability of metallic samples to absorb the incident laser energy, very high laser powers were required to produce a visible hot spot. In addition, extremely long CCD exposures (which for reasons described in section 4.4.2 are best avoided) were needed to record an image. For zirconium and molybdenum, no valid thermal data could be collected.

In general the reflectivity of ceramics is inherently lower than that of metals, and the experimental system will tolerate a more highly polished surface. For example, all three neutral density filters were needed to attenuate the laser beam (operating at a flash lamp current of 22A) enough to allow a measurement of the hot spot image created on a highly polished Bi-Sr-Ca-Cu-O sample.

6.1.2. LAPPING DAMAGE

The need for the test sample to have a flat surface was introduced in section 3.4.2. The lapping process used to achieve this can cause damage to the surface of the test sample in the form of scratches and pitting. Scratches can act as heat boundaries by preferential channelling of heat along their edges, and pitting of the test surface may cause distortion of the hot spot image, thus invalidating collected data. Figure 6.1 shows malformation of the heat affected zone of a laser heated site in zirconium caused by scratches on the sample surface.

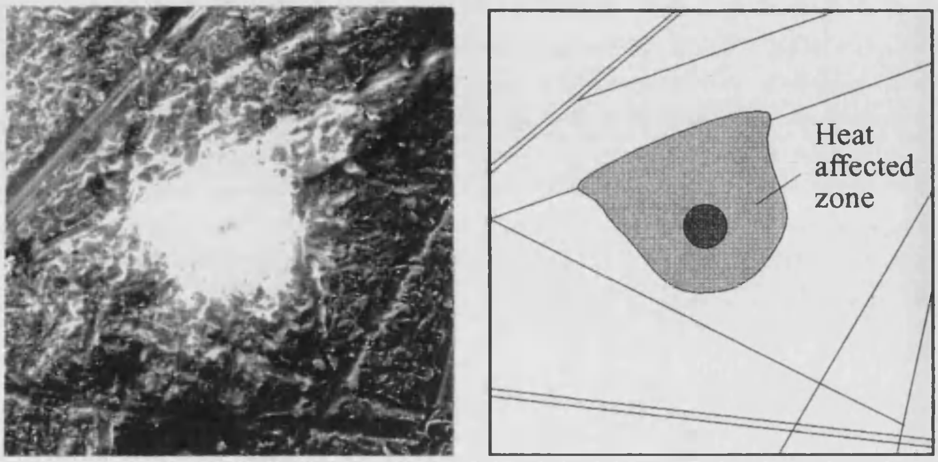

Figure 6.1. Laser heated site on a zirconium sample demonstrating the heat boundary effect of surface scratches (magnification × 180).

Misshapen hot spots always occur when laser heating is performed in the vicinity of surface scratches (as above) and polished samples should be used wherever possible. When the use of a 'greyed' surface cannot be avoided, it is important to ensure, by a microscopic examination of the laser heated surface, that collected data has not been corrupted by surface damage.

6.1.3. SURFACE CONTAMINATION

In addition to the lapping damage described in the previous section, surface oxidation and contamination may also be responsible for the corruption of calculated temperature profiles. Ideally, test samples would be prepared and used immediately but this is not always practicable, particularly if samples are prepared in batches.

The control of surface contamination is more easily achieved than the inhibition of oxide formation. Both influences can be minimised, if samples are prepared 'in-house' to requirements. However, externally sourced materials may be of unknown origin and hence more prone to both types of contamination described. For example, uranium dioxide samples supplied by AEA Harwell have been shown to demonstrate several different surface morphologies on a single sample. Figures 6.2(a) and 6.2(b) are photographs of two regions on the surface of such a sample.

X-ray powder diffractometry has been used to identify iridium contamination on the surface of the uranium dioxide sample shown in figure 6.2 (see appendix C). However, this data was gathered from a comparatively large surface area, and so although the presence of iridium contamination has been proved, the different surface morphologies cannot be directly attributed to this cause. Another explanation for the different surface types is heat damage caused by laser heating of the sample. In view of the considerable attenuation needed to reduce the laser power to a level which will not cause serious deterioration of the sample surface, it is not unreasonable to assume that heat damage may be responsible for causing the morphology shown in figure 6.2(a).

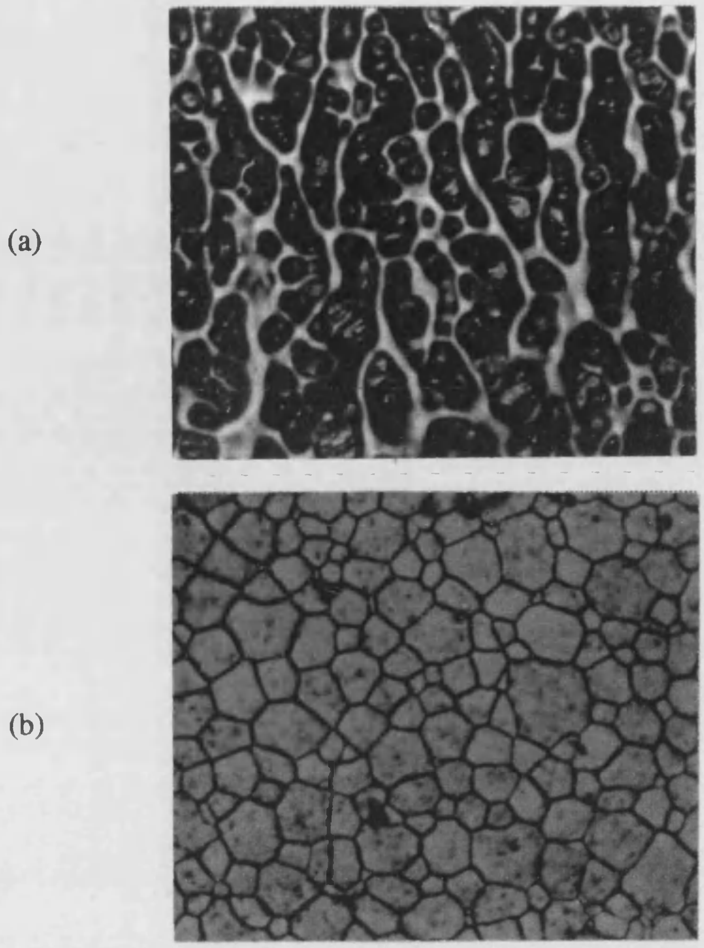

Figure 6.2. Micrographs of a uranium dioxide sample surface demonstrating two different types of morphology (magnification × 160).

In the absence of a more localised X-ray investigation, it is impossible to say whether surface contamination or heat damage has caused the presence of the two clearly different surface morphologies. However, the need to ensure the sample purity at individual laser heating sites has been highlighted.

6.2. VAPORISATION

Table 5.7 on page 126 summarised the laser power density delivered to the test sample as a function of laser flash lamp current. However, to determine the speed of vaporisation of various material surfaces, the absorbed power density as determined by the reflectivity of the material must be found. Table 6.1 shows the absorbed power density of a selection of materials as a function of laser flash lamp current. Note that the absorbed power density values are all approximate, since they are based upon the reflectivity of a typical polished surface at room temperature (see section 2.2.1).

Material	Reflectivity	Approximate absorbed power density as a function of nominal laser flash lamp current/$\times 10^5$Wcm^{-2}			
		31A	28A	25A	22A
Iron	0.675 [1]	3.6	3.3	2.9	2.5
Molybdenum	0.6707 [2]	3.7	3.3	2.9	2.6
Tungsten	0.590 [2]	4.6	4.1	3.6	3.2
Zirconium	0.68 [3]	3.6	3.2	2.8	2.5
Uranium dioxide	0.15 [4]	9.4	8.5	7.5	6.6
$Bi_2Sr_2CaCu_2O_{8+\delta}$	0.1 [5]	10.0	9.0	7.9	7.0
Polycrystalline graphite	0.18 [6]	9.1	8.2	7.2	6.4

Table 6.1. Absorbed power density as a function of laser flash lamp current. Reflectivities according to: [1] Charschan *et al* (1978), [2] Palik (1985), [3] Weast (1976), [4] Gentry (1981), [5] Ginsberg (1992), [6] Reynolds (1968)

A comparison of the values given in table 6.1 and those in table 2.5 on page 45 indicates that even with the laser operating at its lowest flash lamp current, iron, molybdenum, and tungsten would all vaporise within a few milliseconds of exposure to laser heating, effectively ceasing the heating process (section 2.2.3). Although the low reflectivity of uranium dioxide results in high calculated values of absorbed power density, heat loss will be primarily through thermal conduction; surface vaporisation will be minimal. The differing abilities of metals and ceramics to vaporise results in the different types of observed hole formation, which are described in section 6.4.1.

6.3. HEAT CONDUCTION

6.3.1. THE HEAT AFFECTED ZONE

The theoretical size of the laser spot formed on the sample has been calculated to be approximately $4\omega_0$ (see section 2.1.3). However, diffusion of heat into the sample interior increases the size of the effective heated area, and the heat affected zone must be redefined as the area over which the microstructure of the material has been changed. Often the boundary of the heat affected zone is apparent from a microscopic view of the heated surface, although surface contamination and oxidation can cause the region to appear indistinct. Acid etching of the heated surface clearly reveals the heat affected zone, as in figure 6.3, but as surface residues are removed, the diameter of this observed heat affected zone will decrease, thus producing an artificial result. In the following comparisons, the diameters of surface heat affected zones have been considered, but it is important to bear in mind that, for the reasons outlined, such values can only be viewed as approximate.

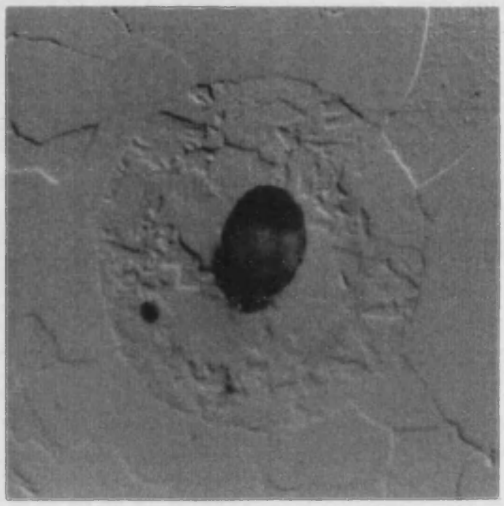

Figure 6.3. Heat affected zone in iron, revealed by acid etching (magnification × 160).

In general the heat affected zones produced on the surface of metals were smaller than those observed in ceramics. However, care must be employed when comparing the effects of laser heating produced on different materials. Consider data presented in table 6.1 on page 167. With the laser operating at a flash lamp current of 22A and with all three optical density filters in the beam path (section 3.2.2), an absorbed power density is produced on the surface of a uranium dioxide sample similar to that created on a metallic sample by a non-attenuated beam produced by a flash lamp current of approximately 25A. The diameters of typical heat affected zones created under these two sets of conditions are 380μm and 200μm respectively.

6.3.2. MEASUREMENT OF HIGH TEMPERATURES

As a direct consequence of the need to impose a minimum setting of the programmable delay unit to overcome problems posed by the external shutter (section 5.2.2), peak measured temperatures have not been as high as anticipated. For example the peak temperature measured on the surface of a uranium dioxide sample was 1800K, which is significantly lower than the melting temperature of ~3100K (see table 7.1).

In having to allow a minimum delay of 800ms between the start of laser heating and the collection of data by the CCD, heat has already been conducted into the interior of the sample, thus reducing its surface temperature. It is suggested that the measurement of high temperatures generated on the surface of materials with a higher thermal diffusivity than uranium dioxide would be even more impractical. Although temperatures of ~2500K have been measured on an iron sample (section 7.3.4), the validity of the calculated temperatures, in the light of the experimental implications of surface damage, remains to be established.

If high temperatures, and the development of the temperature distribution of high thermal diffusivity materials with time, are to be measured, the speed of operation of the external shutter must be considerably improved. Note also that laser damage to the test sample, discussed further in section 6.4.3, may result in a reduction of the peak measured temperature.

6.4. SURFACE DEFORMATION

6.4.1. TYPE OF DAMAGE OBSERVED

Both types of hole formation described in section 2.2.3 have been observed experimentally and examples are shown in figure 6.4. Figure 6.4(a) shows an electron micrograph of a hole produced on a polished iron sample by the laser operated at a stabilised flash lamp current of 29A and using a 3s sample exposure. A hole made by the laser operated at a stabilised flash lamp current of 22A (10ms CCD exposure) on the surface of a nominally stoichiometric uranium dioxide sample is shown in figure 6.4(b).

Figure 6.4(a) shows a hole typical of one in which nearly all of the ejected material has been vaporised almost instantaneously. The edges are comparatively smooth and well defined although there appears to have been some flow of molten material towards the bottom. There is also some evidence of a heat affected zone surrounding the central region. When molten material is ejected from the hole due to a build up of vapour pressure, a hole of the type shown in figure 6.4(b) results. Cracks in the surface are also present and have been observed to extend right across the sample. It is unclear whether these occurred during heating or cooling, although Ford (1967) concludes that the latter case is more probable.

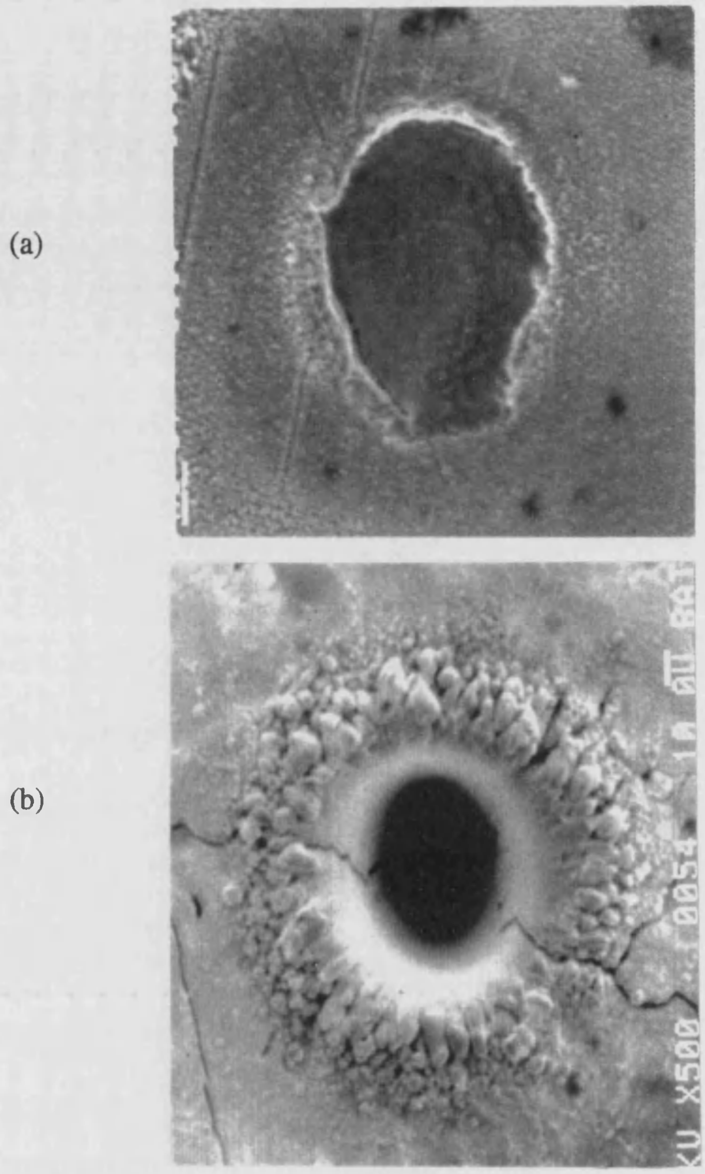

Figure 6.4. Electron micrographs of laser drilled holes: (a) in iron (magnification ×900), (b) on nominally stoichiometric uranium dioxide (magnification ×500).

The ability of metals to change their effective absorptivity upon heating by a laser was discussed in section 2.2.1. This characteristic indicates the presence of a threshold in absorbed laser power above which heating damage will be extreme and below which, less significant. Figure 6.5 shows the surface of an iron sample following repeated exposures to laser heating under the same experimental conditions, using the mapping process described in section 4.1.2. It is apparent from this photograph that there are two types of heat affected zones: one small, one large. Although this observation may, in part, be attributed to instability in laser output, the difference in the appearance of the holes is so great that an effective change of material reflectivity is also likely to have occurred.

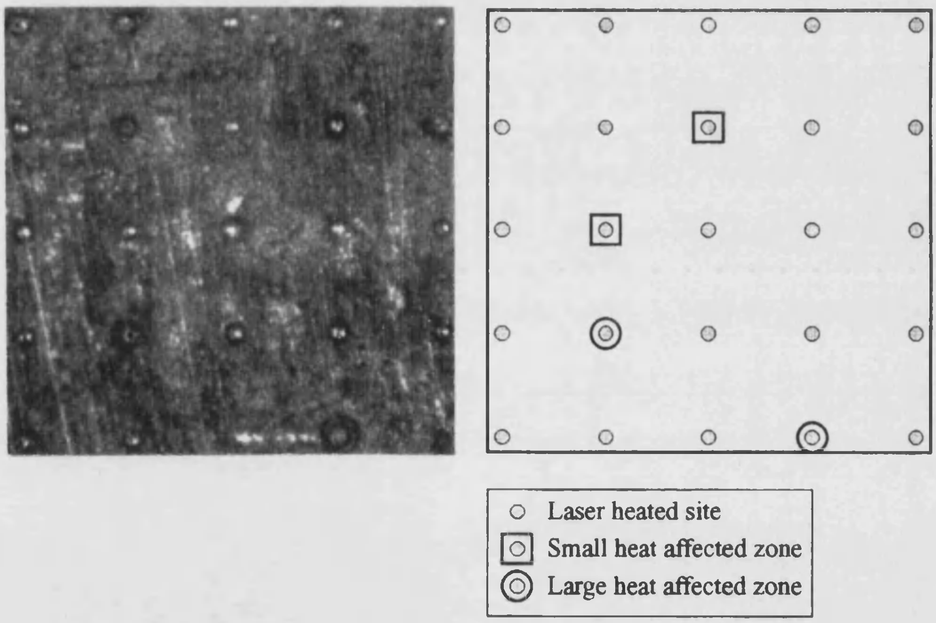

Figure 6.5. Surface of an iron sample following laser heating (magnification × ~40).

The experimental implication of this phenomenon is a further increase in the non-uniformity of results collected under the same experimental conditions, although its effects may be minimised by keeping the exposure of the sample to laser heating as short as possible.

6.4.2. EXTENT OF DAMAGE

The major concern caused by deformation of the sample surface is that once a hole has formed, the laser will no longer be properly focused onto the target, and that the image of the hot spot will no longer be focused accurately onto the spectrograph entrance slit. To determine fully the experimental implications of surface damage, a knowledge of the hole depth is required.

Attempts have been made at measuring hole depths by sectioning and grinding laser heated iron samples, but these have been unsuccessful. Firstly, the precision sectioning of the sample along a row of laser heated sites is difficult to achieve, and also the grinding of soft metallic samples causes their edges to burr over, thus obscuring the holes' cross-section. Hence, a theoretical determination of hole depth is considered here.

Rearranging equation 2.18 on page 47 gives,

$$\ell = \mathrm{A}\mathrm{d}_{\mathrm{m}}. \tag{6.1}$$

Substitution for the maximum observed aspect ratio for metals (section 2.2.3), and the diameter of the hole in iron shown in figure 6.4(a) (12 and 35.3μm respectively) into equation 6.1 gives a maximum possible hole depth (l_{max}) of 423.5µm. Performing the same calculation for the uranium dioxide specimen (maximum aspect ratio = 25 and full hole diameter = 30µm) gives a value for l_{max} of 750µm. These two calculations of l_{max} give hole depths in excess of those likely to be observed in practice. However, the results offer a useful guide for the analyses which follow.

The minimum depth of focus of the laser was found (section 5.1.1) to be 3.76(±0.06)mm. This implies that provided the surface of the test sample is positioned at the centre of the depth of focus, any hole drilled in it by the laser may be up to 1.88mm deep before the beam hitting the base of the hole will be out of focus. It is unrealistic to assume that the sample can be positioned at the absolute centre of the depth of focus, but the value of 1.88mm is still significantly greater than either of the values calculated for l_{max}. Therefore, it may be safely assumed that however deep the laser drilled hole, its surfaces will remain within the depth of laser focus.

6.4.3. EXPERIMENTAL IMPLICATIONS

It has been shown that however extreme the surface deformation caused by the laser, the surface of the test sample will remain within the laser's depth of focus. However, it does not necessarily follow that the image formed at the spectrograph will be unaffected. If distortion of this image is significant, corruption of the resultant temperature calculations will occur.

To determine the effect of surface damage on the resultant temperature calculation, the calibrated light source was shone through the pin hole (section 4.2) placed at different positions along the beam axis and its intensity/wavelength relationship measured by the spectrograph and CCD assembly. For sensitivity calibration purposes the pin hole was first positioned so that the light passing through it was focused at the spectrograph plane; the corresponding z-axis micropositioner value is denoted z_0. This corresponded to a CAC position of 9.78mm. The hole was then moved to either side of this position in turn and the appropriate data collected. The CCD data was converted to temperature and the results compared. In this way the temperature measured from an image, which was out of focus at the spectrograph, could be found and used to gauge the errors introduced to temperature calculations by the laser damage of the test sample. The calculated temperature profiles are presented in figure 6.6 and the central temperature from each profile, plotted as a function of shim position along the laser axis, in figure 6.7. Note that the Abel transform has again caused a dip in the central region of each profile (see section 5.3.2), but a comparison of the temperatures calculated using different CCD exposures may still be made.

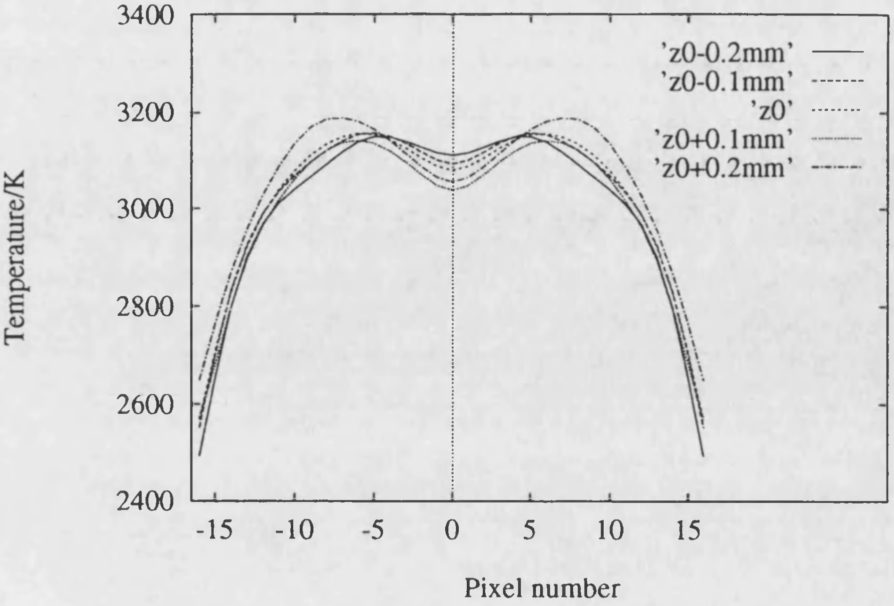

Figure 6.6. Temperature profiles calculated for different CAC z-axis positions.

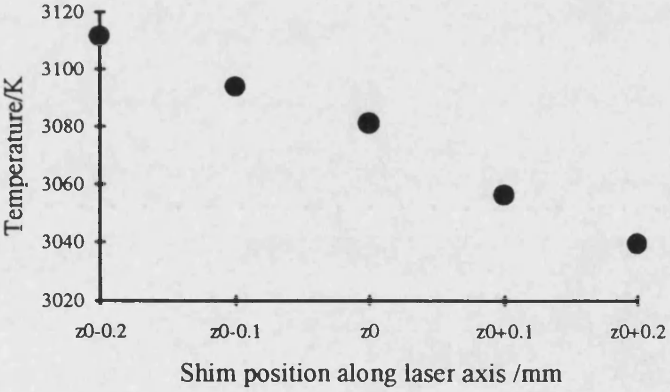

Figure 6.7. Calculated temperature as a function of CAC z-axis position.

It is apparent from figure 6.6 that laser damage to the sample surface, if similar in magnitude to that simulated, will affect the calculation of temperature profiles.

The inaccuracies introduced to temperature calculations by laser damage of the test sample are more easily observed in figure 6.7. Typically, a 100μm deep melt hole will cause a corresponding error in the temperature calculation of ~20K. Since theoretical estimates of maximum hole depth (l_{max}) have been of the order of several hundred microns (see section 6.4.2), it is fair to assume that laser damage may cause a shift in temperature as large as 150K. However, this miscalculation of temperature will not be uniform across the whole of the laser heated site and the edges of the heated region should remain essentially unaffected. Light emitted from the centre of the hole will cause the greatest reduction in calculated temperature, while CCD data emanating from other regions will affect the calculated temperature according to their distance from the centre. Thus, temperature distributions calculated from hot spot images generated from regions of severe laser damage will be artificially 'flattened' in the centre.

6.4.4. MINIMISATION OF SURFACE DAMAGE

Damage to the sample surface could be reduced by decreasing the power density of the laser at the sample. One possibility would be to add an extra, long focal length lens to the optical system between the focusing lens and the test sample and then move the test sample to the beam waist created by the new lens, as shown in figure 6.8.

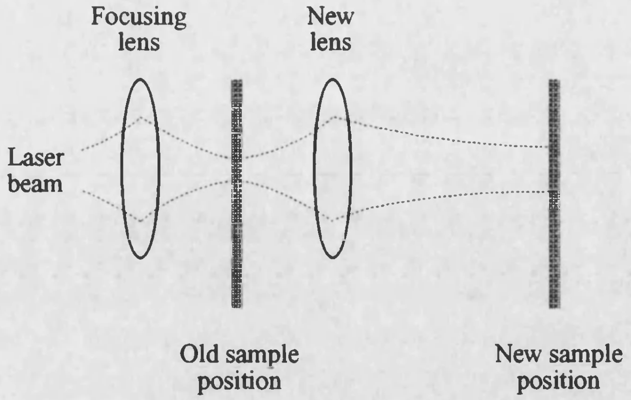

Figure 6.8. Addition of a new, long focal length lens to the optical system to reduce laser damage to the test sample.

The size of the beam waist created by a lens of focal length F may be written

$$2\omega_0 = \left(\frac{4\lambda}{\pi}\right)\frac{F}{D} \Rightarrow \omega_0 \propto F \qquad (6.2)$$

(Newport catalogue, 1990), where D is the diameter of the beam entering the lens. Because the new lens has a longer focal length than the original focusing lens, the size of the waist it forms will be larger, according to equation 6.2. Thus the power density of the laser will be reduced and laser damage to the surface will be less severe. However, there will be a loss in intensity of the hot spot image recorded by the CCD and further work is required to determine the optimum focal length of the new lens, which will allow an appropriate reduction in laser power density without compromising the intensity of the recorded image.

6.5. GRAIN BOUNDARIES

To determine the effect of grain boundaries on heat transfer, an examination of the surfaces of a polycrystalline iron sample and a single crystal zirconium sample, both of which had been exposed to laser radiation, was made.

The iron sample was highly polished and then irradiated by the laser at 10 minute intervals. In all cases, the total sample exposure was 4s. The laser was operated at an unstabilised flash lamp current of 31A (note that at 31A the stabiliser has little influence on laser stability, section 5.1.4). After removal from the CAC, the sample surface was prepared for examination as follows:

1) Polished using a synthetic silk and a 3μm water based diamond solution under a 5lbin^{-2} pressure, to remove pitting caused by the original polishing stage.

2) Polished using a 'microcloth' with a 0.05μm mixed oxide (SiO_2/Al_2O_3) polish under a 2½lbin^{-2} pressure to remove the scratches caused by the previous polishing stage. (Note that although the sample surface was made smoother, it was no longer as flat due to the formation of shallow ripples.)

3) Etched in a 2% 'Nital' solution (HNO_3 in industrial methylated spirit) for approximately 10s.

The zirconium sample was exposed to laser radiation for flash lamp currents of between 22A and 30A. Experimental results are detailed in section 7.5.3. The sample was removed from the CAC and dipped in a zirconium specific etchant for ~30s to remove surface damage caused by lapping. The etchant consisted of 10ml of HF (the etchant itself), 45ml of HNO_3 (to prevent staining caused by the etch) and 45ml of H_2O_2 (to act as a solvent).

After preparation, both samples were examined with a Zeiss optical microscope. A photograph of a typical laser heated site on each sample is shown in figure 6.9. Several features may be observed. For the zirconium surface both the heat affected zone and central hole are approximately circular and concentric. However, these characteristics are not repeated on the iron sample thus indicating that heat transfer was not homogeneous. Furthermore, neither the point of impact nor the heat affected zone is circular, see figure 6.9(a). Sample positioning, which is discussed further in section 6.6.1, could be responsible for an underlying trend in the formation of elliptical regions on the test surface, but as these features have not been demonstrated by the zirconium single crystal it must be assumed that the arrangement of the test sample does not play a significant role in the production of irregularly shaped heating sites.

It is concluded that grain boundaries in polycrystalline materials can act as heat barriers, and that heat will be preferentially transmitted through grains rather than between them. If the material's grainsize is sufficiently large, inhomogenous heat flow should not occur, but as heat affected zones of the order of a few hundred microns have been observed, it is unlikely that such polycrystalline samples will be able to give reliable experimental results. Also, if the temperature measurement system were used in conjunction with a diamond anvil cell (section 1.3.1) the magnitude of the heat affected zone would imply that test samples should be single crystals.

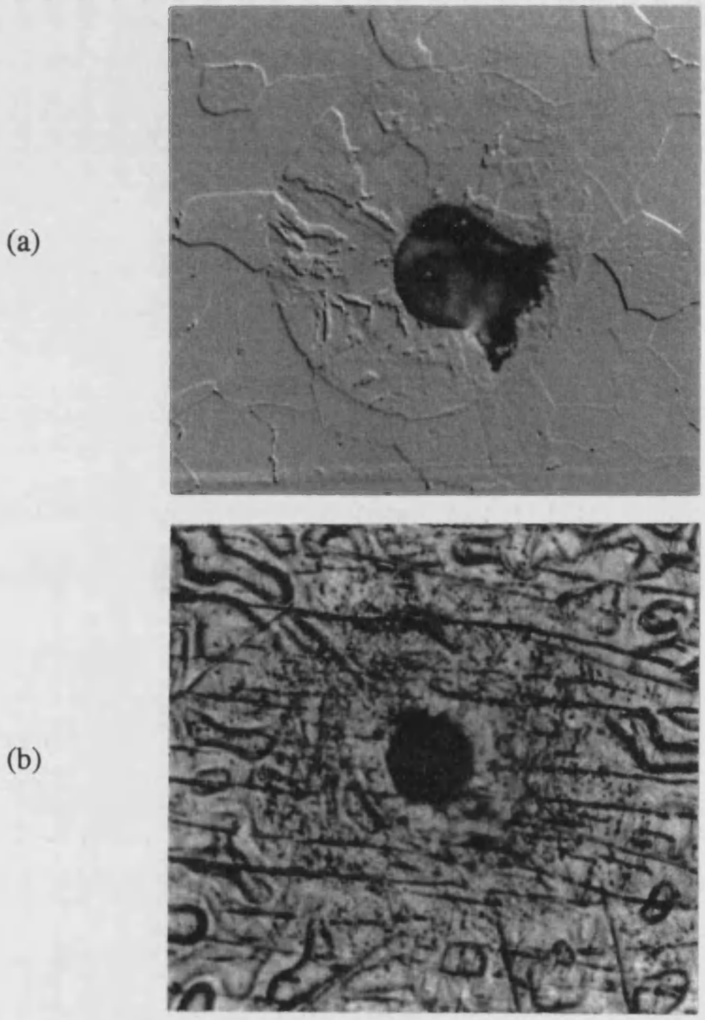

Figure 6.9. Laser heated sites etched to remove lapping damage (magnification × 160): (a) polycrystalline iron, (b) single crystal zirconium.

6.6. CONTAINMENT AND POSITIONING

6.6.1. THE CONTROLLED ATMOSPHERE CHAMBER

During the course of a microscopic examination of samples which had undergone laser heating, it was observed that almost all of the heat affected zones and laser heated sites were not circular but elliptical, even though the circular cross-section of the laser beam had been confirmed by experimental measurement (section 5.1.2). The orientation of the ellipses was the same in each case and might be attributed to the downwards flow of molten material. In some cases, like that shown in figure 6.10, this flow is obvious, whereas in others there is no evidence of material flow and yet the heating site remained elliptical, see figure 6.11.

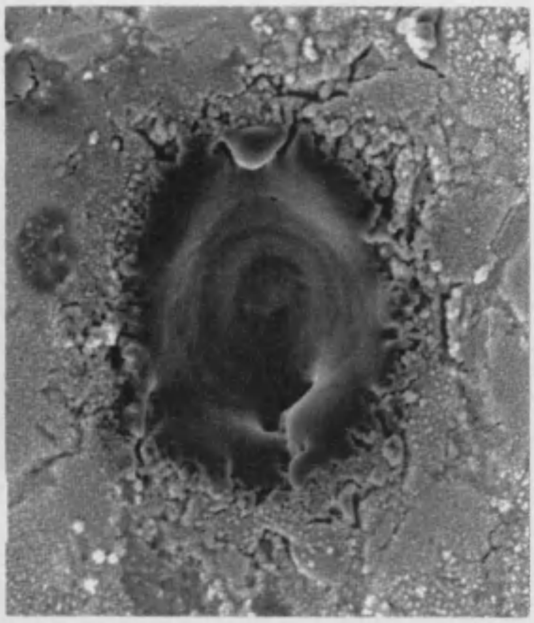

Figure 6.10. Laser heated site in iron exhibiting the flow of molten material (magnification × 900).

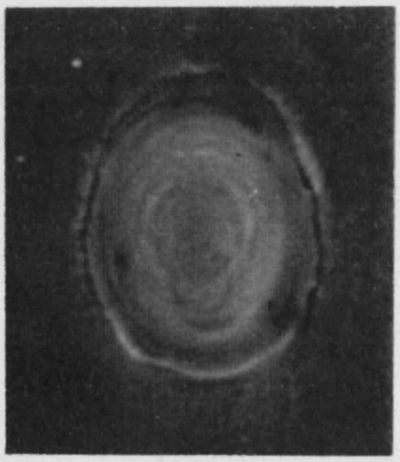

Figure 6.11. An elliptical laser heated site in iron which does not demonstrate material flow (magnification × 900).

An obvious conclusion to be drawn from these observations was that the sample mounting plate was not normal to the laser beam axis, as it had been designed to be. A comparison of the heating sites for which the movement of molten material was not evident yielded values of between 0.73 and 0.91 for the width to height ratio of the heated area. This would indicate that the surface of the test sample was at an angle of between 43.11° and 24.5° to the vertical axis. Since a discrepancy of this magnitude would have been clearly visible, it seems that a rotational misalignment of the CAC cannot be wholly responsible for the formation of elliptical heating sites. Molten material must have contributed to the creation of a non-circular laser heated site even though there was no photographic evidence of it. However, it is suggested that the CAC and micropositioner stage do not allow sufficiently precise positioning of the test sample, and that further investigations into improving the accuracy of alignment of the test surface with regard to the laser beam axis, are needed.

6.6.2. POSITION AND SEPARATION OF HEATING SITES

The mapping procedure described in section 4.1.2 allows a calculated temperature profile to be ascribed to the exact spot on the sample from which it was generated. As a result, any trends in experimental results due to the position of the heating site on the sample should be easily identifiable. During the course of the work described, no such relationship was observed: however, it need not necessarily be concluded that the proximity of the heating site to the sample edge or sample securing plate (see figure 3.13 on page 78) have no effect on the calculated temperature profile. It is proposed that any trend in temperature profile with heating site position is merely being masked by other, more dominant, influences such as surface damage.

Throughout the course of this study heating sites were, by default, located 5mm apart, allowing the formation of a 9×5 matrix on the standard sized test sample. It is preferable to make the heating site separation as small as possible to maximise the acquisition of data from each sample, but care has to be taken to ensure that the laser is not directed at a region containing heat affected material caused by an earlier experiment. Amongst the largest heat affected zones were those observed in uranium dioxide, but even these were small compared with the target site separation. Note that in addition to the normal heat affected zone, large cracks were formed on the surface of uranium dioxide samples at high laser powers. In many cases these cracks were longer than 5mm, but because supplies of uranium dioxide samples were limited, the 5mm separation was retained. In other materials it may have been possible to reduce the distance between heating sites to obtain more data per sample, but this was considered unnecessary due to the abundance of suitable test material.

CHAPTER 7

7. EVALUATION OF TEST MATERIALS

The interaction of a test sample with the experimental system has been considered in chapter 6, and the optimum operating conditions achievable by the system determined. This chapter investigates the experimental performance of various materials to discover whether or not they are appropriate for a study using the system described. This evaluation has allowed the determination of the physical properties desirable in a test sample.

7.1. URANIUM DIOXIDE

The main experimental objectives of the research program, of which the work described within this thesis forms a part, were to determine the thermodynamic properties of uranium dioxide from the measurement of a laser induced surface temperature distribution. Hence, although the extent of experimental investigations was limited by the restricted supply of suitable test samples, the majority of the work undertaken was performed on this material.

7.1.1. URANIUM AND ITS OXIDES

Uranium is a metal belonging to the group of heavy actinide elements. It is a polyvalent element, and as such has a highly complex chemistry; it exists as three different crystal lattices depending on its temperature. Below 662°C it has an orthorhombic structure, between 662°C and 769°C, a tetragonal structure, and from 769°C to 1130°C (the melting temperature), a body centred cubic structure. These are denoted the α, β, and γ phases respectively (Weast, 1974).

Uranium has fourteen isotopes, all of which are radioactive, although naturally occurring uranium consists mostly (~99% by weight) of U^{238}. Another isotope, U^{235}, accounts for most of the remaining 1%. Both isotopes are of great importance as nuclear fuels; U^{235} is used to enrich natural uranium to create a fuel for nuclear power reactors, and the remaining U^{238} may be converted to fissionable plutonium Pu^{239}. Natural uranium, which has a reduced U^{235} content, is known as depleted uranium. The chemistry of nuclear reactor theory has been discussed in some detail by Dawson and Sowden (1963).

The polyvalent nature of uranium introduces four characteristic oxidation states: 3^+, 4^+, 5^+, 6^+. The 3^+ oxidation state is only observed in solids as UF_3, UCl_3, or UI_3, and in the 5^+ oxidation state as UF_5 or UCl_5 (Yemel'Yanov and Yevstyukhin, 1969). The two most important oxidation states are U^{4+} and U^{6+} resulting in the greatest interest being paid to the dioxide UO_2 (cinnamon oxide) and trioxide UO_3 (orange oxide). The uranium mixed oxide, U_3O_8 (black oxide), is also significant since it has been shown that any uranium compound will form it on annealing in air above 700°C (Yemel'Yanov and Yevstyukhin, 1969).

The oxides of uranium are of great interest to the nuclear industry, and many published texts have resulted. Those by Wilkinson (1962), and Kelly and Brooks (1987) are of interest.

7.1.2. ATOMIC STRUCTURE

Below 1200°C uranium dioxide has a fluorite cubic structure (Gronvald *et al*, 1962), fluorite being the common name for the naturally occurring form of calcium fluoride. As far as the author is aware, no data exists for the structure above this temperature and in the absence of adequate information it has been assumed that the structure remains fluorite cubic throughout the experimental temperature range.

The fluorite lattice of UO_2 consists of a cubic structure of oxygen ions with an uranium ion at the centre of alternate cubes. Hence, each oxygen ion is surrounded by four uranium ions in a tetrahedral arrangement as shown in figure 7.1.

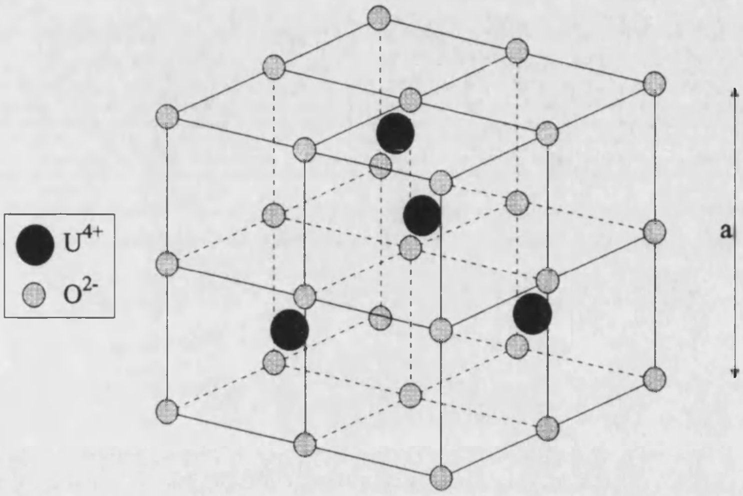

Figure 7.1. The fluorite structure of uranium dioxide.

A comprehensive description of the physical and chemical properties of materials with the fluorite structure has been given by Hayes (1974).

7.1.3. URANIUM-OXYGEN STOICHIOMETRY

The existence of three uranium oxides, UO_3, UO_2, and U_3O_8 has been known for over 130 years. However, work carried out in the 1940s discovered further oxides in the form of hyperstoichiometric (oxygen rich) and hypostoichiometric (oxygen deficient) compounds.

The composition of uranium dioxide has been found to vary from UO_2 to $UO_{2.2}$. Below ~1200°C it consists of two mixed phases (UO_2 and U_4O_9), and above 1200°C as the single phase UO_{2+x}, with the additional oxygen ions contained within the interstitial sites of the UO_2 lattice. If left in the atmosphere, stoichiometric UO_2 absorbs oxygen and gradually assumes a hyperstoichiometric state. If heated in oxygen, this transformation occurs very rapidly, hence the need to perform laser heating of the material in a non-oxidising environment. For experiments performed here, a specific mix of hydrogen and argon was used to prevent the formation of hyperstoichiometric oxides (AEA Technology, private communication).

7.1.4. OXIDE MELTING

Many experimental measurements of the melting temperature of nominally stoichiometric uranium dioxide have been performed. The published results of some of these investigations are given in table 7.1.

Source	Measured melting temperature
Lambertson and Mueller (1953)	3153±20K
Ehlert (1958)	3153±50K
Wisnyi and Pijanowski (1956)	3033±30K
Anderson *et al* (1960)	3073±100K
Kaye and Laby (1986)	3153K
Weast (1976)	3151K
Rand *et al* (1978)	3120K

Table 7.1. Published values of the melting temperature of uranium dioxide.

Many studies on the composition of $UO_{2.0}$ after heating beyond the melting point have also been made. Wisnyi and Pijanowski (1957) claimed no observable decomposition of UO_2 on heating, but subsequent work by Anderson *et al.* (1960) denied this claim. Further work by Rothwell (1961) and MacEwen (1961) not only confirmed decomposition in the form of lattice instability above the melting point, but also identified the inclusion of metallic uranium in such samples. Thus, when laser heating experiments are performed on uranium dioxide it is imperative that a new region of the sample is used each time, and that sufficient space is allowed between adjacent heating sites to avoid recording data from a previously heated area.

7.1.5. TEST SAMPLE SPECIFICATION

AEA Harwell supplied three depleted, polycrystalline, nominally stoichiometric UO_2 samples, the dimensions of which are shown in figure 7.2.

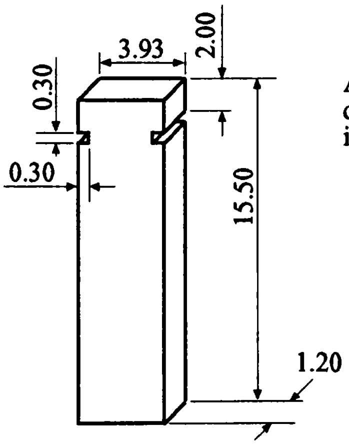

All
dimensions
in mm

Figure 7.2. Dimensions of polycrystalline UO_2 samples supplied by AEA Technology.

The volume of one of these samples was 69.58mm^3, and its weight 0.75g, giving a measured density (ρ_m) of 10.78gcm^{-3}, as compared to the value of 10.96gcm^{-3} quoted by Weast (1976) for the theoretical density of fully dense UO_2 (ρ_t). Substitution for ρ_m and ρ_t in equation 2.14 on page 40 yields a value of 0.016 for the fractional pore volume (f). Substitution for f in equation 2.13 on page 40 gives

$$\kappa_m = 0.984\kappa_t, \qquad (7.1)$$

where κ_m is the measured thermal conductivity, and κ_t is the thermal conductivity of the theoretically dense material. Thus, any measurements of thermal conductivity, made using this sample, need to be corrected according to equation 7.1 before a valid comparison with published values can be made. It has been assumed that all the samples were prepared by AEA in the same manner and that equation 7.1 can be applied to all three.

A micrograph of the surface of one of the three samples, in which grain boundaries are clearly visible, was shown in figure 6.2 on page 166. It is apparent from this figure that the grainsize of this sample is approximately 45μm. All three samples are assumed to have similar grainsize.

7.1.6. EXPERIMENTAL RESULTS

GENERAL OBSERVATIONS

Uranium dioxide, being a dark, almost black, material, is a particularly good absorber of light. With some materials and particularly metals, very high laser powers were required to produce significant sample heating, whereas in an experimental study of UO_2 considerable attenuation of the laser beam was required to prevent excessive surface damage to the sample. This absorption, combined with the brittle nature of the material, makes it susceptible to fracture: nearly all of the samples broke on removal from the CAC.

Figure 7.3 shows clearly how a crack has formed around one side of the laser heating site. This fracture line follows the edge of the heat affected zone due to the poor adhesion between the two microstructure present (heat affected and non-heat affected material).

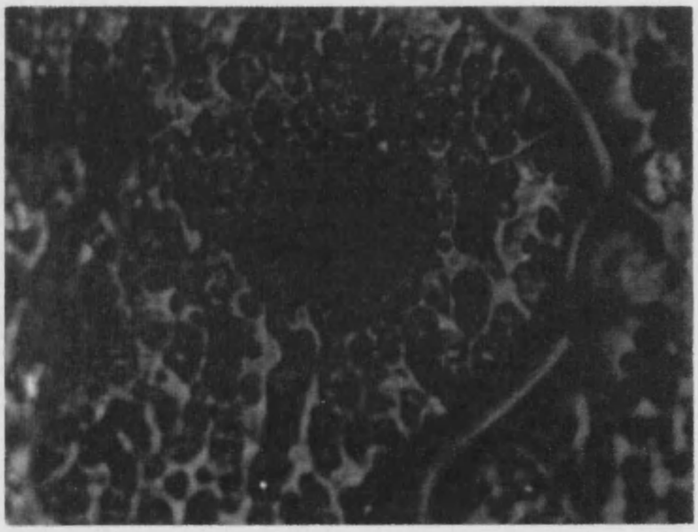

Figure 7.3. Surface fracture on a UO_2 sample indicating the edge of the heat affected zone (magnification × 160).

The relatively low thermal conductivity and reflectivity of uranium dioxide make it particularly suited to an examination by the apparatus described, and allow the measurement of temperature profiles to remain comparatively unaffected by the slow operation of the external laser shutter, section 5.2.1. However, because so much heat is absorbed by the sample, care must be taken to allow it sufficient time to cool between successive laser heatings. In practice, a delay of approximately two hours was found necessary for the sample to cool sufficiently to avoid corruption of the next temperature measurement.

MINIMISATION OF SURFACE DAMAGE

Figure 6.4(b) on page 172 showed the extreme damage caused to the surface of a UO_2 sample by the laser operated at a flash lamp current of 22A (with no attenuation). Such mutilation of the surface is typical, and in the light of hole depth estimations (section 6.4.2) and evidence of the subsequent influence on the data analysis (section 6.4.3), the validity of temperature calculations resulting from such a heating site must be questioned. However, a temperature distribution generated by the laser incident on a UO_2 sample without causing any apparent surface damage, has been measured. The laser power was reduced by three attenuators and a long (2s) CCD exposure used. The resultant temperature profile is shown in figure 7.4 and an electron micrograph of the site from which this data originated, shown in figure 7.5.

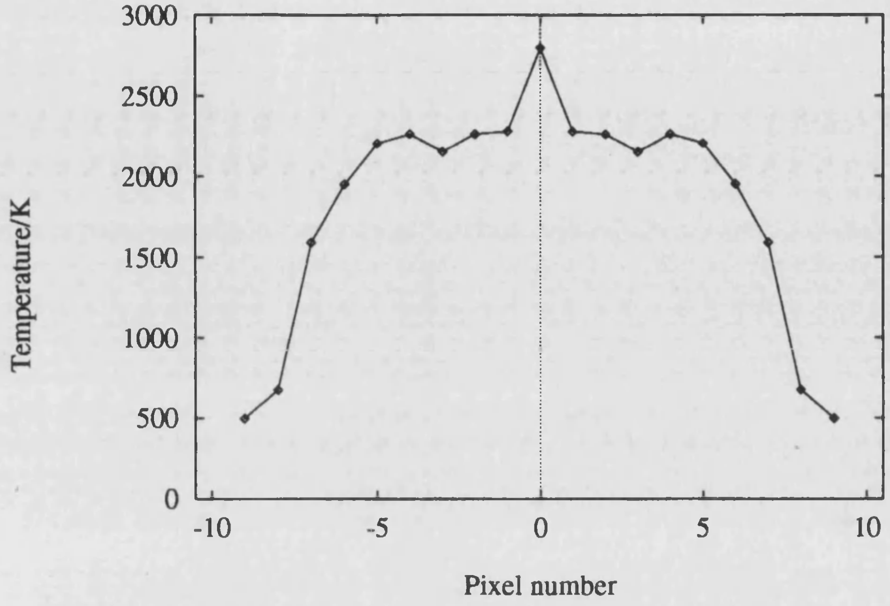

Figure 7.4. Temperature profile created on the surface of a UO_2 sample without causing any apparent surface damage.

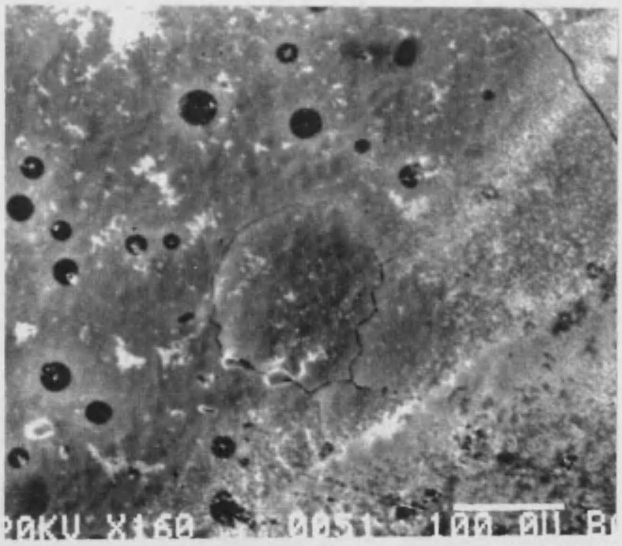

Figure 7.5. Electron micrograph of the laser heated site on UO_2 from which the temperature profile shown in figure 7.4 originated (magnification × 160).

Although figures 7.4 and 7.5 support the theory that temperature profiles can be measured without any visible surface damage being caused by the laser, the length of CCD exposure needed to obtain this data is not ideal. A compromise, which minimises the extent of surface damage whilst keeping the CCD exposure to a reasonable value, must be achieved. To determine such a compromise, an acceptable level of surface damage induced error must be chosen; this error will dictate the maximum admissible hole depth, see section 6.4.3. The laser power may now be increased, and the CCD exposure decreased accordingly, until this hole depth is achieved. However, determining the combination of laser powers and sample exposures needed to achieve a given hole depth is not a straightforward task given the difficulty involved in accurately measuring the depth of laser damage (section 6.4.2). In the case of UO_2 the problem is further compounded by the material's high toxicity, which renders the required cutting and grinding of the sample impracticable.

It is currently unclear what procedural changes can be made, using the existing experimental system, to limit surface damage to UO_2 whilst maintaining sufficiently short CCD exposures. Therefore, it is suggested that CCD data be collected using a reasonable short exposure, and that a qualitative analysis of the heated surface be performed and in cases where surface damage is minimal, it may be assumed that temperature calculations have not been invalidated. However, it remains uncertain what extent of damage will render a CCD image totally unusable.

EVOLUTION OF TEMPERATURE DISTRIBUTION WITH TIME

The evolution of temperature profile with time on the surface of a UO_2 sample, subject to the limitations discussed in the previous section, has been successfully calculated.

A laser flash lamp current of 22A, with the beam attenuated by two of the three neutral density filters, was used to heat the sample in a 2% H_2 in Ar purge gas. The delay imposed by the programmable delay unit was set, in turn, at 1s, 1.2s, 2s, and 3s and the image of the hot spot recorded by the spectrograph/CCD assembly with CCD exposures ranging from 10ms (for a 1s delay) to 20ms (for a 3s delay). Approximately 2 hours were allowed between heating experiments to enable the sample to cool. Calculated temperature profiles (categorised according to the time set on the programmable delay unit) are shown in figure 7.6.

It is apparent from figure 7.6 that the temperature distribution corresponding to the shortest delay (1s) has the highest and narrowest peak. As the delay is increased to 1.2s the height diminishes and the distribution widens. This trend is repeated in the calculated temperature curve for 2s delay. However, there is no significant difference between the temperature profiles for 2s and 3s, and it may be concluded that after approximately 2s the sample has reached thermal equilibrium.

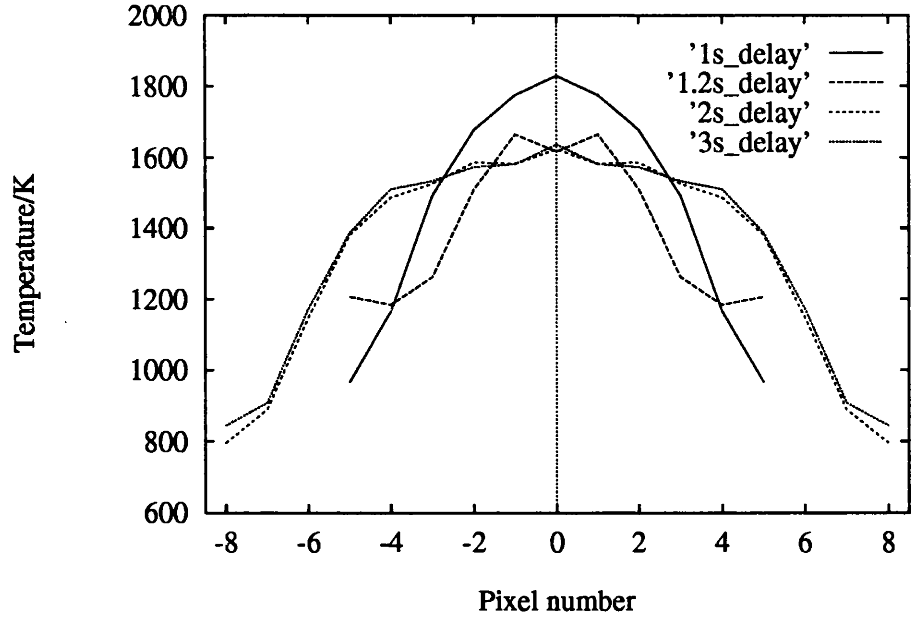

Figure 7.6. Evolution of temperature distribution with time.

Microscopic examination of the surface of the sample, from which the temperature profiles shown in figure 7.6 were generated, shows that surface damage of the laser heated sites was much less extreme than that shown in figure 6.4(b) on page 172. No obvious differences between regions of the sample experiencing different delays were evident, and the heating site shown in figure 7.7 is typical of all those observed.

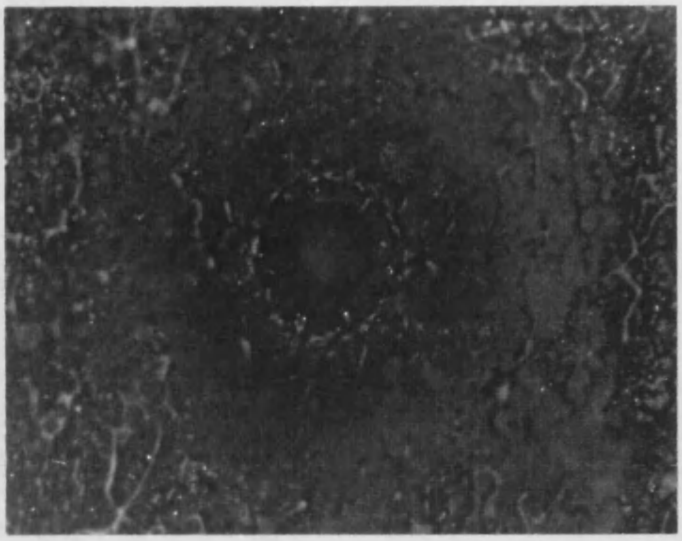

Figure 7.7. Laser heated site typical of that used to generate the temperature profiles shown in figure 7.6 (magnification × 160).

Not only is the damage to the sample not particularly severe, but the CCD exposures used were extremely short (note that 10ms is the minimum exposure made available by the OMA2000 software). These two observations would indicate that the temperature profiles shown in figure 7.6 are worthy of a further numerical investigation such as that described by Tytler (1995).

7.1.7. SUMMARY OF OBSERVATIONS

As a material with a low reflectivity of infra-red radiation, a low thermal conductivity, and high melting temperature, uranium dioxide has been shown to be particularly suited to an examination by the experimental techniques described. Although several experimental limitations have been identified, temperature profiles which appear to not have been significantly corrupted by surface damage, and which may be used for the determination of thermal diffusivity, have been measured.

7.2. Bi-Sr-Ca-Cu-O COMPOUND

The investigation was extended to a study of a Bi-Sr-Ca-Cu-O compound because the supply of uranium dioxide samples was limited. Bi-Sr-Ca-Cu-O compounds and uranium dioxide are both dark, almost black, ceramics and hence have very similar optical properties. For example, the reflectivity of $Bi_2Sr_2CaCu_2O_{8+\delta}$ is of the order of 0.1 (Ginsberg, 1992) compared with a quoted value of 0.15 (Gentry, 1981) for uranium dioxide. The thermal conductivities of these two materials are not dissimilar, but at ~3100K (see table 7.1 on page 191), the melting temperature of uranium dioxide is significantly higher than that observed in Bi-Sr-Ca-Cu-O compounds (see table 7.2). The experimental consequences of both the similarities, and differences between, the two materials are well illustrated by the experimental results described in section 7.2.2.

Several Bi-Sr-Ca-Cu-O compounds belong to the new league of high temperature superconductors, and were readily available within the School of Physics. Note that X-ray diffractometry has confirmed that the material studied here belongs to the Bi-Sr-Ca-Cu-O family, but its precise composition has not been verified, see appendix C.

Material	Melting temperature /K	Reference
$Bi_2Sr_2CaCu_2O_{8+\delta}$	1203	Heeb *et al* (1993)
$Bi_2Sr_3Ca_3Cu_2O_8$	1113	Rao *et al* (1993)
$Bi_2Sr_4Ca_4Cu_3O_{10}$	1123	Komatsu *et al* (1988)
$BiSrCaCu_2O_x$	1150	Komatsu *et al* (1988)

Table 7.2. Published melting temperatures of various Bi-Sr-Ca-Cu-O compounds

7.2.1. PHYSICAL PROPERTIES

Superconductivity in the bismuth-strontium-copper oxides was first discovered by Michel *et al* in 1987, and in the related bismuth-strontium-calcium-copper oxides in 1988 by Maeda *et al.* However, since interest in the Bi-Sr-Ca-Cu-O compounds is almost exclusively concerned with temperatures below 0°C, there is little published data on its physical properties within the experimental temperature range used here. In addition, these materials have a non-stoichiometric composition and are extremely anisotropic, making them somewhat unpredictable test materials. The experimental results presented in section 7.2.2 reflect this unpredictability.

A more detailed study of the structure and composition of the Bi-Sr-Ca-Cu-O family of ceramics is considered to be beyond the scope of this text, and for further information the reader should consult Ginsberg (1992).

7.2.2. EXPERIMENTAL RESULTS

A sample approximately 3mm×2mm×15mm was cut from a piece of Bi-Sr-Ca-Cu-O, the chemical composition of which is discussed in appendix C. To prevent the absorption of oxygen during laser heating, the sample was heated in an argon atmosphere. Because $Bi_2Sr_2CaCu_2O_{8+\delta}$ has an inherently low reflectivity, and the sample used here was assumed to have similar optical properties, its surfaces were highly polished to reduce the power density absorbed by the sample. However, the minimum laser flash lamp current of 22A, with all three neutral density filters used to attenuate the beam, was needed to produce images of the hot spot with an intensity sufficiently low to avoid saturation of the detector. Note, that at 20ms, the CCD exposure used was also very short.

In general, the measured response of the sample to laser heating was erratic. Although the non-repeatability of measurements may be attributed, in part, to the instability of the laser beam at this low power, the anisotropy of the material is the more likely cause. A further experimental limitation was the significant delay required between successive laser heatings for the sample to return to ambient temperature; two and a half hours were allowed in most cases. However, in the course of the study on the Bi-Sr-Ca-Cu-O sample, the temperature profile shown in figure 7.8 was measured. A photograph of the corresponding heating site is shown in figure 7.9. Note that CCD data was collected from other heating sites, but the reconstructed temperature profiles were not of the expected form and are not considered further.

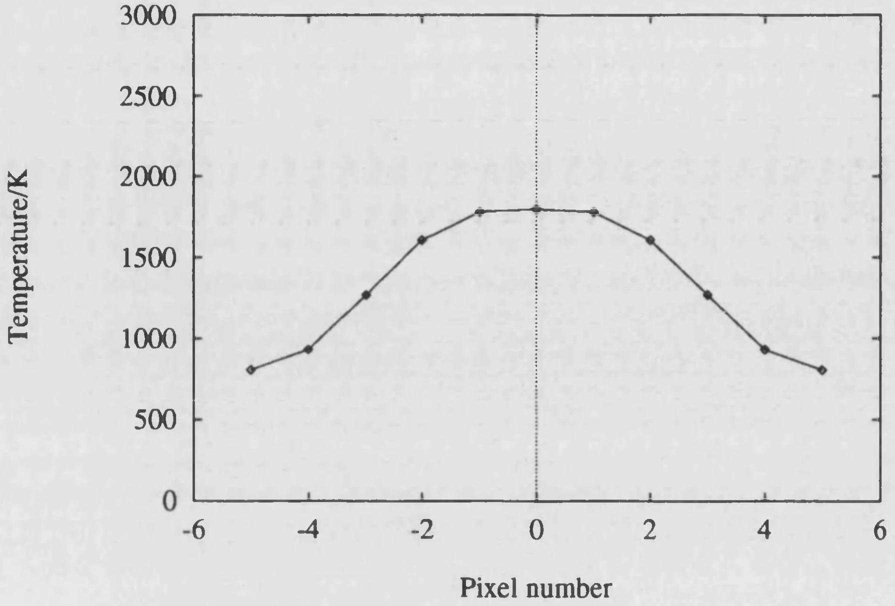

Figure 7.8. Temperature profile measured on the surface of a Bi-Sr-Ca-Cu-O ceramic.

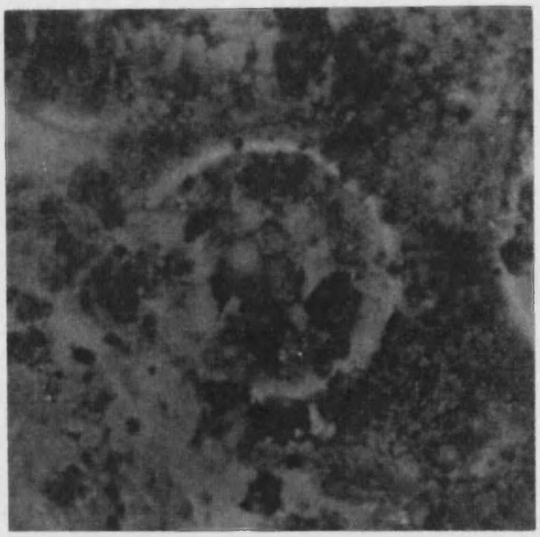

Figure 7.9. Photograph of the laser heating site from which the temperature profile shown in figure 7.8 was generated (magnification ×80).

Several observations may be made from the information presented in figures 7.8 and 7.9. The temperature profile plotted in figure 7.8 includes data from eleven detector pixels. Each detector pixel is 23μm wide; thus, the temperature profile shown in figure 7.8 was generated from a 253μm tall image formed on the detector face. The optical system magnification is 4.29 (see section 3.2.5) and so a CCD image 253μm tall corresponds to a hot spot on the test sample ~59μm wide. The laser heated site shown in figure 7.9 has been magnified 80 times, and so a hot spot 59μm wide corresponds to a circular area ~5mm in diameter in this figure; the central melt zone shown in figure 7.9 has this approximate dimension.

The central region of the laser heated site shown in figure 7.9, from which the temperature profile plotted in figure 7.8 was measured, is non-circular and corresponds to a hole in the sample surface. Note also the presence of a comparatively large heat affected zone surrounding the central region, which is equivalent to an area ~440μm in diameter on the sample surface.

The experimental observations indicate that despite using the maximum attenuation available, laser heating has damaged the sample surface. Although the outline of the central region from which the temperature profile emanated is not particularly clear in figure 7.9, the large heat affected zone indicates that heat damage has been significant. It is also important to note that of all the CCD images recorded for this sample, the temperature profile shown in figure 7.8 was the only one to have the predicted form. Further attenuation of the laser beam to reduce surface damage may allow the generation of reproducible temperature profiles, but it is suggested that the relatively low melting point of Bi-Sr-Ca-Cu-O ceramics (see table 7.2), combined with their high emissivity and anisotropic nature, would make the measurement of reliable data unrealistic.

7.3. IRON

The optical and thermal responses of ceramic materials to laser heating has been discussed in sections 7.1 and 7.2. However, as a readily available material, iron was selected for the application of the described technique to the measurement of laser induced temperature distributions in a metal. At 1530°C (Weast, 1976), the melting point is not particularly high, but the reflectivity is lower than that of many other metals, thus making it a reasonably effective absorber of incident laser radiation. Preparation of test samples was straightforward, and although an oxide layer formed on the surface during storage, it was removed by a short lapping of the surface directly before use.

7.3.1. PHYSICAL PROPERTIES

Iron is the most widely used of all metals and has four allotropic forms, known as the α, β, γ, and δ phases, with transition temperatures of 770°C, 928°C, and 1390°C respectively (Weast, 1976). The α, β and δ phases have a body centred cubic lattice whilst the γ form has a face centred cubic lattice.

Iron is rarely used in the pure form; it is usually found alloyed with carbon and other metals. The pure metal is very chemically reactive and corrodes rapidly in air, particularly at elevated temperatures. The addition to the metal of the oxides of other elements (for example Cr_2O_3, Al_2O_3, SiO_2, or BeO) may be used to help prevent oxidation of the surface. Carbon is added to iron to create steels with a subsequent increase in strength and ductility. The properties of steels are highly dependent on the amount of carbon present and have been the subject of many texts such as those by Nutting and Baker (1965), Vander Voort (1984) and Rollason (1961).

7.3.2. SAMPLE SPECIFICATION

Samples approximately 15mm×4mm×1.9mm were cut from an iron bar (with a grainsize of ~100μm), the composition of which was confirmed by X-ray powder diffractometry. The X-ray results are presented in appendix C. However, during an investigation into the effect of grain boundaries on heat transfer (described in section 6.5) small grains of a pearlite structure were observed. A photograph of such a grain is shown in figure 7.10.

Figure 7.10. Pearlite grain in a suspected iron sample (magnification × ~350).

Pearlite is the laminar aggregate of ferrite and cementite, and is present in all steels. Ferrite is the term applied to substantially pure α iron, and cementite is a hard, brittle compound of iron and carbon (Fe_3C) which contains about 6.6% carbon. Thus iron/carbon alloys are truly iron/cementite alloys. Further descriptions of the interaction of iron and carbon have been made by Tottle (1984).

Although the presence of pearlite indicated that the material was really steel and not iron, the concentration of pearlite was very low. Nevertheless, there is still a small probability of the laser beam hitting a pearlite grain, with a consequent danger of hot spot corruption. Pearlite in the material bulk may also interfere with the evolution of heat through the sample, thus changing the form of the heat affected zone. The first case would become evident from a microscopic study of the heated test surface, but the identification of the latter situation may not be so straightforward.

These experimental observations have highlighted that caution should be employed when using the described experimental technique to study the properties of materials containing aggregate impurities.

7.3.3. HOLE FORMATION MECHANISM

To investigate the mechanism by which a hole is created on the surface of a metallic sample, the polished iron surface was subjected to increasingly long pulses of laser radiation. The resultant damage to the surface was examined using a Scanning Electron Microscope (SEM).

To inhibit oxide formation on the test surface, argon was used as the CAC purge gas. The laser remained stabilised at 28A (corresponding to a scaled DC voltage of 260mV) throughout. The exposure of the sample to laser heating was set at 1s, 2.5s and 3s. Figures 7.11(a), 7.11(b), and 7.11(c) show the surface of the sample after each of the different exposures, and may be used to observe the mechanism by which a hole was formed on the surface. Note that each picture corresponds to a different site on the sample surface. Figure 7.11(a) shows the initial formation of a heat affected zone with little evidence of surface damage. After a 2.5s exposure a puddle of molten material has started to form, which after a 3s exposure has become quite pronounced (figures 7.11(b) and 7.11(c) respectively). Although there does not appear to be any significant surface deformation, the onset of hole formation is clearly apparent in figure 7.11(c). Thus CCD data collected from any of the laser heated sites shown in figure 7.11 would not be corrupted excessively by surface damage. However, attempts to measure a temperature distribution created on an iron surface were not particularly successful, for reasons discussed in the following section.

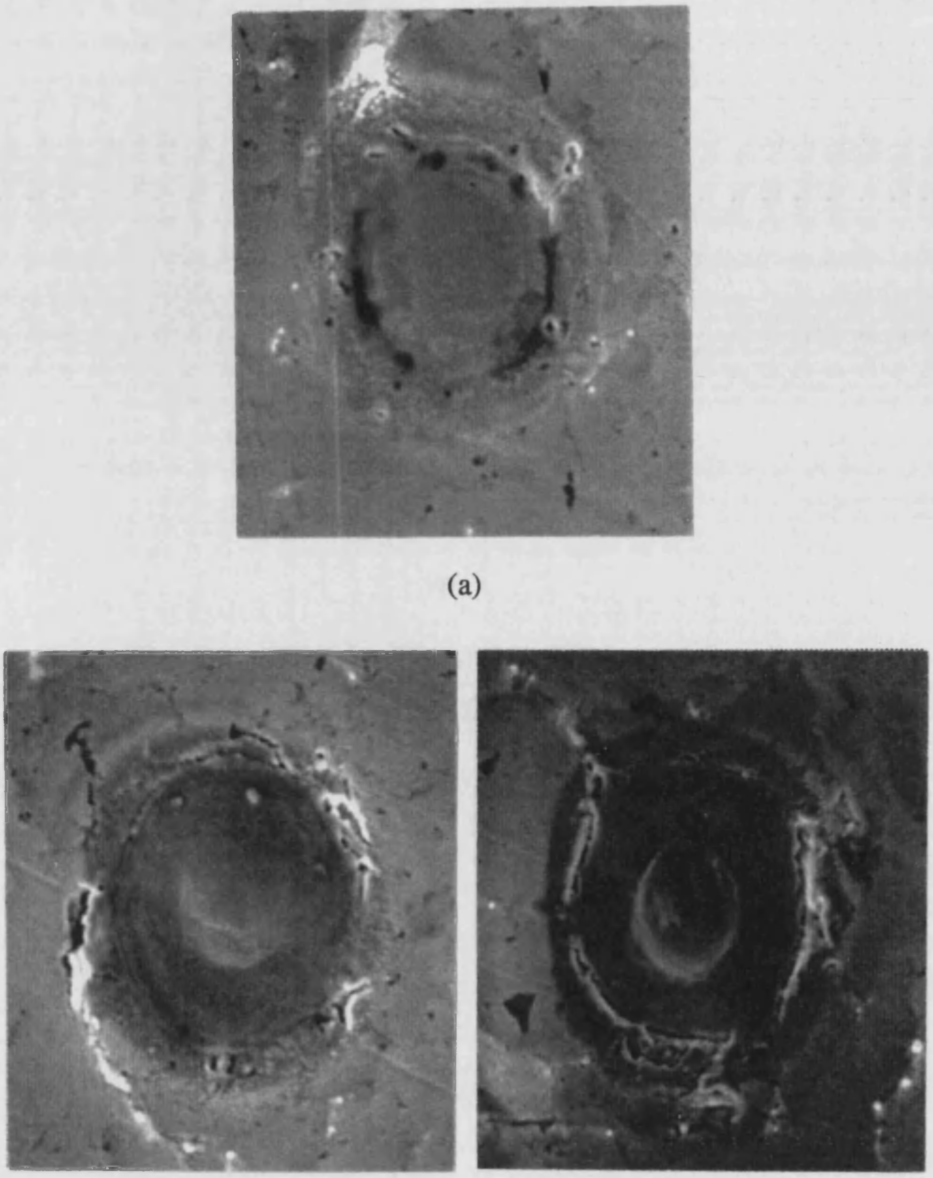

(a)

(b)

(c)

Figure 7.11. Electron micrographs of laser heated sites formed on a polished iron surface: (a) after 1.0s exposure, (b) after 2.5s exposure, (c) after 3.0s exposure.

7.3.4. TEMPERATURE DISTRIBUTION MEASUREMENTS

The measurement of data appropriate for the calculation of temperature distributions was relatively unsuccessful and only a hot spot formed on a greyed surface by the laser operating at a very high power was bright enough to be measured by the CCD. The recorded data was sufficient only to produce a temperature distribution 6 pixels wide, which for the reasons discussed in section 5.5.5, is unsatisfactory. However, there was some agreement between temperature profiles generated from different laser heated sites, two of these are shown in figure 7.12.

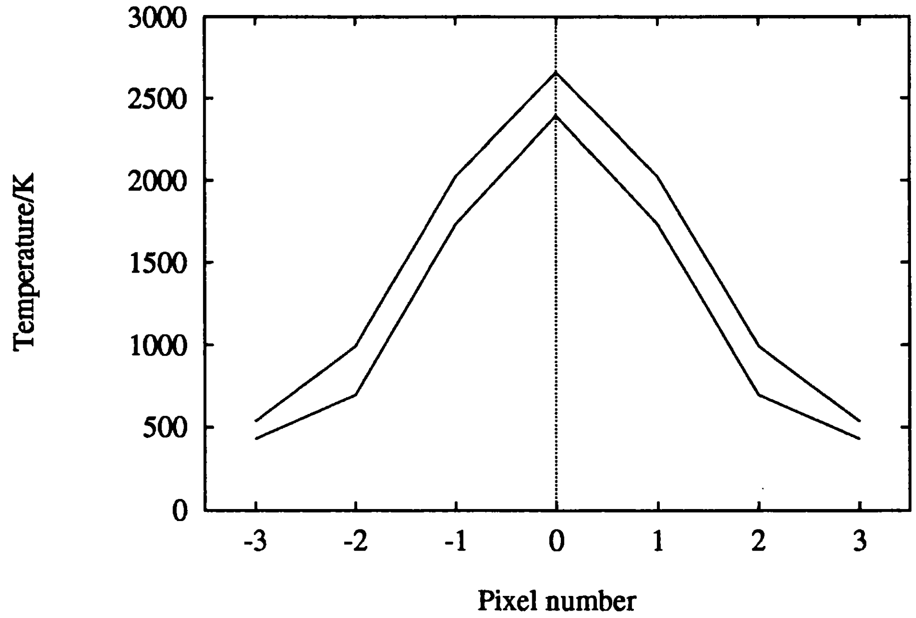

Figure 7.12. Temperature profiles measured from two heating sites on a greyed iron surface.

In section 7.2.2 the width of a measured temperature profile was used to calculate the area of the test sample from which it had been generated. A similar calculation for the temperature profiles, shown in figure 7.12, indicates that they were generated from a region on the sample surface which was 32.2μm in diameter. A laser heated site typical of that used to generate the temperature profiles shown in figure 7.12 is shown in figure 7.13.

Figure 7.13. Photograph of a laser heated site typical of that used to generate the temperature profiles shown in figure 7.12 (magnification ×160).

The hole shown in figure 7.13 has been magnified 160 times: a hot spot 32.2μm in diameter appears as a circular region 5.15mm wide in this photograph. It is apparent from a study of figure 7.13 that the central melted region of the hole has approximately this diameter. Therefore, it may be concluded that the temperature profiles measured on this surface were generated from the small molten region at the centre of the heat affected zone, and not from the heat affected zone itself.

In addition to the uncertainty introduced by the limited size of the image formed on the CCD, the validity of temperature calculations is further questioned by the conclusion that data has only come from a region on the test surface which has melted, and is thus deformed. Because the depth of the hole which has been created is unknown, it remains impossible to quantify the error introduced by the surface damage. Furthermore, although the measured temperatures in figure 7.12 span the published melting temperature for iron (1535°C according to Weast, 1974), no plateaux are evident in the temperature profiles (see section 5.4.3).

The production of a dull image of the hot spot results in the measurement of minimal light at its edges, and a corresponding underestimate of temperature. The inverse Abel transform compounds this error so the uncertainty in temperature at the centre of the profile also becomes large; as a consequence, the shape of the distribution will be of the correct form, but will have been shifted towards a lower temperature range. Hence, a temperature profile, which has been shown to emanate completely from a region of molten material, can have a maximum temperature below that of the melting temperature of the material. Therefore, the collection of broad hot spot images which include non-molten as well as molten material, is imperative if the melting temperature of the test material is to be determined.

7.3.5. EXPERIMENTAL IMPLICATIONS

The ease with which metals vaporise implies that at first sight they would be inappropriate for use as test materials with this experimental system. However, some success has been achieved with iron, in that sample damage was not as severe as expected. Although, at present the validity of collected temperature profiles is questionable, it is proposed that the development of a method for the characterisation of the contours of laser drilled holes, in conjunction with methods described in chapter 6 for the improvement of the experimental technique, could result in the collection of valuable data on the thermal properties of iron. The most significant experimental improvement would be the enlargement of the hot spot on the sample, since the spots formed here were too small for accurate resolution of the profile shape.

Before undertaking any further examination of iron, it is imperative to obtain test samples of a higher purity and larger grainsize to minimise any effects caused by aggregate impurities and finite grainsize, discussed in sections 7.3.2 and 6.5 respectively.

7.4. MOLYBDENUM

Like that of iron, the reflectivity of molybdenum is low compared with that of some other metals, such as copper and silver (see figure 2.3 on page 36), and therefore was considered an appropriate material for the absorption of laser radiation and subsequent measurement of surface temperature distributions. Molybdenum also has a very high melting point and thus it was anticipated that surface damage caused by the laser would be less than that observed in iron.

7.4.1. PHYSICAL PROPERTIES

Molybdenum is a silvery white, very hard metal with a melting temperature of 2500°C (Weast, 1976), which is exceeded only by tungsten and tantalum (of the more readily available metals). Its other physical properties are similar to those of iron. The major use of molybdenum is in steelmaking where it is added to increase strength and hardness, although it has also been recently employed in electrodes for electrically heated glass furnaces. Other uses include nuclear energy applications, and missile and aircraft parts.

7.4.2. EXPERIMENTAL RESULTS

Analysis of molybdenum has shown it to be particularly unsuited to an examination by the experimental system described within this thesis. Data was only measured by the CCD for greyed samples irradiated by the laser operating at its highest possible power using a CCD exposure in excess of 18s. Although temperature profiles were calculated, they were deemed invalid due to both the extremely long CCD exposures used and the abnormal RLE images obtained. The RLE image produced by a typical ‘good’ raw data set is shown in appendix B. Those obtained for molybdenum demonstrated several unusual features such as a skewing of the distribution and the appearance of two separate images. Such RLE images are shown in figure 7.14, but note that the secondary images are very faint.

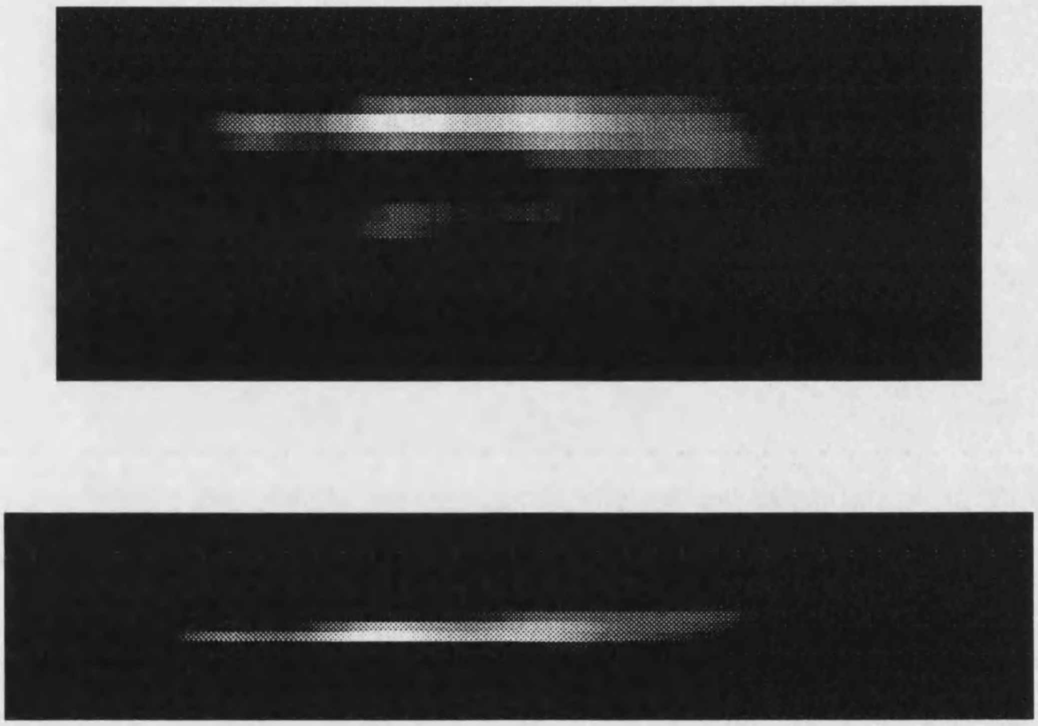

Figure 7.14. Abnormal RLE images of hot spots created on the surface of a greyed molybdenum sample.

One explanation for these unusual images is that damage to the sample has caused the reflection of additional light from features created on its surface. However, observation of a typical laser heated site, see figure 7.15, indicates that this is unlikely to be the case since there has been no obvious distortion of the surface. Thus, the corruption of the images presented in figure 7.14 has been attributed to the extremely long CCD exposures used. It is suggested that the sample surface has been exposed to laser heating for a sufficiently long time for a noticeable thermal expansion to occur which in turn has caused a drift in the spatial position of the image formed on the detector. This suggestion is well supported by the photograph of the laser heated site shown in figure 7.15 which, although demonstrating little fundamental damage, displays evidence of a heat affected zone.

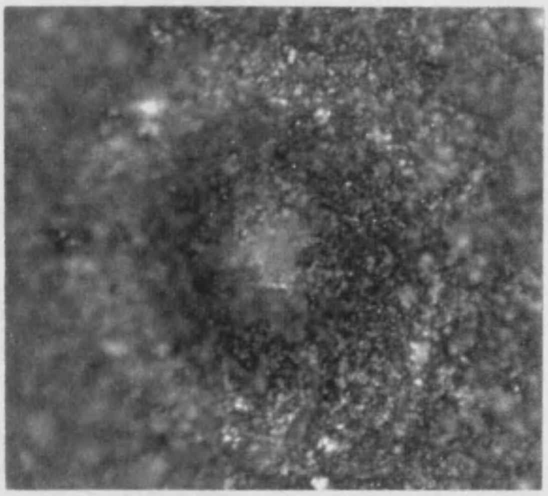

Figure 7.15. Laser heated site on a greyed molybdenum surface (magnification × 400).

Although heating experiments performed on molybdenum have not yielded valid temperature profile data, they have provided evidence of the earlier indications (section 5.2.2) that CCD exposures must be kept to a minimum.

The inability of molybdenum to support a laser heated hot spot, which is detectable by the spectrograph/CCD, may be attributed to its high thermal diffusivity (see table 2.3 on page 41). This value accounts for the obvious presence of a heat affected zone, but little other heat damage in figure 7.15.

7.4.3. EXPERIMENTAL IMPLICATIONS

In the case of lower thermal diffusivity materials for which temperature measurement was not wholly successful, for example iron, it was proposed that improvements to the experimental system, which have been described in chapter 5, could result in the acquisition of useful and valid data. However, it seems unreasonable to predict that these improvements could allow the successful study of a material with as high a thermal diffusivity as molybdenum. In the light of this discussion it was also considered unprofitable to study materials with even higher thermal diffusivities, such as tungsten.

7.5. ZIRCONIUM

To enable a comparison between the experimental behaviour of polycrystalline and single crystal metals, test samples of both have been studied. Results of experimental investigations into the behaviour of polycrystalline iron and molybdenum samples have been discussed in sections 7.3 and 7.4 respectively. The study of the behaviour of a single crystal of zirconium, introduced in section 6.5, is continued here.

As a silvery white metal, the optical properties of zirconium, with regard to the experimental technique described, are far from perfect. However, at 1852°C (Weast, 1976), the melting temperature is higher than that of iron, and at $0.13\text{cm}^2\text{s}^{-1}$ (see table 2.3 on page 41), zirconium has the lowest thermal diffusivity of the metals studied here. Since metallic single crystals are not easily prepared and the experimental technique is of such a destructive nature, the study of such samples was deemed to constitute a very poor use of resources. However, the School of Materials Science were able to supply one test sample of single crystal zirconium for a study employing the described technique.

7.5.1. PHYSICAL PROPERTIES

Zirconium has a broad range of industrial uses: a cladding material for nuclear reactors, as a pigment in the manufacture of plastics, in the fabrication of steel. Preparation of the material is difficult since zirconium powder is very reactive and can be explosive; its ignition temperature being only 20°C (Browning, 1961). The solid metal ignites less easily, but is still highly susceptible to oxidisation in air. Pure zirconium is a very soft, ductile material, whereas impure zirconium is much harder and brittle.

7.5.2. SAMPLE SPECIFICATION

Zirconium has a hexagonal close packed structure below 850°C, above which it is body centred cubic (Swanson *et al*, 1953). A sample 15.03mm×4.25mm×0.68mm was cut from a single zirconium crystal, formed from a pulled boule, as shown in figure 7.16, and its surfaces greyed (section 4.1.1). The material's composition was established, and the high purity of the sample confirmed by X-ray diffractometry (see appendix C). The orientation of the sample, in relation to the principle crystal axes, was determined by Laue photography, which was also used to confirm the sample mono-crystallinity.

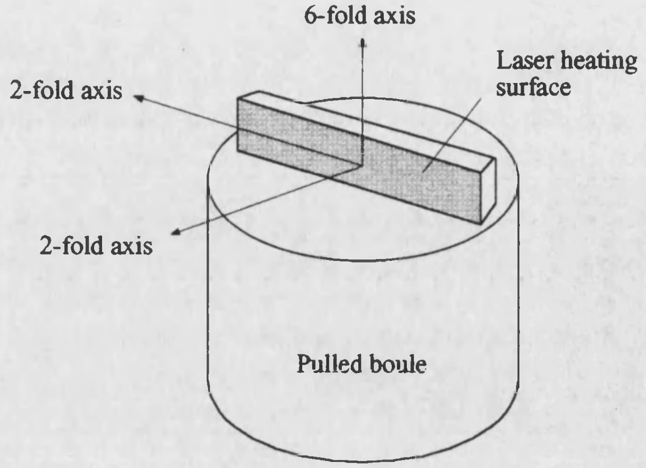

Figure 7.16. Orientation of the cut zirconium sample showing symmetry axes.

7.5.3. EXPERIMENTAL RESULTS

Heating experiments were performed using laser flash lamp currents of between 22A and 30A, using argon as a purge gas to inhibit both the formation of an oxide layer, and the ignition of the material.

Although the CCD detected hot spot images formed on the sample for all the considered laser powers, none resulted in temperature profiles of the predicted form. The inability of the experimental system to record valid temperature profiles may be attributed to the very narrow images recorded by the CCD; the widest recorded image covered only five detector pixels. Also, the CCD exposures required to successfully record these images had no obvious relationship to the laser power used to produce them; in some cases the measurement of the image of a hot spot produced by a high laser power required a longer CCD exposure than that produced with a lower power. For example, at a flash lamp current of 22A, a

1s CCD exposure was required, whereas for 26A, a 3s exposure was needed. The peak intensity measured by the detector was similar in both cases.

The unpredictability of measurements made using zirconium has been attributed to the readiness with which an oxide layer forms on its surface. As a highly reflective material, some doubt had been expressed as to the ability with which zirconium would absorb laser radiation. However, its capacity to produce hot spots recordable by the CCD, combined with evidence of damage caused to the surface by laser heating, see figure 7.17, indicate that significant laser radiation absorption had occurred. It is proposed that the formation of a non-uniform oxide layer on the surface of the test sample prior to heating has seriously changed the local absorption characteristics of the material, thus affecting the amount of laser light absorbed, and subsequently the amount of visible light returned to the detector. The need to control oxide growth, which was introduced in section 6.1.3, has thus been confirmed.

Note also that the test sample used was comparatively thin, which combined with the high ductility implied by the considerable purity of the material, indicates that the sample was prone to distortion, either during surface preparation or laser heating. Although surface oxidation has been partially responsible for the creation of unreliable experimental measurements, such distortion may also have contributed towards the invalidation of collected data.

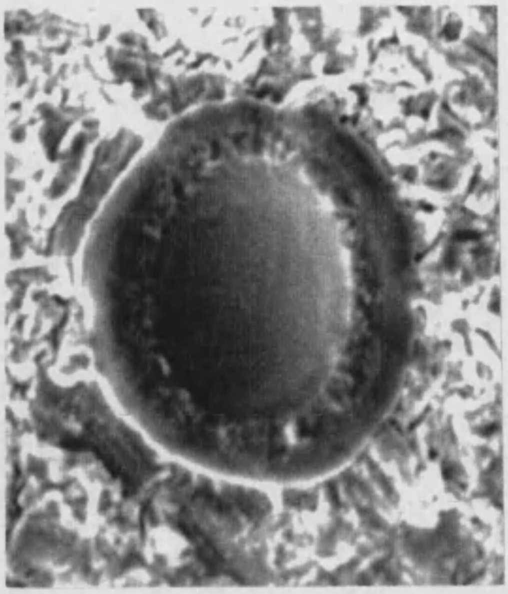

Figure 7.17. Laser heated site on a greyed zirconium sample indicating evidence of laser damage (magnification × 900).

7.6. GRAPHITE

As a material with a relatively low reflectivity, high thermal stability, and low thermal conductivity, graphite was proposed as an appropriate material for study using the experimental system described. However, like the Bi-Sr-Ca-Cu-O material studied in section 7.2, graphite is strongly anisotropic; the experimental implications of this anisotropy are discussed further in section 7.6.2.

7.6.1. PHYSICAL PROPERTIES

Graphite is a material of very broad technological importance. Originally developed in large quantities for use in electrodes, the development of the nuclear reactor lead to its widespread use as a neutron moderator. As a direct consequence of its great strength at very high temperatures, graphite is also used in various spacecraft components.

Graphite often occurs in combination with other forms of carbon such as chars, lampblacks and soots which have ill-defined physical properties. For this reason, it is generally accepted (Reynolds, 1968) that any carbon demonstrating a well developed layer structure, in which the atoms are arranged in open hexagons and the layers show some order in stacking sequence, may be called a graphite.

The atoms within each layer are 0.14nm apart and bound by strong covalent bonds. Layers are separated by 0.33nm and bound by weak van der Waals' interactions (Wyatt and Dew-Hughes, 1974). The anisotropy in the structure of the material is repeated in its physical and mechanical properties. Strength, optical reflectivity, and thermal and electrical conductivities are high parallel to the hexagonal planes, and low in the perpendicular direction; as a result the properties of polycrystalline graphite are somewhat unpredictable. Graphite does not have a melting point at atmospheric pressure, but sublimes at 3367(±25)°C (Kaye and Laby, 1986).

The physical and thermal properties of graphite have been considered in more detail by Hooker *et al* (1963), Klein and Holland (1964), and Taylor (1966).

7.6.2. EXPERIMENTAL RESULTS

Several samples approximately 15mm×4mm×1.8mm were cut from polycrystalline, synthetic, nuclear grade (high purity) graphite, the chemical composition of which was confirmed by X-ray diffractometry (see appendix C). The surfaces were greyed according to the description given in section 4.1.1 and the samples heated, in an inert argon atmosphere to prevent oxide formation, by the laser operating at a flash lamp current of 27A.

Resultant temperature profiles were not particularly wide, and only a few were of the predicted shape. However, some calculated profiles were of the expected form and demonstrated some degree of consistency. These are plotted in figure 7.18.

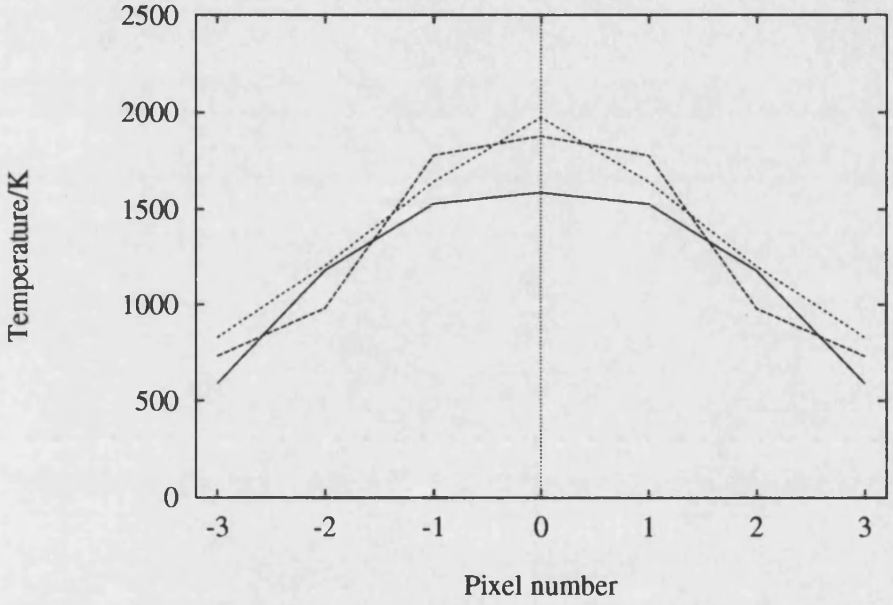

Figure 7.18. Temperature profiles generated on the surface of graphite using a laser flash lamp current of 27A.

The laser heated sites, from which the temperature profiles shown in figure 7.18 were measured, demonstrated very little evidence of surface damage. A typical laser heated site is shown at the centre of figure 7.19.

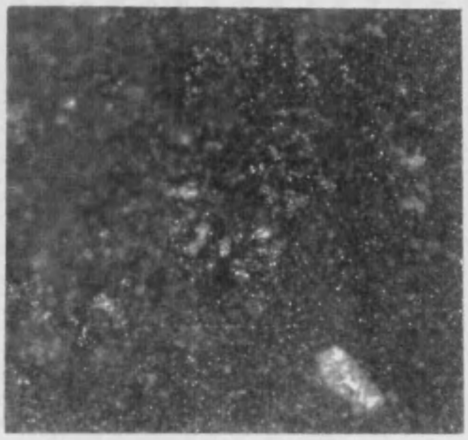

Figure 7.19. Laser heated site on a graphite sample (magnification × 160).

It is apparent from the laser heated site shown in figure 7.19 that the temperature profiles plotted in figure 7.18 have not been corrupted by surface damage. If all measured profiles were of the form shown in figure 7.18, and the width of calculated profiles could be increased by methods discussed previously (section 6.4.4), graphite would be an excellent choice of test material for the experimental and analytical procedures described within this thesis. It is proposed that malformed temperature distributions were the result of the inherent anisotropic nature of the material, and are thus unavoidable. Ideally, single crystals of graphite would be used as test samples, but since the largest single crystals are only a few millimetres across, liable to shear easily, and very rare, their use would be highly impracticable. However, the introduction of a non-subjective procedure for the selection of valid profiles from all those calculated would permit the use of polycrystalline graphite as a sound test material for future work.

7.7. OTHER MATERIALS

Experimental results obtained for a variety of test materials have been described in sections 7.1 to 7.6. Several other materials have also been considered for use as test materials, but for various reasons they have produced no experimental data. However, for motives outlined below, they are each worthy of a brief description here.

7.7.1. ZIRCONIA

Zirconia is a white crystalline powder consisting of zirconium oxide (ZrO_2). It has a high melting point (2950°C, [Tottle, 1984]), and as such was considered worthy of an examination by the experimental system described. Knowledge of the behaviour of ceramics within the experimental environment would also be expanded by such a study.

A disc of sintered zirconia approximately 4cm in diameter was provided by the School of Materials Science, and a peripheral diamond blade saw used to cut an appropriately sized test sample. However, the extreme hardness of the sample was found to render sample preparation by this technique impracticable, and no experimental work was performed on the material.

Because high melting temperature ceramics have, in the course of this study, been found to be appropriate to a study by the techniques described, it is suggested that in future work, and provided that a suitable test sample can be prepared, zirconia is used as a test material.

7.7.2. ALUMINA

A sample with dimensions of approximately 14mm×5mm×3mm was cut from a block of an alumina ceramic, and the surfaces greyed according to the description given in section 4.1.1. The laser operating at a flash lamp current of 22A was used to heat the sample, and the CCD exposure set at 3s; there was no evidence of surface damage and the image of a hot spot was not detected. The laser flash lamp current was increased, but even with a current of 30A and a CCD exposure of 30s, no optical response was detected.

In the absence of any specific physical data about the material, it was concluded that the surface of the test sample was too reflective to absorb sufficient laser energy to heat it to a measurable temperature.

7.7.3. TUNGSTEN

Tungsten is a steel-grey metal with a high density and mechanical strength, and is unusual in its ability to resist oxidation other than at extremely high temperatures.

It also has a relatively low reflectivity of Nd:YAG laser radiation, as demonstrated by the data presented in figure 2.3 on page 36.

It was originally proposed that the material properties of tungsten would make it an appropriate choice as a metallic test sample. However, later work conducted on molybdenum indicated that metals with a high thermal diffusivity were unsuited to an examination by the technique described here. Since tungsten has an even higher thermal diffusivity than molybdenum (see table 2.3 on page 41), its use as an experimental test material was not considered worthwhile.

CHAPTER 8

8. CONCLUSIONS AND RECOMMENDATIONS

The objective of the work described within this thesis was to perform an evaluation of a remote temperature measurement technique designed by Ladds (1994). The viability of the method has been verified, and temperature profiles which demonstrate the evolution of temperature with time have been measured. Improvements which would enhance the capability of the system have been highlighted, and practical steps which could be taken to achieve such improvements are described. The determination, and subsequent use, of the optimum experimental parameters have allowed the performance of the data acquisition and analysis procedures to be maximised. A variety of different materials have been studied, and the intrinsic and extrinsic properties of these materials, which allow the calculation of the most reliable temperature profiles, have been investigated. The preferred test sample attributes have been deduced.

The conclusions drawn from the experiments detailed in this text are now discussed in the order defined by the work outline described in section 1.4 on page 25.

Firstly, a few practical limitations of the experimental apparatus have been isolated, one being the inadequate power stability demonstrated by the Nd:YAG heating laser. It has been shown that fluctuations in the width and peak intensity of its beam are inherently lowest for a laser flash lamp current of approximately 26A, and that at this power the laser stabiliser is unable to make any significant improvement to the output stability. Therefore, it is recommended that in future work the laser is operated at 26A, and that lower power densities are achieved by attenuation of the beam. Higher powers are best avoided, unless required to heat highly reflective samples.

The mode of operation of the external shutter has been identified as the cause of the inability of the experimental system to record reliably high temperatures generated on the surface of a test sample. The difficulty of measuring data suitable for the determination of thermal diffusivity of high thermal conductivity materials using such a system, has also been discussed. The replacement of the shutter with one which operates faster and gives a more uniform exposure of the sample to laser heating, for example a Pockels cell, has been endorsed.

The practical effects of an increase in the magnification of the hot spot image by the optical system have been investigated. Although a higher magnification would result in the measured profiles being constructed from more calculated temperatures, wavelength convolution at the detector would be increased. It is concluded that the existing value for the optical system magnification of 4.29, although not ideal, is an acceptable compromise between these two conflicting demands.

In the course of performing spectral sensitivity corrections, an instability of the CCD/calibrated lamp arrangement was identified. Although an investigation into the source of this phenomenon has been made, the non-uniformity of the measured spectral response of the calibrated lamp could not be attributed to a single specific cause. It is suggested that a more comprehensive study of the performance of this apparatus may isolate the origin of the problem.

The microscopic examination of heated samples has indicated that despite being heated by a laser beam of circular cross-section, the heated sites are elliptical in shape. This observation has been attributed to the downwards flow of molten material, although the alignment of the CAC with respect to the laser axis has also been brought into question. It is proposed that a rearrangement of the optical system so that the heated surface of the test sample is horizontal rather than vertical, would enable the identification of any misalignment of the test sample by preventing the flow of molten material.

In order to measure a valid temperature profile from the surface of a laser heated sample, several conditions must be satisfied. The first of these is that the heating laser beam must be symmetrical and have a Gaussian transverse power distribution. Laser characterisation achieved with a beam profiler has confirmed that the Nd:YAG laser satisfies both these requirements. However, significant laser power instability has been observed, and it is important to note that as a result, temperature profiles measured under nominally identical experimental conditions will not necessarily be the same. To allow the comparison of such temperature profiles, the use of a beam splitter to allow the heating of the test sample and the simultaneous characterisation of the laser beam is recommended.

It is also important to note that all temperature profiles calculated in the course of this study have been found to emanate from small regions where the surface damage is most severe. Thus it would appear that the shape of the larger heat affected zone is not an important factor as far as temperature measurement is concerned. However, the heat affected zone acts as a useful guide to the validity of data collected by the spectrograph and CCD. For example, a non-circular heat affected zone may indicate the presence of non-homogenous heat flow, and the size of the heat affected zone will help to show whether or not heat travelling through the material has encountered the edge of the test sample.

Surface damage has been shown, by the simulation of hot spots formed at the base of laser drilled holes, to introduce an uncertainty to the calculated temperature of approximately 20K for every 100μm of material that is removed from the surface during laser heating. Lower laser powers combined with longer CCD exposures may be used to reduce surface damage, but long CCD exposures have also been shown to compromise the validity of calculated temperatures. In order to balance these conflicting demands, the level of acceptable error introduced to calculated temperature profiles must be chosen. The hole depth corresponding to this error must be calculated, and an investigation made into the laser powers and corresponding sample exposures which will produce holes of this depth. Note: separate calculations will be required for each material examined, in the course of the present study, no successful experimental measurements of hole depth have been made. However, calculations of the depth of focus of the Nd:YAG laser at the test sample position, combined with theoretical estimates of the maximum hole depth incurred, indicate that however extreme the surface damage caused, the test sample surface remains within the depth of focus of the laser.

Calculated temperature profiles may also be corrupted by the flow of molten material, and by local impurities contained within non-homogenous materials, such as steels. Surface contamination of the sample, and the formation of an oxide upon heating, may also invalidate collected data.

An evaluation of the data analysis programs, written by Ladds (1994), formed part of the work described within this thesis. The effects of system parameters set by the operator, and of measurements made for calibration purposes, on the resultant calculated temperature were investigated. The cut-off value for the spectral correction coefficients was found to be crucial in determining consistent temperature distributions, and was strongly dependent on the CCD exposure used to collect the spectral sensitivity information from which the coefficients were found. The sensitivity of the wavelength calibration to its input data was studied. Wien temperature fitting was found to be affected very little by the wavelength calibration procedure, but the Planck technique was discovered to be highly susceptible to an inaccurate wavelength reference. However, due to problems encountered with the operation of the external shutter, temperatures within the ideal range of the Planck fitting method were not measured, and therefore it is impossible to quantify reliably the uncertainty introduced by this procedure.

Although the two methods of temperature fitting investigated each have an inherently more accurate temperature range, the agreement between them was found to be better than anticipated. It was concluded that there is no absolute rule governing which should be used for the determination of a particular range of temperatures, and that it would be provident to use both methods in all cases to allow a comparison of temperatures calculated by different techniques. Further refinement of the Planck fitting routine to prevent the occasional calculation of obviously erroneous temperatures is recommended.

To develop an understanding of the interaction of a laser beam with different test materials, the coupling between a calculated temperature profile, and the laser heated site from which it was generated, was determined. Grain boundaries were found to cause a distortion of the heat affected zone and melt puddle, and it was concluded that test samples cut from single crystals should be used wherever possible. It is proposed that the use of single crystals would also allow the application of the experimental system to the determination of thermodynamic properties along specific crystal axes.

An investigation has been made of the experimental implications of laser target surfaces prepared by different techniques. Highly reflective surfaces have been found to reflect infra-red light back into the cavity of the Nd:YAG laser, thus causing a further instability in laser output power. The addition of a one-way infra-red filter to the optical system between the dichroic mirror and laser cavity would stop such reflections.

Heat affected zones, which have been distorted by scratches and pitting introduced during the lapping process, have been observed. Thus, the use of polished samples is preferential, although for some materials such a surface prevents adequate absorption of laser radiation. If greyed samples are used, a microscopic evaluation of the surface, to identify whether or not disruption of the heating site has occurred, is required.

The absorptivity of metals may be improved by allowing an oxide layer to form on the surface before heating. However, for such a process to be beneficial, the oxide layer must be thin and uniform. Unless the formation of the oxide layer can be controlled, it is preferable to inhibit oxide formation completely.

An investigation into the suitability of different test materials to a study using the described experimental system has been made, and several conclusions drawn. Firstly, metallic samples have been shown to produce very narrow temperature profiles emanating from molten regions on the test surface. It is proposed that such materials would produce broader temperature distributions if the laser heating spot incident on their surface was made larger, although suggested methods for achieving this have been shown to have wider experimental implications. Also, it has been concluded that in most cases such improvements would have little beneficial effect on the temperature profiles produced. Some metals, in requiring a very high laser power combined with a very long CCD exposure to generate a measurable hot spot, have been shown to be completely unsuitable for a study by this technique. However, others have given more promising results, and in those cases further work incorporating suggested improvements to the experimental system would be useful. Molybdenum and iron are typical of metals belonging to these respective classes.

In general, the reliability of the system for measuring temperature distributions created on metals has been shown to depend upon their reflectivity and thermal diffusivity. Although all metals tend to be good thermal conductors and highly reflective, molybdenum, in being a better thermal conductor than iron, is less well suited to a study by this apparatus.

Much broader temperature profiles have been measured from ceramic test samples than from metals, due to their low reflectivities, and low thermal conductivities. In being affective absorbers of laser radiation, ceramics have allowed the use of a highly polished test surface and the operation of the laser at its optimum output power, although care must be taken to ensure that the melting temperature of the material is high enough to prevent serious surface damage. Also, the low thermal diffusivities demonstrated by these materials ensure that the passage of heat through the test sample is slow enough to allow the measurement of broad temperature profiles and the evolution of temperature profile with time. The ceramics studied have been shown to require much longer delays between successive laser heatings than metals, and it is recommended that further experimental studies of high emissivity materials incorporate an accelerated cooling system. The use of a thermocouple to measure the back face temperature of the test sample during cooling is suggested as a method for allowing the waiting time between consecutive laser heatings to be minimised.

To quantify the effects of ambient temperature and humidity on the performance of the experimental system, several investigations were made. Firstly, laser stability under relatively warm and relatively cool ambient temperatures was measured; no differences were observed. The experimental consequences of high ambient humidity have been studied. It is concluded that although arrangements have been made within the data analysis programs to correct for contamination of the detector face by water droplets and ice crystals, it is preferable to inhibit their formation and thus avoid the need for any numerical compensation. In practice this has been achieved by allowing the passage of dry nitrogen around the CCD casing for much longer than in previous studies.

The final experimental objective was to obtain data which was suitable for the calculation of thermal conductivity and thermal diffusivity by methods described by

Tytler (1995). Although temperature profiles of the expected form have been measured, the validity of such data remains in question until surface damage can be accurately quantified. Also, because of the narrow temperature profiles produced, some test materials have been shown to be inherently inapplicable for use within the experimental system.

Within the limits of experimental uncertainties described, data suitable for the determination of thermal diffusivity has been measured from a uranium dioxide sample. However, the existing experimental system is unsuitable for the measurement of such data from higher thermal diffusivity materials. Before such a study is undertaken, improvements to the external laser shutter should be made, and the delay imposed by the OMA2000 software quantified.

The work described within this thesis has highlighted several restrictions which apply to the analyses described by Tytler (1995). For example, a theoretical calculation of heat diffusion through different materials has implied that boundary conditions must be applied to any calculation of thermal conductivity. Also, the size of the beam waist has been shown to be strongly related to laser power; the calculated relationship should be included when measured temperature profiles are used for the determination of thermodynamic properties.

In conclusion, the experimental system described has been shown to be appropriate for the measurement of laser induced temperature distributions in low reflectivity, low thermal conductivity, relatively high melting point ceramics such as uranium dioxide. However, several experimental limitations have been observed, and an indication of the corresponding uncertainties introduced to measured temperatures has been made. Restrictions involved in applying this temperature measurement technique to use within a diamond anvil cell have been highlighted; it is recommended that any future work involving the experimental system described is first concerned with improving the repeatability and validity of measured data by the methods outlined, before the application of the system to measurements at elevated pressures.

APPENDIX A

A. PROGRAMMABLE TIME DELAY UNIT

To allow a pre-determined delay between the commencement of laser heating and data acquisition, a programmable time delay unit was built. A schematic diagram of this unit was given in figure 3.9 on page 70; a full circuit digram is given in figure A.1. The logic circuit connecting the unit to the OMA system is shown in figure A.2, and the corresponding timing diagram in figure A.3.

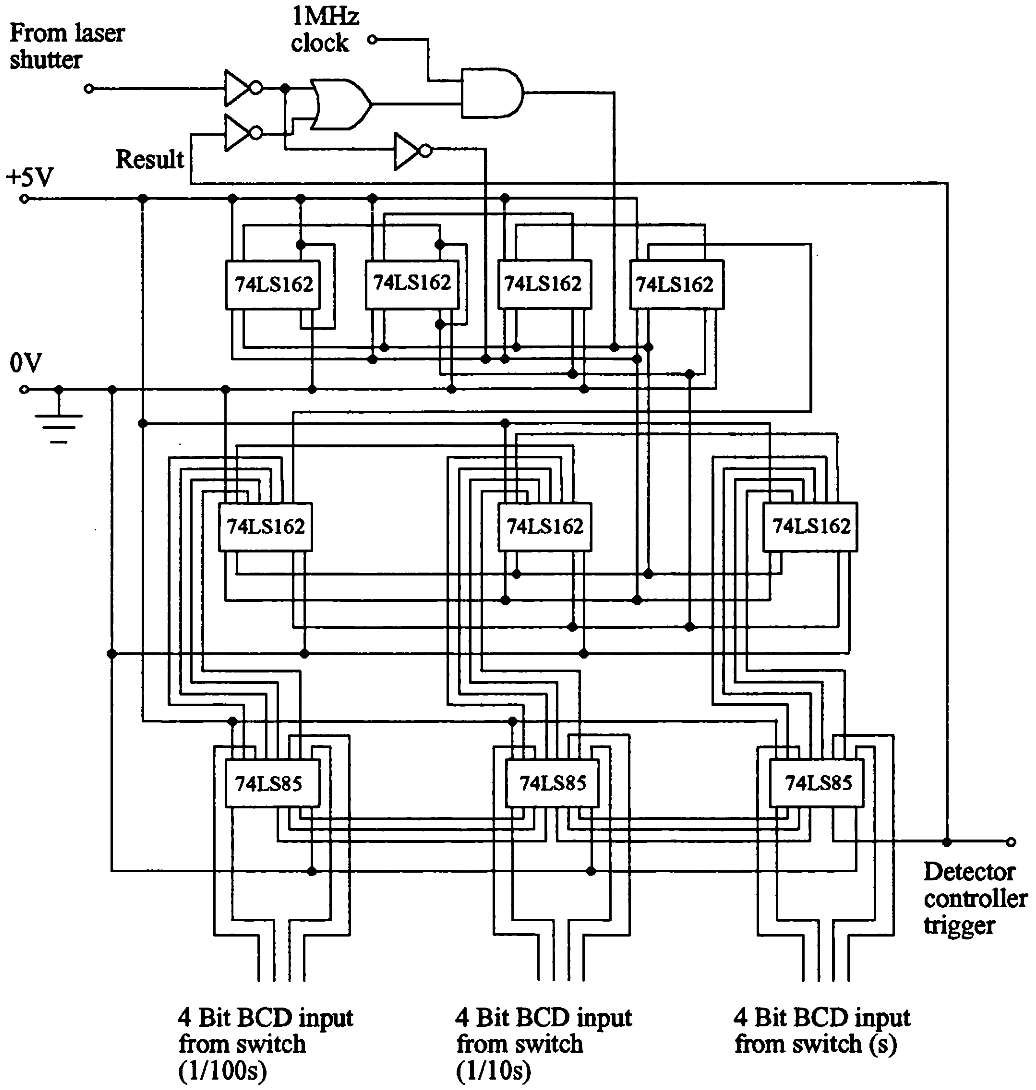

Figure A.1. Circuit diagram for the programmable time delay unit.

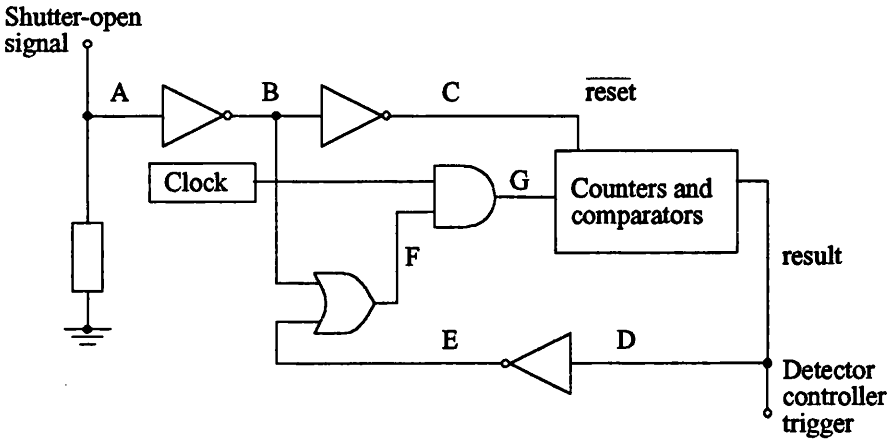

Figure A.2. Logic circuit connecting the time delay unit to the OMA system.

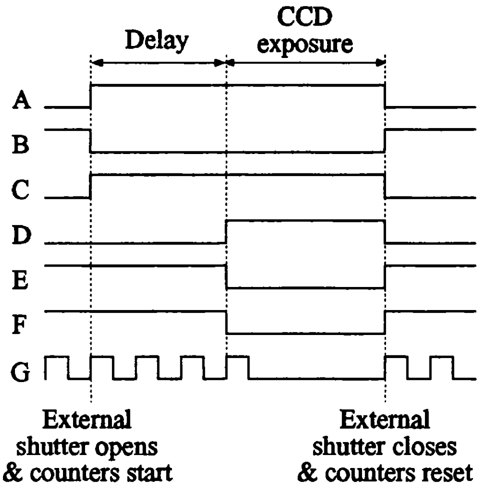

Figure A.3. Timing diagram for the circuit shown in figure A.2.

APPENDIX B

B. THE UTAH RASTER TOOLKIT

The Utah Raster Toolkit (URT) is a set of computer programs based around the Run Length Encoded (RLE) graphic format. Its primary use here is in the inspection of raw, unprocessed data recorded by the CCD, to determine whether or not data corruption has occured during acquisition. An RLE image of a typical raw data set is shown in figure B.1, and an expanded section of this image in figure B.2. Note that the horizontal axis represents wavelength, and the vertical scale the spatial position across the hot spot.

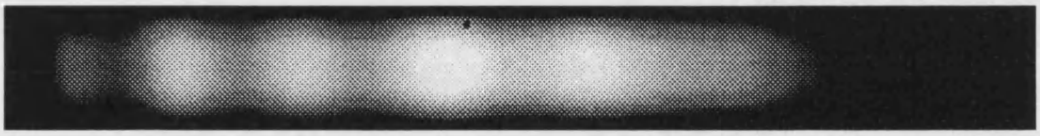

Figure B.1. RLE image of a typical raw data set.

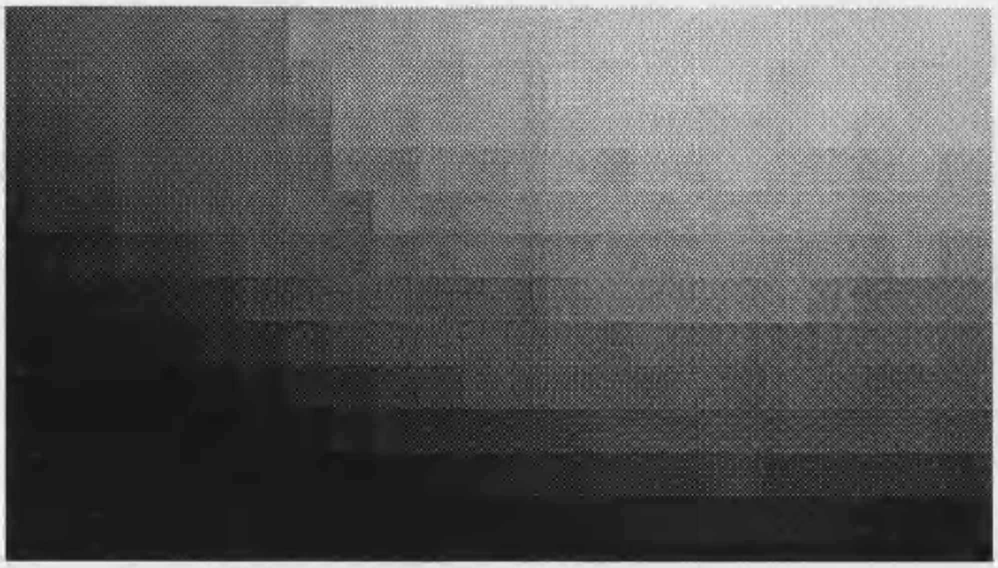

Figure B.2. Expanded section of the RLE image given in figure B.1, showing individual CCD pixels.

A comprehensive description of the implementation of the URT programs has been made by Ladds (1994).

APPENDIX C

C. X-RAY DIFFRACTOMETRY DATA

To determine the chemical composition of the test materials used, shallow angle X-ray powder diffractometry experiments were performed. The analysis was performed using a Philips diffractometer with automatic powder diffraction software (PC-APD) which is able to match the peaks in the measured reflection spectra to the lines recorded in the appropriate Powder Diffraction File published by the International Centre for Diffraction Data (ICDD-PDF). The incident X-ray radiation used was dichromatic, consisting of the copper $K_{\alpha 1}$ (1.54060Å) and $K_{\alpha 2}$ (1.54439Å) lines in the intensity ratio 2:1. As a consequence, each of the measured reflection peaks is formed by a closely spaced doublet with a 2:1 intensity ratio. The $K_{\alpha 1}$ peak is the largest.

Reflection spectra collected from uranium dioxide, a superconductor of the Bi-Sr-Ca-Cu-O family, iron, molybdenum, zirconium, and graphite are presented in the following sections.

C.1. URANIUM DIOXIDE

To determine the purity of the uranium dioxide samples used to collect the data presented in section 7.1.6, an X-ray powder diffractometry experiment was performed. The measured spectra is presented in figure C.1, and the angular positions of the observed peaks listed in table C.1, together with predicted values for uranium dioxide (ICDD-PDF file number 41-1422).

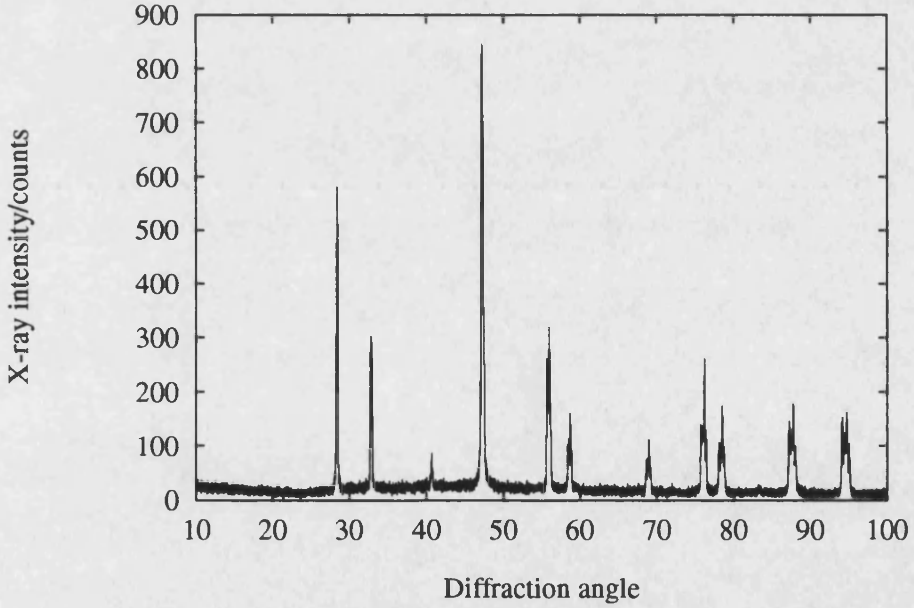

Figure C.1. Measured X-ray diffraction spectrum for polycrystalline uranium dioxide.

Measured		Predicted	
Diffraction angle (2Φ) /°	d-spacing/Å	d-spacing/Å	Plane
28.5	3.133	3.153	1 1 1
32.8	2.729	2.733	2 0 0
40.7	2.216		
47.0	1.930	1.933	2 2 0
47.3	1.922		
56.1	1.639	1.647	3 1 1
58.4	1.578	1.578	2 2 2
68.7	1.366	1.367	4 0 0
69.0	1.360		
75.8	1.255	1.254	3 3 1
78.2	1.221	1.224	4 2 0
83.3	1.159		
87.3	1.117	1.116	4 2 2
88.1	1.108		

Table C.1. Measured and predicted peak positions for an X-ray diffraction spectrum obtained from nominally pure polycrystalline uranium dioxide.

It is apparent from table C.1 that although uranium dioxide is present, there are a number of peaks which cannot been attributed to this material. Ladds (1994) described the iridium contamination of polycrystalline uranium dioxide samples supplied by AEA Technology, and so the positions of predicted peaks for iridium (ICDD-PDF file number 6-598) were identified and are presented in table C.2.

d-spacing/Å	Plane
2.217	111
1.920	200
1.358	220
1.157	311
1.108	222

Table C.2. Predicted peaks for the X-ray diffraction spectrum of iridium.

It may be observed from a comparison of the data presented in tables C.1 and C.2, that peaks predicted for iridium coincide with those measured that could not be matched to the uranium dioxide ICDD-PDF file. Therefore, it is concluded that the sample bulk was of uranium dioxide with iridium contamination present. Because the X-ray data was collected from a comparatively large region on the sample, the distribution of iridium contamination cannot be determined by this method.

C.2. Bi-Sr-Ca-Cu-O COMPOUND

To establish the stoichiometry of a sample belonging to the Bi-Sr-Ca-Cu-O superconductor family, an X-ray diffraction spectrum was collected, and is shown in figure C.2. The positions of the highest peaks were compared with powder diffraction files for a number of materials in the Bi-Sr-Ca-Cu-O group, but the best match was found to be that corresponding to $Bi_3Sr_3Ca_2Cu_4O_x$ (ICDD-PDF file number 43-298). Measured and predicted peak positions are given in table C.3.

Although the agreement between measured and predicted d-spacings presented in table C.3 is not as good for this sample as for others considered, it is concluded that the material is almost certainly of the Bi-Sr-Ca-Cu-O group, and very probably $Bi_3Sr_3Ca_2Cu_4O_x$.

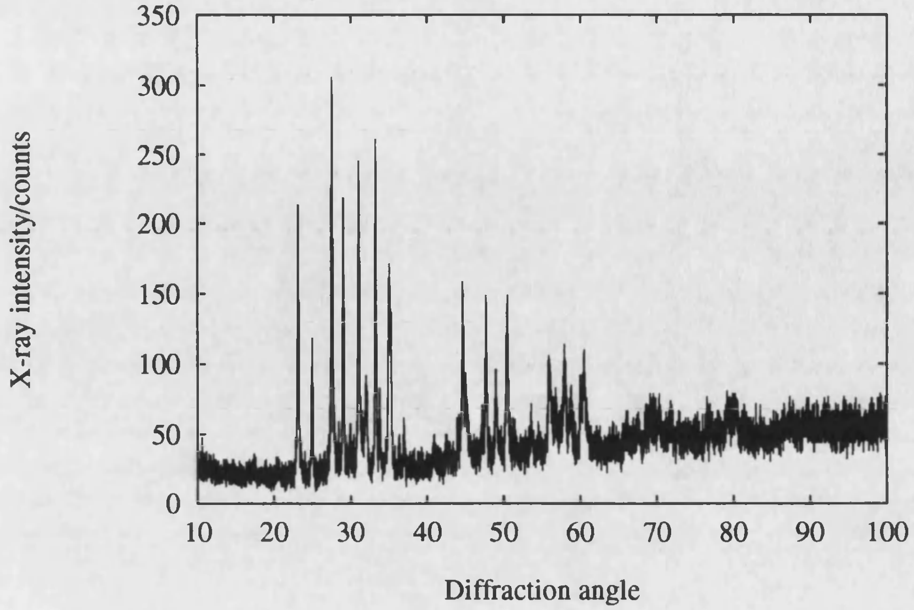

Figure C.2. Measured X-ray diffraction spectrum for a Bi-Sr-Ca-Cu-O sample.

Measured		Predicted	
Diffraction angle (2Φ) /°	d-spacing/Å	d-spacing/Å	Plane
23.17	3.837	3.84	0 0 8
24.97	3.564	3.58	1 5 3
27.56	3.234	3.24	1 5 5
29.04	3.072	3.07	0 0 10
31.04	2.879	2.879	1 5 7
33.26	2.692	2.698	2 0 0, 0 10 0
33.73	2.561	2.559	0 0 12
35.29	2.542	2.544	2 0 4, 0 10 4
44.62	2.029	2.028	2 0 10, 0 10 10
47.68	1.906	1.910	2 10 0
48.97	1.859	1.855	2 0 12, 0 10 12
50.47	1.807	1.806	1 5 15
55.85	1.645	1.645	3 5 5, 1 15 5
57.89	1.592	1.592	3 5 7, 1 15 7
60.59	1.527	1.528	3 5 9, 1 15 9

Table C.3. Measured and predicted peak positions for an X-ray diffraction spectrum obtained from the Bi-Sr-Ca-Cu-O sample.

C.3. IRON

The composition of a test sample believed to be iron was investigated by X-ray diffractometry. The measured spectrum is shown in figure C.3 and the measured peak positions tabulated in table C.4. The predicted positions of spectral peaks (ICDD-PDF file number 6-696) are also given in table C.4.

The data presented in table C.4 indicates that the test sample was iron, as suspected. However, a microscopic examination of the surface following an acid etch, see section 7.3.2, identified the presence of pearlite grains, implying the material was in fact a mild steel.

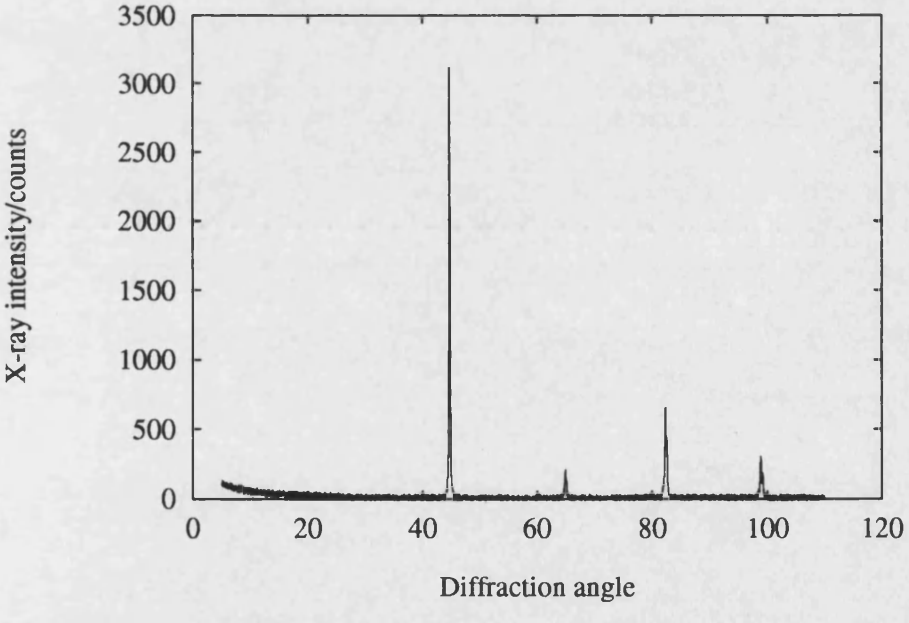

Figure C.3. Measured X-ray diffraction spectrum for a nominally iron sample.

Measured		Predicted	
Diffraction angle (2Φ) /°	d-spacing/Å	d-spacing/Å	Plane
44.7	2.027	2.027	1 1 0
65.0	1.434	1.433	2 0 0
82.3	1.170	1.170	2 1 1
98.9	1.014	1.013	2 2 0

Table C.4. Measured and predicted peak positions for an X-ray diffraction spectrum obtained from iron.

C.4. MOLYBDENUM

The identity of a nominally molybdenum sample was determined by an X-ray diffraction study. The measured spectrum is shown in figure C.4 and the measured and predicted peak positions (ICDD-PDF file number 42-1120) given in table C.5. The Miller indices of the crystal plane from which each line was generated are also given.

The excellent agreement between the measured and predicted peak positions shown in table C.5 indicate that the material was molybdenum, as expected.

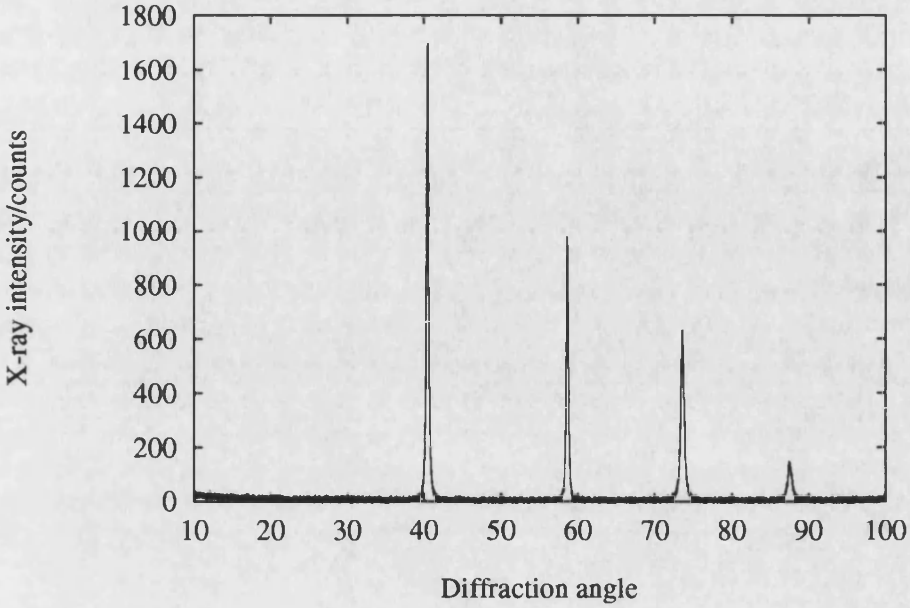

Figure C.4. Measured X-ray diffraction spectrum for molybdenum

Measured		Predicted	
Diffraction angle (2Φ) /°	d-spacing/Å	d-spacing/Å	Plane
40.5	2.227	2.225	1 1 0
58.6	1.575	1.574	2 0 0
73.6	1.286	1.285	2 1 1
87.4	1.115	1.113	2 2 0

Table C.5. Measured and predicted peak positions for an X-ray diffraction spectrum obtained from molybdenum

C.5. ZIRCONIUM

In order to confirm the identity of a zirconium sample, its X-ray diffraction spectrum was measured and is shown in figure C.5. Table C.6 lists the measured and predicted peak positions (ICDD-PDF 5-665), and the corresponding Miller indices.

In general, the measured and predicted data sets agree well. Although the measured peaks at diffraction angles of 68.69° and 69.52° were not very good matches to the corresponding predicted values, those at other angles were much better, and it was concluded that the material was zirconium as expected.

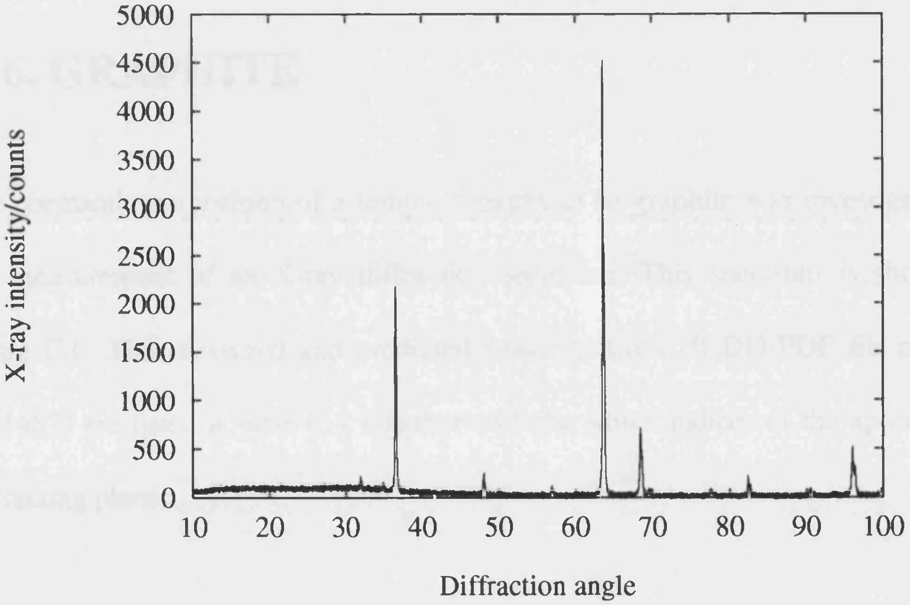

Figure C.5. Measured X-ray diffraction spectrum for zirconium.

Measured		Predicted	
Diffraction angle (2Φ) /°	d-spacing/Å	d-spacing/Å	Plane
31.99	2.796	2.798	1 0 0
34.88	2.570	2.573	0 0 2
36.53	2.458	2.459	1 0 1
48.04	1.893	1.894	1 0 2
56.91	1.617	1.616	1 1 0
63.54	1.463	1.463	1 0 3
66.76	1.400	1.399	2 0 0
68.47	1.370	1.368	1 1 2
68.69	1.365	1.350	2 0 1
69.52	1.351	1.287	0 0 4
77.53	1.230	1.230	2 0 2
82.43	1.169	1.169	1 0 4
90.45	1.085	1.084	2 0 3
93.41	1.058	1.059	2 1 0
96.02	1.036	1.036	2 1 1

Table C.6. Measured and predicted peak positions for an X-ray diffraction spectrum obtained from zirconium

C.6. GRAPHITE

The chemical composition of a sample thought to be graphite was investigated by the measurement of an X-ray diffraction spectrum. This spectrum is shown in figure C.6. The measured and predicted peak positions (ICDD-PDF file number 41-1487) are listed in table C.7 together with the Miller indices of the appropriate diffracting planes.

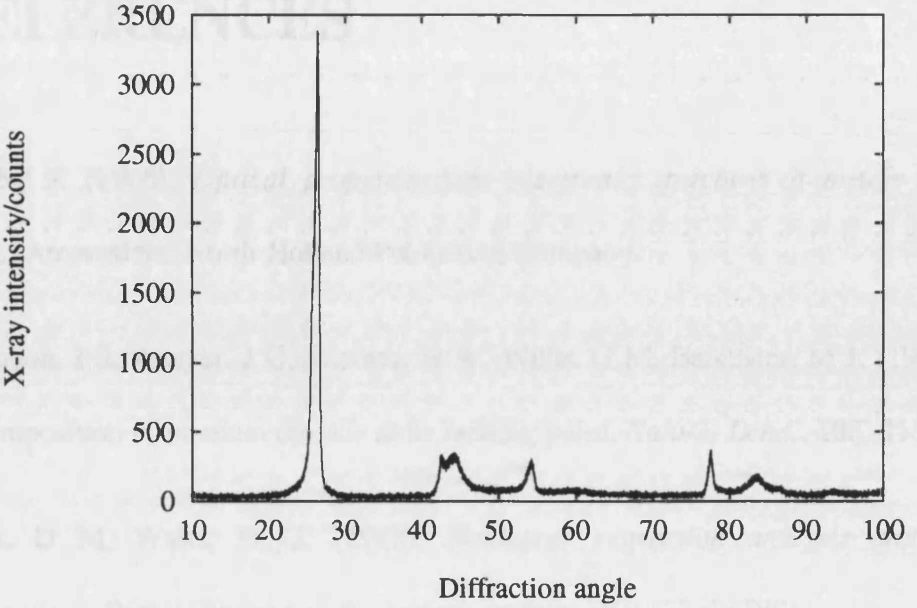

Figure C.6. Measured X-ray diffraction spectrum for graphite.

Measured		Predicted	
Diffraction angle (2Φ) /°	d-spacing/Å	d-spacing/Å	Plane
26.24	3.394	3.380	0 0 2
42.46	2.128	2.139	1 0 0
44.51	2.034	2.039	1 0 1
54.37	1.686	1.681	0 0 4
59.70	1.548	1.548	1 0 3
77.53	1.230	1.234	1 1 0
83.43	1.158	1.160	1 1 2
86.46	1.125	1.121	0 0 6
94.06	1.053	1.057	2 0 1

Table C.7. Measured and predicted peaks for an X-ray diffraction spectrum obtained from graphite.

The good agreement between the measured and predicted d-spacings presented in table C.7, indicates that the test sample was graphite, as anticipated.

REFERENCES

Abelès, F. (1966). *Optical properties and electronic structure of metals and alloys*. Amsterdam: North-Holland Publishing Company.

Anderson, J S, Sawyer, J O, Worner, H W, Willis, G M, Bannister, M J. (1960). Decomposition of uranium dioxide at its melting point. *Nature, Lond.*, **185**, 915.

Bates, D M, Watts, D G. (1988). *Nonlinear regression analysis and its applications*. Probability and mathematical statistics. New York: Wiley.

Benedict, R P. (1984). *Fundamentals of temperature, pressure, and flow measurements. 3rd ed.* New York: John Wiley & Sons.

Berman, R. (1976). *Thermal conduction in solids*. Oxford: Clarendon Press.

Boyd, R W. (1983). *Radiometry and the detection of optical radiation.* New York: John Wiley and Sons.

Browning, E. (1961). *The toxicity of industrial metals.* New York: John Wiley and Sons.

Charschan, S S, Draper, C W, Palmquist, J M, Tice, E S, Webb, R, Zaleckas, V J. (1978). *Guide for material processing by lasers*. Baltimore: The Paul M Harrod Company.

Chatfield, C. (1984). *The analysis of time series - an introduction.* London: Chapman and Hall

Coxon, W F. (1960). *Temperature measurement and control.* London: Heywood and Company Ltd.

Dawson, J K, Sowden, R G. (1963). *Chemical aspects of nuclear reactors.* London: Butterworths.

Deans, S R. (1983). *The Radon transform and some of its applications.* New York: John Wiley and Sons.

Ehlert, T C. (1958). *The melting point and spectral emissivity of* UO_2. MS Thesis, University of Winconsin.

Ford, W F. (1967). *The effect of heat on ceramics.* London: Maclaren & Sons.

Fowles, G R. (1975). *Introduction to modern optics.* New York: Dover Publications Inc.

Gentry, P J. (1981). A survey of the published data concerning the hemispherical emmisivity of uranium dioxide. Technical Report ND-R-687(W), United Kingdom Atomic Energy Authority, Windscale Nuclear Power Development Laboratories. Northern Division Report.

Gill, P, Murray, W, Wright, M H. (1981). *Practical optimisation.* London: Academic Press.

Ginsberg, D M. (1992). *Physical properties of high temperature superconductors III.* New Jersey: World Scientific.

Goodfellow. (1994). Goodfellow Cambridge Limited Catalogue.

Grant, G A. (1977). *General physics and heat.* London: Edward Arnold.

Gronvold, F. (1955). High temperature X-ray study of uranium oxides in the UO_2–U_3O_8 region. *J. Inorg. & Nuclear Chem.*, **1**, 357.

Hartley, H O. (1961). The modified Gauss-Newton method for fitting of non-linear regression functions by least squares. *Technometrics*, **3**, 269–280.

Hayes, W. ed. (1974). *Crystals with the fluorite structure.* Oxford: Clarendon Press.

Hecht, E. (1987). *Optics.* Reading , Massachusetts: Addison-Wesley Publishing Company.

Heeb, B, Gauckler, L J, Heinrich, H, Kostorz, G. (1993). Microstructure and properties of melt-processed Bi-2212 ($Bi_2Sr_2CaCu_2O_x$). *Journal of Electronic Materials*, **22.**

Heinz, D L and Jeanloz, R. (1987). Temperature measurements in the laser heated diamond anvil cell. *High Pressure Research in Mineral Physics*, 113-127.

Herzfield, C M. ed. (1962). *Temperature - its measurement and control in science and industry, volume 3.* New York: Reinhold Publishing Corporation.

Hooker, C N, Ubbelohde, A R, Young, D A. (1963). *Proc. Roy. Soc. A*, **276**, 83.

Hutchings, M T. (1987). High-temperature studies of UO_2 and ThO_2 using neutron scattering techniques. *J. Chem. Soc., Faraday Trans.* 2, **83**, 1083–1103.

Kaye, G W C, Laby, T H. (1986). *Tables of physical and chemical constants and some mathematical functions, 15th edition.* London: Longman.

Kelly, P J, Brooks, M S S. (1987). Electronic structure and ground state properties of the actinide oxides. *J. Chem. Soc., Faraday Trans. 2*, **83**, 1189–1203.

Klein, C A, Holland, M G. (1964). *Phys. Rev.*, **136**, A575.

Komatsu, T, Imai, K, Sato, R, Matusita, K, Yamashita, T. (1988). Preparation of high T_c superconducting Bi-Ca-Sr-Cu-O ceramics by the melt quenching method. *Japanese Journal of Applied Physics*, **27**, L533-L535.

Ladds, D A. (1991). *The construction and use of a laser heated diamond cell.* Bath: University of Bath.

Ladds, D A. (1994). *Remote measurement of surface temperature distributions in laser heated samples. PhD thesis.* Bath: University of Bath.

Lambertson, W A, Mueller, M H. (1953). Uranium oxide phase equilibrium system, UO_2– MgO. *J. Amer. Chem. Soc.*, **36**, 332.

Levi, L. (1980). *Applied Optics - A guide to optical system design, volume 2*. New York: John Wiley and Sons.

Loeb, A L. (1954). Thermal conductivity: VIII. A theory of thermal conductivity of porous materials. *J. Amer. Ceramic. Soc.*, **37**, 96.

MacEwen, J R. (1961). *Grain growth in sintered uranium dioxide*. Atomic Energy of Canada Ltd. Report, CRFD-999.

Maeda, H, Tanaka, Y, Fukutomi, M, Asano, T. (1988). *Jpn. J. Appl. Phys*. **27**, L209.

Michel, C, Hervieu, M, Borel, M M, Grandin, A, Deslandes, F, Provost, J, Raveau, B. (1987). *Z Phys*, B **68**, 421.

Morrell, R. (1985). *Handbook of properties of technical and engineering ceramics. Part 1: An introduction for the engineer and designer*. London: Her Majesty's Stationery Office.

Motorola Semiconductors. (1986). *Fast and LS TTL data*. Genève, Switzerland.

NPL certificate of calibration. (1986). Ref 127460/OP3. Teddington: National Physical Laboratory.

National Semiconductor Corporation. (1987). *LS/S/TTL logic databook*. California.

Newport Catalogue. (1990). *Optical tutorial, section N*.

Nutting, J, Baker, R G. (1965). *The microstruture of metals*. Bungay, Suffolk: The Chaucer Press Ltd.

O'Shea, D C. (1985). *Elements of modern optical design*. New York: John Wiley and Sons.

Palik, E D. (1985). *Handbook of optical constants of solids*. Orlando: Academic Press Inc..

Parrott, J E, Stuckes, A D. (1975). *Thermal conductivity of solids*. London: Pion Limited.

Pedrotti, F L, Pedrotti, L S. (1987). *Introduction to optics*. New Jersey: Prentice-Hall International Publications.

Photon, Inc. (1991). *Instruction manual for BeamScan model 2180 optical profiler*. Santa Clara: Photon Inc.

Quantronix (1984). *Series 100 lasers - technical manual*. New York

Quantronix (1990). *Model 366 laser stabiliser*. New York

RS Data Library. (1990). *Data sheet 10192*.

Rand, M H, Ackermann, R J, Gronvold, F, Pattoret. (1978). *Rev. Int. Hautes Temp. Refract.*, **15**, 355–365.

Rao, C N R, Nagarajan, R, Vijayaraghavan, R. (1993). Synthesis of cuprate superconductors. *Supercond. Sci. Technol.*, **6**, 1-22.

Reynolds, W N. (1968). *Physical properties of graphite.* Amsterdam: Elsvier Publishing Co Ltd.

Rollason, E C. (1961). *Metallurgy for engineers.* London: Edward Arnold (Publishers) Ltd.

Ross, A M. (1960). The dependence of the thermal conductivity of uranium dioxide on density, microstructure, stoichiometry and thermal neutron irradiation. Atomic energy of Canada Ltd. Report, CRFD-817.

Rothwell, E. (1961). High temperature substoichiometry in uranium dioxide. UKAEA Report AERE-R 3897.

Slack, G A. (1972). *Proc. int. conf. on phonon scattering in solids,* p 24. Service de Documentation du CEN Saclay.

Swanson *et al.* (1953). National Bureau Stanadards (US), **539**, 3.

TC Ltd. (1995). *Thermocouple and Resistance Thermometry Data Book.*

Taylor, R. (1966). *Phil. Mag.*, **13**, 121.

Tennent, R M. (1988). *Science data book.* London: Oliver and Boyd.

Tottle, C R. (1984). *An encyclopaedia of metallurgy and materials.* Plymouth:Macdonald and Evans Ltd.

Tytler, D G F. (1995). *Determination of the thermal properties of materials utilising remote sensing techniques. PhD thesis.* Bath: University of Bath.

Voort, V. (1984). *Metallography: principles and practice.* New York: McGraw-Hill Book Company.

Weast, R P, ed.. (1976). *Handbook of chemistry and physics. Ready reference book of chemical and physical data, 57th edition.* Cleveland, Ohio: CRC Press Inc.

Wilkinson, W D. (1962). *Uranium metallurgy. Vol 2: Uranium corrosion and alloys.* New York: Interscience Publishers.

Wisnyi, L G, Pijanowski, S. (1956). *The melting point of* UO_2. USAEC Report, KAPL-1658.

Wyatt, O H, Dew-Hughes, D. (1974). *Metals, ceramics and polymers.* London: Cambridge University Press.

Yemel'Yanov, V S, Yevstyukhin, A I. (1969). *Metallurgy of nuclear fuel. Properties and principles of the technology of uranium, thorium, and plutonium.* Oxford: Pergamon Press.